

Surface-Based Tools for Characterizing the Human Brain Cortical Morphology

by

Alberto Fernández Pena

A dissertation submitted in partial fulfillment of the
requirements for the degree of Doctor of Philosophy in

Biomedical Science and Technology

Universidad Carlos III de Madrid

Advisors:

Dr. Susanna Carmona Cañabate

Dr. Manuel Desco Menéndez

Tutor:

Dr. Manuel Desco

January 2023

This thesis is distributed under license “Creative Commons **Attribution - Non Commercial - Non Derivatives**”.



A mi hija.

AGRADECIMIENTOS

Quien me conoce sabe que entre mis virtudes no está precisamente la expresividad, así que podéis figuraros el esfuerzo que me supone escribir estas líneas. Tengo mucha gente a la que agradecer su apoyo y su ayuda durante los años de esta tesis, pero espero que sepáis perdonar que en este caso me centre en mi familia, la sanguínea y la que me ha adoptado en estos años.

Recuerdo perfectamente esa primera entrevista para entrar a trabajar al laboratorio. Ahí estaban Yasser, Susana y David contándome qué era la Plataforma de Neuroimagen en la que entraría a trabajar. A ellos tres les debo muchísimo tanto a nivel personal como laboral. A Yasser, que me ha llevado por toda Cuba haciéndome sentir como si fuera de su familia, que durante todos estos años me ha enseñado y ayudado tanto cuando hubiera sido muy sencillo desentenderse. Sin él, sus ideas y sus miles de líneas de scripts de MATLAB este trabajo no existiría, o sería una cosa muy diferente. A Susana, que se ha convertido, además de en jefa, en una fantástica amiga, siempre dispuesta a ayudar. Una persona capaz de destacar en la ciencia, en la pintura, en el deporte, probablemente la DaVinci de nuestra era. Y a David, una de las mejores personas que he conocido. Él fue quien me introdujo en la neuroimagen y gracias a él aprendí todo lo que sé de cloud.

Todo este viaje no habría sido lo mismo sin mis compañeras y compañeros. Desde la primera semana, Luis me hizo sentir como en casa. Con él he compartido aficiones, horas de charla, recetas de cocina. Si he aprendido algo de estadística en todos estos años ha sido gracias a él. Tampoco habría sido posible este trabajo sin Dani. Es el héroe de las películas que se tira encima de la granada para salvar a todo el mundo. Te está ayudando antes de que te dé tiempo a pedirselo, puede apartar todo lo que esté haciendo para explicarte lo que sea y seguramente esté en el top 20 de personas más inteligentes del planeta. Javi es otro ser humano excepcional, siempre armado con el peor chiste que te puedas imaginar, siempre dispuesto a hacer de enlace entre la parte más biológica del trabajo y la parte más “ingenieril”. Magda y María, que además de buenos ratos, siempre traen comida valenciana o murciana para que probemos. También he de agradecer a Joost sus revisiones de manuscritos, sus ideas para los métodos y las charlas de fútbol. Por último, a Manolo por darme la oportunidad de trabajar en este laboratorio.

Ya terminando, quiero agradecer a mis padres haberme apoyado durante toda mi carrera y haber confiado en mí incluso cuando yo no lo hacía tanto. Gracias a vosotros todo esto ha sido más fácil. Finalmente, a María, que me ha ayudado, cuidado y aguantado, especialmente estas últimas semanas. La mejor compañera posible para este viaje que empezamos pronto.

Gracias a todos vosotros, y a tantos otros que no estáis nombrados, pero que habéis sido importantes en mi vida estos últimos años.

PUBLISHED AND SUBMITTED CONTENT

Journal Articles:

- A. Fernández-Pena, D. Martín de Blas, F. J. Navas-Sánchez, L. Marcos-Vidal, P. M. Gordaliza, J. Santonja, J. Janssen, S. Carmona, M. Desco, and Y. Alemán-Gómez, “ABLE: Automated Brain Lines Extraction Based on Laplacian Surface Collapse,” *Neuroinformatics*, Aug. 2022. doi: [10.1007/s12021-022-09601-7](https://doi.org/10.1007/s12021-022-09601-7). [Online]. Available: <https://link.springer.com/10.1007/s12021-022-09601-7>.

Author Contributions: Fernández-Pena was responsible for the conception and implementation of the algorithm, performing the statistical analysis, creating the figures, and writing the manuscript. Alemán-Gómez and Martín de Blas supervised the conception and implementation of the algorithm. All authors were involved in writing and reviewing the paper.

This article is wholly included in this dissertation as Chapter 3.

The material from this source included in this thesis is not singled out with typographic means and references.

- A. Fernández-Pena, F. J. Navas-Sánchez, D. Martín de Blas, L. Marcos-Vidal, P. M. Gordaliza, I. Martínez-Tejada, J. Janssen, S. Carmona, M. Desco, and Y. Alemán-Gómez, “Estimation of Vertex-wise Sulcal Width Maps on Cortical Surfaces,” *bioRxiv*, Nov. 2022. doi: [10.1101/2022.11.09.515775](https://doi.org/10.1101/2022.11.09.515775). [Online]. Available: <https://www.biorxiv.org/content/10.1101/2022.11.09.515775v1>. Submitted for publication to NeuroImage.

Author Contributions: Fernández-Pena was responsible for the conception and implementation of the algorithm, performing the statistical analysis, creating the figures, and writing the manuscript. Navas-Sánchez was responsible for additional statistical analysis. Alemán-Gómez and Martín de Blas supervised the conception and implementation of the algorithm. All authors were involved in writing and reviewing the paper.

This article is wholly included in this dissertation as Chapter 4.

The material from this source included in this thesis is not singled out with typographic means and references.

Posters:

- A. Fernández-Pena, D. Martín de Blas, J. Santonja, L. Marcos-Vidal, I. Martínez-Tejada, M. Martínez-García, L. Carretero-Gómez, M. Paternina, J. Janssen, F. J.

Navas-Sánchez, S. Carmona, M. Desco, Y. Alemán-Gómez. “Automated Sulcal Line Extraction based on Laplacian Skeletonization,” presented at the 25th Org. of the Hum. Brain Mapp. (OHBM), Rome, Jun. 2019.

Author Contributions: Fernández-Pena was responsible for the conception and implementation of the algorithm, performing the statistical analysis, creating the figures, and writing the manuscript. Alemán-Gómez supervised the conception and implementation of the algorithm. All authors were involved in writing and reviewing the poster.

OTHER RESEARCH MERITS

Journal Articles:

- J. Janssen, C. Alloza, C. Díaz-Caneja, J. Santonja, L. Pina-Camacho, P. Gordaliza, A. Fernández-Pena, N. Lois, E. Buimer, N. van Haren, W. Cahn, E. Vieta, J. Castro-Fornieles, M. Bernardo, C. Arango, R. Kahn, H. Hulshoff Pol, and H. Schnack, “Longitudinal Allometry of Sulcal Morphology in Health and Schizophrenia,” *Journal of Neuroscience*, vol. 42, no. 18, 2022. doi: [10.1523/JNEUROSCI.0606-21.2022](https://doi.org/10.1523/JNEUROSCI.0606-21.2022)
- F. Navas-Sánchez, D. Martín De Blas, A. Fernández-Pena, Y. Alemán-Gómez, A. Lage-Castellanos, L. Marcos-Vidal, J. Guzmán-De-Villoria, I. Catalina, L. Lillo, J. Muñoz-Blanco, A. Ugalde, B. Quintáns, M.-J. Sobrido, S. Carmona, F. Grandas, and M. Desco, “Corticospinal tract and motor cortex degeneration in pure hereditary spastic paraparesis type 4 (SPG4),” *Amyotrophic Lateral Sclerosis and Frontotemporal Degeneration*, vol. 23, no. 1-2, 2022. doi: [10.1080/21678421.2021.1962353](https://doi.org/10.1080/21678421.2021.1962353)
- F. Navas-Sánchez, L. Marcos-Vidal, D. Martín de Blas, A. Fernández-Pena, Y. Alemán-Gómez, J. Guzmán-de-Villoria, J. Romero, I. Catalina, L. Lillo, J. Muñoz-Blanco, A. Ordoñez-Ugalde, B. Quintáns, M.-J. Sobrido, S. Carmona, F. Grandas, and M. Desco, “Tract-specific damage at spinal cord level in pure hereditary spastic paraplegia type 4: a diffusion tensor imaging study,” *Journal of Neurology*, vol. 269, no. 6, 2022. doi: [10.1007/s00415-021-10933-8](https://doi.org/10.1007/s00415-021-10933-8)
- M. Martínez-García, M. Paternina-Die, E. Barba-Müller, D. Martín de Blas, L. Beumala, R. Cortizo, C. Pozzobon, L. Marcos-Vidal, A. Fernández-Pena, M. Picado, E. Belmonte-Padilla, A. Massó-Rodríguez, A. Ballesteros, M. Desco, Ó. Vilarroya, E. Hoekzema, and S. Carmona, “Do pregnancy-induced brain changes reverse? The brain of a mother six years after parturition,” *Brain Sciences*, vol. 11, no. 2, 2021. doi: [10.3390/brainsci11020168](https://doi.org/10.3390/brainsci11020168)
- F. Navas-Sánchez, A. Fernández-Pena, D. Martín de Blas, Y. Alemán-Gómez, L. Marcos-Vidal, J. Guzmán-de-Villoria, P. Fernández-García, J. Romero, I. Catalina, L. Lillo, J. Muñoz-Blanco, A. Ordoñez-Ugalde, B. Quintáns, J. Pardo, M.-J. Sobrido, S. Carmona, F. Grandas, and M. Desco, “Thalamic atrophy in patients with pure hereditary spastic paraplegia type 4,” *Journal of Neurology*, vol. 268, no. 7, 2021. doi: [10.1007/s00415-020-10387-4](https://doi.org/10.1007/s00415-020-10387-4)
- C. M. Díaz-Caneja, C. Alloza, P. M. Gordaliza, A. Fernández-Pena, L. de Hoyos, J. Santonja, E. E. L. Buimer, N. E. M. van Haren, W. Cahn, C. Arango, R. S. Kahn,

H. E. Hulshoff Pol, H. G. Schnack, and J. Janssen, “Sex Differences in Lifespan Trajectories and Variability of Human Sulcal and Gyrus Morphology,” *Cerebral Cortex*, vol. 31, no. 11, pp. 5107–5120, Oct. 2021. DOI: [10.1093/cercor/bhab145](https://doi.org/10.1093/cercor/bhab145). [Online]. Available: <https://academic.oup.com/cercor/article/31/11/5107/6309923>

Conference Papers:

- D. Talia, P. Trunfio, F. Marozzo, L. Belcastro, J. Garcia-Blas, D. del Rio, P. Couvée, G. Goret, L. Vincent, A. Fernández-Pena, D. Martín de Blas, M. Nardi, T. Pizzuti, A. Spătaru, and M. Justyna, “A Novel Data-Centric Programming Model for Large-Scale Parallel Systems,” in *Lecture Notes in Computer Science (including subseries Lecture Notes in Artificial Intelligence and Lecture Notes in Bioinformatics)*, vol. 11997 LNCS, 2020, pp. 452–463. DOI: [10.1007/978-3-030-48340-1_35](https://doi.org/10.1007/978-3-030-48340-1_35). [Online]. Available: http://link.springer.com/10.1007/978-3-030-48340-1_35
- J. García Blas, J. Fernández, J. Carretero, F. Marozzo, D. Talia, D. Martín de Blas, and A. Fernández-Pena, “Convergence of HPC and Big Data in extreme-scale data analysis through the DCEx programming model,” IEEE 34th International Symposium on Computer Architecture and High Performance Computing (SBAC-PAD), Bordeaux, Nov. 2022.

Patents:

- Software registration: CIBERSAMXnat, Record No. 09-RTPI-08647.7/2020

CONTENTS

SUMMARY	1
THESIS OUTLINE	5
1. INTRODUCTION.	7
1.1. Key Concepts on Cortical Folding and Neurodevelopment	7
1.1.1. Morphogenesis and Gyrification of the Human Cortex	7
1.1.1.1. External Constraints	8
1.1.1.2. Differential Tangential Expansion.	9
1.1.1.3. Axonal Tension	10
1.1.1.4. Hybrid Models	10
1.1.2. Cortical Layers	11
1.1.3. Relationship Between Brain Gyrification and Pathologies	12
1.2. Assessing the Cortical Anatomy Using Magnetic Resonance Imaging	13
1.2.1. Working with Magnetic Resonance Images	13
1.2.1.1. Voxel-Based Approaches.	14
1.2.1.2. Surface-Based Approaches.	15
1.2.1.3. Regions of Interest	17
1.2.2. Cortical Morphometry	18
1.2.2.1. Surface Area.	18
1.2.2.2. Cortical Thickness	19
1.2.2.3. Cortical Volume.	20
1.2.2.4. Cortical Depth.	21
1.2.2.5. Gyrification Index.	23
1.2.2.6. Sulcal Width.	23
1.2.2.7. Cortical Lines Extraction.	26
2. MOTIVATION AND OBJECTIVES	31
2.1. Motivation	31
2.2. Hypothesis and Objectives	32

3. AUTOMATED BRAIN LINES EXTRACTION BASED ON LAPLACIAN SURFACE COLLAPSE	35
Abstract	35
3.1. Introduction	35
3.2. Methods	38
3.2.1. Geodesic Depth Map Estimation	38
3.2.2. Gyral Crown and Sulcal Fundi Extraction	39
3.2.2.1. Sulcal Segmentation	40
3.2.2.2. Gyral Crowns Extraction	40
3.2.2.3. Sulcal Fundi Extraction	42
3.2.3. Validation	43
3.2.3.1. Sample and MRI Acquisition	43
3.2.3.2. Evaluation Metrics	44
3.3. Results	46
3.3.1. Brain Lines: Gyral Crowns and Sulcal Fundi	46
3.3.2. Sulcal Fundi Curvature and Depth	47
3.3.3. Sulcal Fundi Longitudes	48
3.3.4. Reproducibility: Hausdorff Distances Between Test and Retest	52
3.3.5. Execution Time	55
3.4. Discussion	55
3.5. Conclusion	57
4. ESTIMATION OF VERTEX-WISE SULCAL WIDTH MAPS ON CORTICAL SURFACES	59
Abstract	59
4.1. Introduction	59
4.2. Methods	61
4.2.1. Cortical Surface Extraction and Sulcal Depth Computation	61
4.2.2. Depth-based Isolines Construction and Labeling	62
4.2.3. Sulcal Width Computation	64
4.2.4. Validation	65
4.2.4.1. Validation Using Simulated Data	65

4.2.4.2. Validation Using HCP Test-Retest Dataset	66
4.2.4.3. Application to the OASIS-3 Dataset	67
4.2.5. Statistical Analyses	68
4.2.5.1. Simulated Data	68
4.2.5.2. Test-Retest Dataset	68
4.2.6. Subcohort of OASIS-3 Dataset	68
4.3. Results	69
4.3.1. Results on the Simulated Sulcus	69
4.3.2. Results on the HCP Test-Retest Dataset	69
4.3.3. Relationship Between Vertex-wise Sulcal Width and Age	73
4.4. Discussion	74
4.4.1. Limitations	76
4.5. Conclusions.	76
5. MORPHOLOGICAL EVALUATION OF AN AGING DATASET.	79
5.1. Sample Description	79
5.2. Interaction Between Age and Cortical Thickness in Sulcal/Gyral Lines	80
5.2.1. Statistical Analysis.	81
5.2.2. Results	81
5.3. Correlation Between the Length of Sulcal/Gyral Lines and Age.	83
5.3.1. Statistical Analysis.	83
5.3.2. Results	83
5.4. Vertex-wise Correlations Between Age, Thickness, and Width	85
5.4.1. Statistical Analysis.	85
5.4.2. Results	86
5.5. Discussion	86
6. GENERAL DISCUSSION	89
6.1. Limitations	91
6.2. Future Lines	91
7. CONCLUSIONS	93
BIBLIOGRAPHY.	95

LIST OF FIGURES

1.1	Development of cortical gyrus.	8
1.2	External constraints.	9
1.3	Differential tangential expansion.	9
1.4	Axonal Tension.	10
1.5	Cortical layers organization.	12
1.6	Example of brain acquisition using structural MRI.	14
1.7	Limitations of interpretation of gray matter VBM results.	15
1.8	Example of FreeSurfer output.	16
1.9	Representation of a 3D cortical surface.	17
1.10	Different scenarios representing the limitations on the interpretation of cortical thickness.	20
1.11	Scheme of the estimation of cortical thickness and cortical volume.	21
1.12	Representation of Euclidean, geodesic, and travel depth.	22
1.13	Difference of organization between supragranular and infragranular layers in cortical regions of gyrus and sulcus.	27
3.1	Summary of the processing workflow for the brain lines extraction method.	39
3.2	Detail of the endpoint location and delineation of sulcal and gyral lines.	42
3.3	Comparison of sulcal lines extracted with different methods.	46
3.4	Close-up of the individual differences between labeling methods.	47
3.5	Plot of the differences in curvature and depth between the proposed method and the reference methods.	48
3.6	Scatter plots and regression of the longitudes obtained using the different sulcal lines extraction methods and the BrainVISA longitudes for the studied sulci.	50
3.7	Bland-Altman plots comparing the four methods (ABLE, GPDM, Mindboggle, and TRACE) against BrainVISA sulcal lengths.	50
3.8	Comparisons of logarithms of mean and maximum Hausdorff distances between ABLE and the reference methods.	53
4.1	Graphic representation of the sulcal width estimation steps.	62

4.2	Schematic view of the generation of the simulated sulcus.	66
4.3	Regression plot and Bland-Altman for comparing the simulated and estimated sulcal widths in the phantom sulcus.	69
4.4	Violin plot representing the mean sulcal width for the ten selected sulci. .	70
4.5	Plots of the linear regression for sulcal width between methods per sulcus.	71
4.6	Vertex-wise partial correlation coefficients between age and width.	74
5.1	Histogram reporting the age distribution.	79
5.2	Pie charts showing the sample distribution by scanner.	80
5.3	Scatter plots for the thickness in gyral and sulcal lines along with the predictions of the linear mixed-effects models.	82
5.4	Scatter plots for the sulcal and gyral length with age along with their linear regressions.	84
5.5	Vertex-wise maps of the Pearson's r for age and width.	87

LIST OF TABLES

3.1	Coefficient of determination, slope coefficients and associated T-values for the regressions of the longitudes obtained by the different methods and the reference values (i.e., BrainVISA).	51
3.2	Comparison of the values of the logarithms of mean Hausdorff and maximum Hausdorff distances yielded by the different methods.	54
4.1	Statistics of the sulcal width comparisons.	72
4.2	Intraclass correlation coefficients estimating the resemblance between two different measures of sulcal width for the same subject.	73
4.3	Root mean square errors between test and retest measures for each method and sulcus.	74
5.1	Results of the interaction between age and location (sulcus/gyrus) for cortical thickness per lobe.	81
5.2	Results of the correlation between age and length in gyral and sulcal regions per lobe.	85

ACRONYMS

- 3D** three-dimensional.
- CFT** Cluster Forming Threshold.
- CSF** Cerebrospinal Fluid.
- CT** Cortical Thickness.
- CV** Cortical Volume.
- CWP** Cluster-Wise Probability.
- EDT** Euclidean Distance Transform.
- EEG** Electroencephalography.
- FA** Flip Angle.
- FDR** False Discovery Rate.
- FO** Fold Opening.
- FOV** Field of View.
- GI** Gyrification Index.
- GM** Gray Matter.
- GPDM** Geodesic Path Density Map.
- HCP** Human Connectome Project.
- ICC** Intraclass Correlation.
- IT** Inversion Time.
- LGI** Local Gyrification Index.
- LM** Local Maxima.
- MEG** Magnetoencephalography.
- MRI** Magnetic Resonance Imaging.
- OASIS** Open Access Series of Imaging Studies.

RMSE Root Mean Square Error.

ROI Region Of Interest.

SA Surface Area.

SBM Surface-Based Morphometry.

SVZ Subventricular Zone.

SW Sulcal Width.

T1w T1-weighted.

TE Echo Time.

TR Repetition Time.

TRACE Topological Graph Representation for Automatic Sulcal Curve Extraction.

VBM Voxel-Based Morphometry.

VZ Ventricular Zone.

WM White Matter.

SUMMARY

The cortex of the human brain is highly convoluted. These characteristic convolutions present advantages over lissencephalic brains. For instance, gyrification allows an expansion of cortical surface area without significantly increasing the cranial volume, thus facilitating the pass of the head through the birth channel. Studying the human brain's cortical morphology and the processes leading to the cortical folds has been critical for an increased understanding of the pathological processes driving psychiatric disorders such as schizophrenia, bipolar disorders, autism, or major depression. Furthermore, charting the normal developmental changes in cortical morphology during adolescence or aging can be of great importance for detecting deviances that may be precursors for pathology. However, the exact mechanisms that push cortical folding remain largely unknown.

The accurate characterization of the neurodevelopment processes is challenging. Multiple mechanisms co-occur at a molecular or cellular level and can only be studied through the analysis of ex-vivo samples, usually of animal models. Magnetic Resonance Imaging can partially fill the breach, allowing the portrayal of the macroscopic processes surfacing on in-vivo samples.

Different metrics have been defined to measure cortical structure to describe the brain's morphological changes and infer the associated microstructural events. Metrics such as cortical thickness, surface area, or cortical volume help establish a relation between the measured voxels on a magnetic resonance image and the underlying biological processes. However, the existing methods present limitations or room for improvement.

Methods extracting the lines representing the gyral and sulcal morphology tend to over- or underestimate the total length. These lines can provide important information about how sulcal and gyral regions function differently due to their distinctive ontogenesis. Nevertheless, some methods label every small fold on the cortical surface as a sulcal fundus, thus losing the perspective of lines that travel through the deeper zones of a sulcal basin. On the other hand, some methods are too restrictive, labeling sulcal fundi only for a bunch of primary folds.

To overcome this issue, we have proposed a Laplacian-collapse-based algorithm that can delineate the lines traversing the top regions of the gyri and the fundi of the sulci avoiding anastomotic sulci. For this, the cortex, represented as a 3D surface, is segmented into gyral and sulcal surfaces attending to the curvature and depth at every point of the mesh. Each resulting surface is spatially filtered, smoothing the boundaries. Then, a Laplacian-collapse-based algorithm is applied to obtain a thinned representation of the morphology of each structure. These thin curves are processed to detect where the extremities or endpoints lie. Finally, sulcal fundi and gyral crown lines are obtained by eroding the surfaces while preserving the structure topology and connectivity between the endpoints. The assessment of the presented algorithm showed that the labeled sulcal

lines were close to the proposed ground truth length values while crossing through the deeper (and more curved) regions. The tool also obtained reproducibility scores better or similar to those of previous algorithms.

A second limitation of the existing metrics concerns the measurement of sulcal width. This metric, understood as the physical distance between the points on opposite sulcal banks, can come in handy in detecting cortical flattening or complementing the information provided by cortical thickness, gyrification index, or such features. Nevertheless, existing methods only provided averaged measurements for different predefined sulcal regions, greatly restricting the possibilities of sulcal width and ignoring the intra-region variability.

Regarding this, we developed a method that estimates the distance from each sulcal point in the cortex to its corresponding opposite, thus providing a per-vertex map of the physical sulcal distances. For this, the cortical surface is sampled at different depth levels, detecting the points where the sulcal banks change. The points corresponding to each sulcal wall are matched with the closest point on a different one. The distance between those points is the sulcal width. The algorithm was validated against a simulated sulcus that resembles a simple fold. Then the tool was used on a real dataset and compared against two widely-used sulcal width estimation methods, averaging the proposed algorithm's values into the same region definition those reference tools use. The resulting values were similar for the proposed and the reference methods, thus demonstrating the algorithm's accuracy.

Finally, both algorithms were tested on a real aging population dataset to prove the methods' potential in a use-case scenario. The main idea was to elucidate fine-grained morphological changes in the human cortex with aging by conducting three analyses: a comparison of the age-dependencies of cortical thickness in gyral and sulcal lines, an analysis of how the sulcal and gyral length changes with age, and a vertex-wise study of sulcal width and cortical thickness.

These analyses showed a general flattening of the cortex with aging, with interesting findings such as a differential age-dependency of thickness thinning in the sulcal and gyral regions. By demonstrating that our method can detect this difference, our results can pave the way for future in vivo studies focusing on macro- and microscopic changes specific to gyri or sulci. Our method can generate new brain-based biomarkers specific to sulci and gyri, and these can be used on large samples to establish normative models to which patients can be compared. In parallel, the vertex-wise analyses show that sulcal width is very sensitive to changes during aging, independent of cortical thickness. This corroborates the concept of sulcal width as a metric that explains, in the least, the unique variance of morphology not fully captured by existing metrics. Our method allows for sulcal width vertex-wise analyses that were not possible previously, potentially changing our understanding of how changes in sulcal width shape cortical morphology.

In conclusion, this thesis presents two new tools, open source and publicly available,

for estimating cortical surface-based morphometrics. The methods have been validated and assessed against existing algorithms. They have also been tested on a real dataset, providing new, exciting insights into cortical morphology and showing their potential for defining innovative biomarkers.

THESIS OUTLINE

The present dissertation introduces two new morphometry methods that aim to expand the information researchers can extract from structural Magnetic Resonance Imaging. The thesis is organized into six chapters. Chapter 1 contains an introduction providing basic biological and technical background. In particular, the first part of the introduction covers the bases of cortical morphogenesis, giving insight into the biological mechanisms that lead to cortical folding and why it is necessary to measure morphological features. Then, the second part of the introduction covers how these metrics can be estimated through Magnetic Resonance Imaging, explaining their strengths and limitations.

Having stated the importance of measuring cortical morphology, the main metrics, and their limitations, Chapter 2 introduces the motivation of the work, as well as the objectives of the thesis.

Chapter 3 presents the journal publication corresponding to the first of the developed methods. This tool applies a Laplacian-collapse-based algorithm to obtain the lines representing the cortical surface's sulcal fundi and gyral crowns while avoiding small anastomotic sulci. Along with a detailed description of the method, the chapter presents the validation of the algorithm, comparing the obtained results against three well-known sulcal line extraction algorithms.

Then, Chapter 4 includes the publication of the second developed method: a tool for generating vertex-wise sulcal width maps on cortical surfaces. As in the previous chapter, the proposed algorithm is explained and validated in detail. In this case, validation includes the assessment of the algorithm in a simulated sulcus and the comparison of the method with two widely-used sulcal width estimation tools on a test-retest database.

Chapter 5 aims to provide a biological application of the developed algorithm. Thus, both tools are applied to a cohort of aging participants to measure morphological features using the proposed algorithm.

Finally, Chapter 6 presents a general discussion of the developed methods and their biological relevance, stating the existing limitations and future lines. Following this discussion, the conclusions of the work are available in Chapter 7.

1. INTRODUCTION

1.1. Key Concepts on Cortical Folding and Neurodevelopment

From a biomedical engineering perspective, we are interested in applying our methods and ideas to help solve a problem. However, sometimes we solely focus on the engineering aspects of the issue at hand, and we do not pay enough attention to the biological grounds in which our problem may be rooted. Bearing this potential engineer's hazard in mind, this work is fully based on biology. That is, the central focus of this thesis is the development of new methods that provide fine-grained morphological information about the human brain cortex. These methods can be applied to quantify human variability in previously uncharted aspects of cortex morphology and the relationship of said variability with development, disease, and function. This work builds on the typical folded, also called gyrified, shape of the human cortex. A complex, not fully understood, neurobiological process leads to this folded shape. The following sections contain a brief introduction to the ontogenesis of human cortex folding, as it provides the biological fundament on which this thesis is built.

1.1.1. Morphogenesis and Gyrification of the Human Cortex

The cortex of the human brain is highly convoluted. Folded brains present significant advantages over brains without convolutions. For instance, gyrification allows an expansion of cortical surface area without greatly increasing the cranial volume, thus facilitating the pass of the head through the birth channel. Additionally, the lissencephalic brain would require longer axons to connect different cortical regions, thus increasing the metabolic costs and reducing the speed of information exchange [10]. It is essential to state that the forces governing the gyrification process are far from random. There might be variability between subjects and even between hemispheres of the same subject; still, the primary sulci are preserved with remarkable consistency across subjects [11] and are highly reproducible at the intra-species level [12].

The gyrification process occurs during the first stages of embryonic development. Initially, the brain is formed by two smooth hemispheres with the ventricles filled with Cerebrospinal Fluid (CSF). These ventricles are surrounded by a tissue layer called Ventricular Zone (VZ) populated with progenitor cells [12]. These cells function as neural stem cells; they can duplicate symmetrically to form new progenitor cells or asymmetrically to create a progenitor cell, and a neural precursor [13, 14]. These cells also form a scaffolding that helps in the migration of the new neural precursors towards the outer layers of the cortical plate [12], as the progenitor cells form elongated fibers that grow radially (see Figure 1.1). The Subventricular Zone (SVZ) appears as a region between the cortical plate and the VZ

and contains the intermediate progenitor cells. These cells can divide to form two new intermediate progenitors or two new neurons, which will migrate through the scaffolding provided by the radial progenitor cells [10, 14]. Some of the radial progenitor cells in the SVZ lose the attachment to the ventricular shell, becoming basal radial progenitors. The cytoarchitectural organization that arises from the development will determine the pattern of brain convolutions [15, 16].

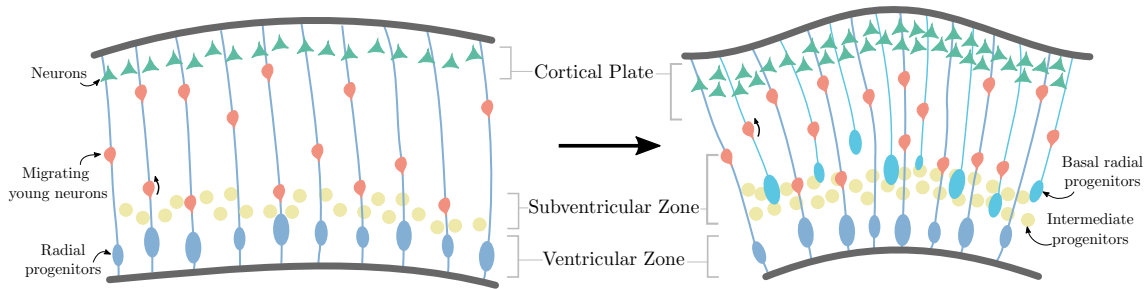


Figure 1.1: Development of a cortical gyrus during early embryonic stages. Initially, the different zones that form the brain are thin. The progenitors duplicate in the ventricular and subventricular zones to form new progenitors and neurons. These neurons migrate through the radial progenitor cells toward the cortical plate. In the late stages of development, the subventricular zone and the cortical plate are enlarged, and the folds are appreciable. Some radial progenitor cells have lost the connection to the ventricular surface, forming the basal radial progenitors.

The exact mechanisms leading to cortical gyrification are not well understood. However, studying the biological processes underlying folding is of great importance in attempting to comprehend typical and atypical brain neurodevelopment. The following subsections summarize some of the most important morphogenesis theories. More comprehensive reviews can be found in the following references [10, 11, 14, 17–19].

1.1.1.1. External Constraints

An early hypothesis on the origin of this gyrification process states that the cortex folds due to the existence of external constraints, i.e., the skull [20]. This hypothesis posits that the tangential expansion of the cortex inside a constrained space, as is the cranial volume, causes brain folding (see Figure 1.2). Some scholars disagree with this hypothesis. Barron [21] exposed that creating additional space inside the developing skull by surgically removing non-cortical brain areas does not alter folding patterns. Furthermore, the skull must be stiff enough to constrain the tangential cortical growth. This is not the case, as skull ossification does not occur until the late stages of development [10].

The current consensus states that, while external constraints contribute, they are insufficient to form main cortical folds. [14, 22–24].

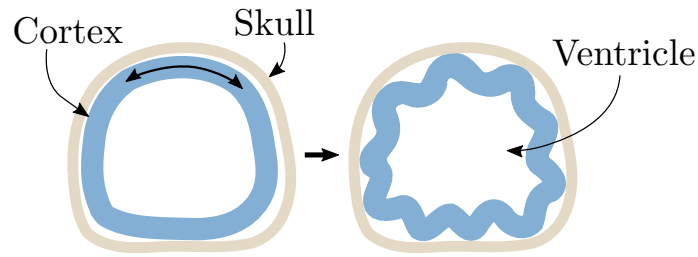


Figure 1.2: Cortical folding model based on external constraints. In this case, the skull is bounding the growth of the cortex, creating the folds of the brain.

1.1.1.2. Differential Tangential Expansion

Once these external constraints theories lost momentum, the focus shifted to the intrinsic mechanisms of the brain. One of the first hypotheses suggests that the cortex folds due to the asymmetric expansion between cortical layers [25]. Assuming that the outer layers are tightly bound to the deeper layers, they will create a mechanical stress gradient if the outer layers expand faster tangentially. This gradient would cause the cortex to buckle, thus forming the sulci (see Figure 1.3).

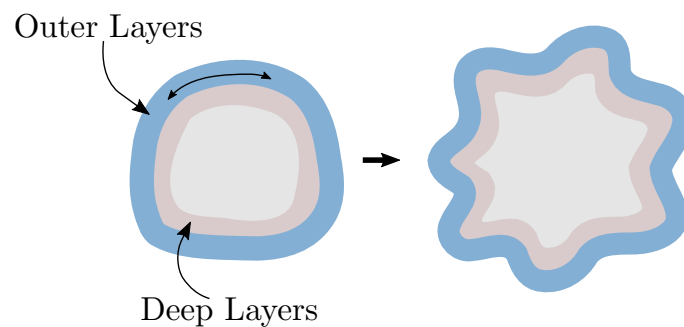


Figure 1.3: Differential tangential expansion. The different layers are bounded to the others. The outer layers grow faster than the deep ones, causing the outer layers to begin to buckle.

Taking this hypothesis as a starting point, recent studies have proposed different models for folding based on differential tangential expansion. Mathematical simulations and experiments with hydrogel solutions demonstrate that, in the appropriate situation, a single layer can fold when it is attached to a central core from which it cannot delaminate [26–28].

However, these models based on a single elastic layer have limitations in replicating the intra-species reproducibility of the primary folds consistently and accounting for the genetic component of the patterns [14]. Another objection to this hypothesis is that it is unclear that the outer and inner cortical layers present differences in stiffness during this developmental period [29]. Also, there is a lack of evidence that the differential expansion is the cause of gyrification and not the consequence [11, 30, 31].

1.1.1.3. Axonal Tension

First proposed in Van Essen [30], the axonal tension hypothesis states that fiber bundles that directly connect different parts of the cortex generate a tension that pulls together the opposite sides of gyral folds at specific locations (see Figure 1.4). The resulting configuration would have a minimized wiring length while preserving the connectivity, optimizing the sharing information efficiency [30]. This hypothesis is sustained by the fact that the white matter is under tension [32, 33] and addresses a problem present in the previous models: it can explain the reproducibility of the primary sulci.

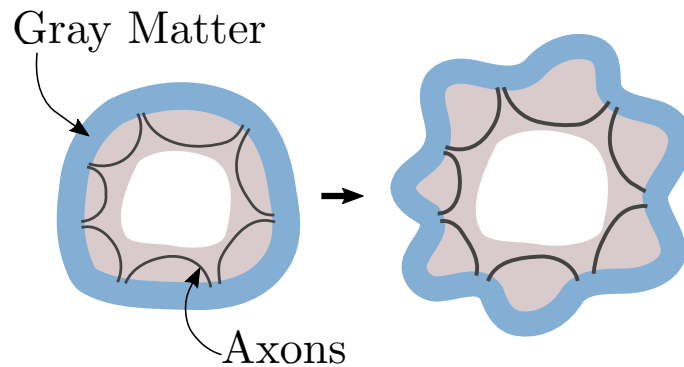


Figure 1.4: Cortical folding model based on axonal tension. The pulling forces that the fiber bundles exert on the cortex model brain folding.

Nevertheless, as in the previous scenarios, this theory presents limitations. In a study using ferrets, Xu *et al.* [29] suggests that axons run parallel to the sulcal walls instead of perpendicular, as the hypothesis suggests. Also, the researchers found that making a cut in a gyrus of a developing ferret brain does not cause the fold to open, indicating that the axonal tension is not strong enough to drive the folding.

1.1.1.4. Hybrid Models

As it arises from the many limitations of the previous models, it seems reasonable to admit that cortical folding is not the product of a single force but a combination of mechanisms, known or yet uncharted, acting in an unknown order. This hypothesis has grown in importance in the literature of the last years, with more models proposing a combination of forces as the cause of folding [10, 15, 31, 34]. To illustrate the section, I will delve into three examples.

First, in the work by Toro and Burnod [31], they present a hypothesis that combines the differential tangential expansion [25] with the axonal tension [30]. This computer model considers that folding arises as a mechanism to reduce the pressure caused by the tangential expansion of the cortical plate, understood as an elastic ring. The radial glia fibers connect this ring to a central core, creating spatial variations of thickness and stiffness in the tissue depending on the fiber density [31]. Variations in these parameters lead

to folds occurring in reproducible locations, proposing a theoretical basis for combining the two most accepted mechanisms for cortical gyrification [25, 30].

On his side, Van Essen [34] presents an update of his own paper from 1997 [30]. In this new work, he proposes a new model named “differential expansion sandwich plus” sustained on a combination of five different principles. The first one is that the tangential growth of the cortex is guided by a radial tension in the gray matter. Second, the existence of a differential tangential expansion pushes for gyral folding. Third, the tangential tension in the outer cortical layer combines with the trans-sulcal adhesion of the pia and arachnoid layers to boost gyrification. Fourth, cell proliferation and migration patterns affect cortical morphometry, influencing the positioning of sulci and gyri. Finally, tension along the central nervous system decreases wiring length, constrained by the limitations imposed by axonal interdigitation [34]. This update complements the axonal tension hypothesis [30] with the differential tangential expansion theory [25], or the external constraints caused by the meninges.

Finally, Striedter *et al.* [10] hypothesize that when the young neurons migrating along the radial progenitors (see Figure 1.1) reach the cortical plate, they start pushing the neighboring cells causing a tangential expansion of the outer cortical layers. When the tangential expansion is wide enough, the cortex begins folding outwards or inwards depending on factors such as the pulling forces exerted by the radial scaffolding of the progenitor cells, the tissue elasticities, or external forces like the meninges.

These works exemplify the complexity of understanding the forces driving cortical folding. Many other studies propose different combinations of mechanisms, exploring the issue from a molecular level [35], a cellular perspective [10], or mathematical simulations [24, 36].

1.1.2. Cortical Layers

During the early stages of neurodevelopment, new neurons generated in the VZ start migrating to the outer layers of the cortical plate (see Figure 1.1). On these outer layers, neurons finish their migration and develop dendritic and axonal arbors [19]. This differentiation will result in a laminated organization divided into cortical layers. The adult brain is mainly organized into six layers, each of them named with a Roman numeral from I to VI from the outer to the inner layers (see Figure 1.5), and their exact organization is related to the processes of cortical folding [15, 34, 37]. These layers are generated in chronological order during neurodevelopment. Thus, the deepest layers appear earlier, and the following ones start piling up [19, 38]. This principle applies to every layer except for layer I, formed by the Cajal-Retzius cells, which are the first neurons created [19].

As mentioned before, the main portion of the cortex is formed by the so-called isocortex or neocortex, composed of six distinct cellular layers. There is an exception for this organization of the isocortex: the motor cortex has no IV layer discernible in adults

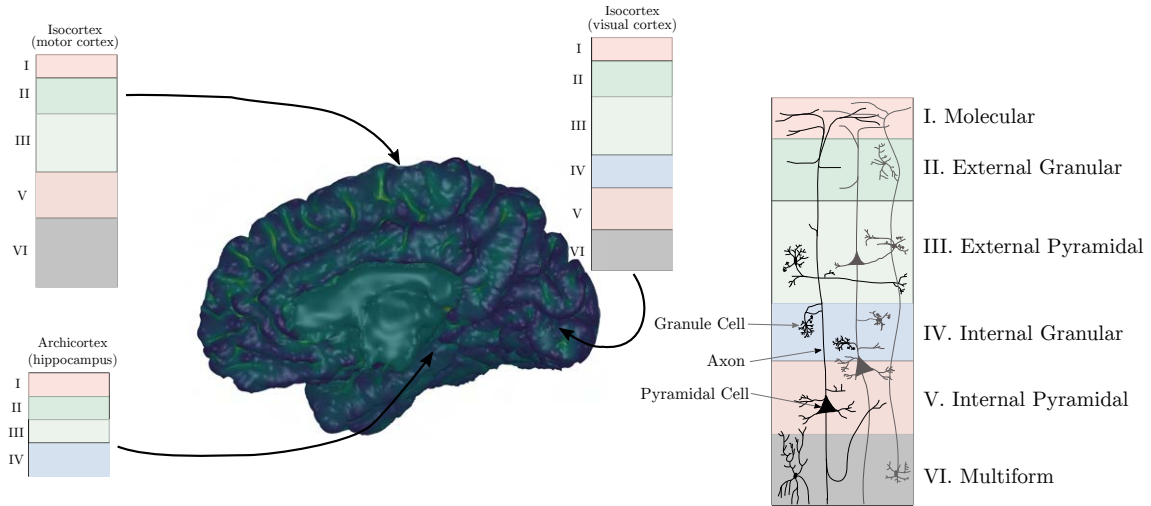


Figure 1.5: Schematic depiction of the cortical layer organization.

[39–41]. On their side, other regions, such as the hippocampal cortex, present only three to four layers [40] (see Figure 1.5). These differences at the cellular level are used to define parcellations of the cerebral cortex. Depending on the exact organization of the cortical layers, the human cortex can be divided into different cytoarchitectural areas, that gave rise to the Brodmann atlas [12, 39, 40].

1.1.3. Relationship Between Brain Gyrification and Pathologies

The most obvious implications of anomalous patterns in the gyrification process are those where the brain presents loss or excess of folds as it can be the lissencephaly (absence or simplification of gyri in the cortex), polymicrogyria (presence of an excessive amount of shallow folds), microcephaly (reduction in head circumference), or macrocephaly (abnormally large head) [19, 35]. These disorders are usually related to severe cases of intellectual disability, epilepsy, or autism [35, 42].

Besides the more apparent malformations, anomalies in the neurodevelopmental processes linked to the folding or the organization of cortical layers are subtle. It has been reported that major psychiatric disorders like schizophrenia originate during neurodevelopment, presenting abnormalities at the cellular level, for instance, in the dendrites of cortical layer III [43]. In parallel, schizophrenia has been related to alterations in the gyrification patterns and cortical volumes [44–46]. Similar findings appear when studying autism, where changes at the cellular level in different regions and layers of the cortex can be observed [47, 48] along with anomalies at a macroscopic level [46, 49–51]. The same can be observed in bipolar disorders [46, 51, 52], or major depression disorders [46, 51, 53, 54]. Moreover, studies have also found atypical sulcal patterns in patients with attention deficit and hyperactivity disorder [55, 56].

Hence, attending to the literature, it is reasonable to say that the level of gyrification

and the arrangement of such gyri can provide insights into possible cerebral dysfunction besides posing as macroscopic landmarks for functional and cytoarchitectonic areas [57]. Also, gyrification patterns can provide a more static neurodevelopmental marker than cortical volume, as these patterns are less subject to change with age [51].

1.2. Assessing the Cortical Anatomy Using Magnetic Resonance Imaging

As we have stated in the previous epigraph, the study of gyrification can provide essential insights into the progress of pathologies and normal neurodevelopment. The existing strategies to examine microscopic neurobiological processes associated with gyrification rely on the analysis of *ex-vivo* samples, which greatly hinders such study in human populations. A reasonable alternative for this is the study of the folding characteristics at a macroscopic level, analyzing the properties of gyri arrangement and thickness. This kind of study can be performed thanks to Magnetic Resonance Imaging (MRI), as it allows a clear distinction of the inner tissues of, in this case, the brain in *in-vivo* populations.

MRI is a non-invasive medical imaging modality that generates three-dimensional (3D) representations of the internal anatomy of the head. Different modalities of MRI can be used to measure various properties of the brain, such as functional MRI, which is based on the different magnetic properties of the oxygenated and deoxygenated hemoglobin to measure the neuronal activity [58], or diffusion-weighted imaging, that measures the water movement inside the brain to infer its structural organization [59]. In this dissertation, I will focus on anatomical or structural MRI.

As its name indicates, this modality aims to characterize the gross anatomy of the brain, specifically the three main components that form it: Gray Matter (GM), White Matter (WM), and Cerebrospinal Fluid (CSF). The basis of this modality is to exploit the magnetic properties of the protons, which are abundant in the brain due to its high content in water and, therefore, the presence of hydrogen nuclei. Besides water concentration, MRI scanners are sensible to other tissue-specific macroscopic magnetic properties as the T1 and T2 relaxation parameters [60]. Measuring these properties MRI scanners can generate images with different tissue contrasts that provide complementary information, being the so-called T1-weighted (T1w) images the most common acquisition for structural MRI (see Figure 1.6).

1.2.1. Working with Magnetic Resonance Images

These 3D images are organized on a regular Cartesian grid of voxels (understood as volumetric pixels), each of them containing a value that reflects the intensity measured in that position. Usually, these volumes need to be preprocessed to correct the different artifacts they present, such as bias field and inhomogeneities [61]. Once the images are corrected, a wide variety of possible analyses and operations can be applied to the data. We can

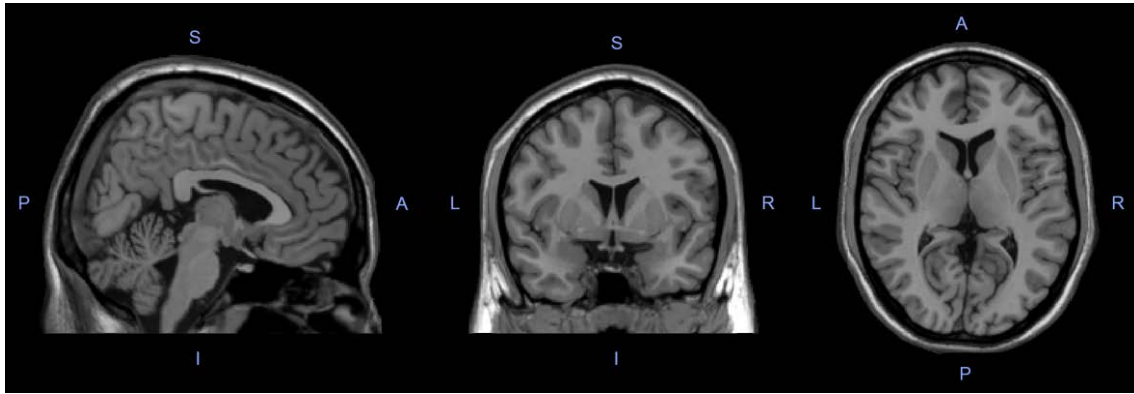


Figure 1.6: Example of brain acquisition using MRI. From left to right, the slices are sagittal, coronal, and axial. Regions associated with white matter present lighter gray colors. Gray matter areas are generally correspondent with darker gray shades. Finally, cerebrospinal fluid is represented in black. **Note:** A, P, S, I, L, and R refer to anterior, posterior, superior, inferior, left, and right, respectively.

divide them into three main groups: voxel-based approaches, surface-based approaches, or region-of-interest analyses.

1.2.1.1. Voxel-Based Approaches

This kind of analysis consists of operating on the 3D Cartesian grid where the images are presented. The main advantage of this approach is its relative simplicity and computation efficiency. As the images are located in a 3D grid, the correspondence between neighbors is fixed, making it easy to adapt well-known morphological 2D image processing operations to this field.

Among the voxel-based analyses available, the most popular one is Voxel-Based Morphometry (VBM). Succinctly, VBM consists of registering the 3D volumes to a common stereotactic space to remove inter-subject variability (spatial normalization), identifying the Gray Matter (GM) or White Matter (WM) tissues (segmentation), and comparing the local concentration of the tissue of interest among groups of subjects, for example, a healthy group against a pathological one [62, 63]. This approach has been used in an endless number of publications and applied to multiple pathologies [64–70], just a simple search of the terms VBM or Voxel-Based Morphometry on PubMed¹ generates over 7,236 results, around 2,000 of them just for the period between 2019 to 2022.

However, despite its popularity and undeniable usefulness, voxel-based approaches present some limitations that need to be considered. For starters, in VBM, misalignments when registering to a common template can alter the results. This is why the algorithm and template selected for spatial normalization might greatly impact the outcome of a study [71–73]. Misclassification errors, assigning a wrong label to a voxel in the segmentation step, can also be a source of errors. In addition, the interpretation of VBM results can also

¹<https://pubmed.ncbi.nlm.nih.gov/>

be puzzling. For instance, there are cases where it is not obvious if the differences in GM arise due to a reduction in cortical thickness or because of the inter-subject variability in the folding pattern [74] as shown in Figure 1.7.

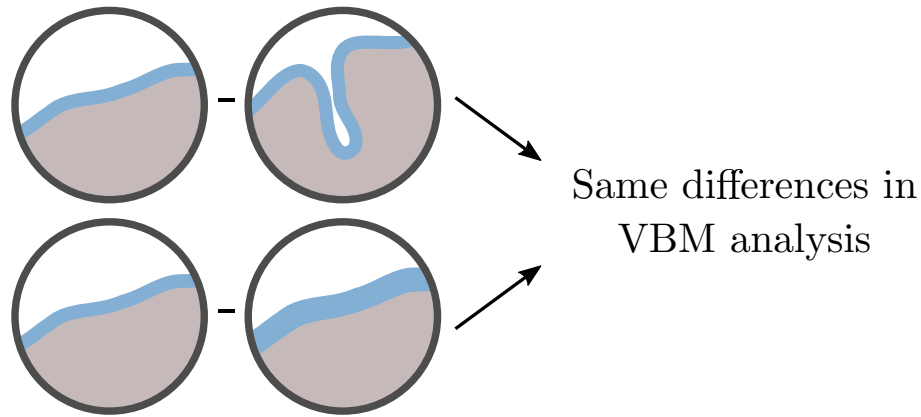


Figure 1.7: Limitations of interpretation of Gray Matter Voxel-Based Morphometry (VBM) results. The differences in Gray Matter depicted in the upper line, between a thin straight region and a thin convoluted one, are equivalent to those in the bottom line, showing a thin straight region against an equally unfolded but thicker region.

Further, due to the intricate morphology of the human cortex, some operations can be challenging to perform on a voxel space. For example, measuring the geodesic distance between two cortical points would require complex proceedings, as measuring a simple Euclidean distance would underestimate the real value, especially when those two points are located on opposite sulcal banks [75].

1.2.1.2. Surface-Based Approaches

The drawbacks appearing when operating at the voxel level can be partially solved using surface-based approaches. These approaches are based on the extraction of meshes that enclose the CSF/GM and GM/WM cortical interfaces. The most popular and widely-used tool for generating and analyzing these surfaces is FreeSurfer [76, 77], although there are other image processing suites such as BrainSuite [78] or BrainVISA [79]. The basic steps to create these surfaces are somewhat analogous among the different tools. The T1-weighted (T1w) image is corrected to remove possible variations in the intensity across the volume. Then, a skull-stripping step is performed to restrict the analysis and processing to the voxels belonging to the brain. On this masked volume, the algorithm applies a classification method to label the voxels attending to their position and intensity, differentiating between CSF, GM, and WM regions. For each hemisphere, an initial surface is adjusted to the outer boundary of the WM segmentation, which is right after refined using the intensities of the corresponding voxels in the input volume. This refined surface is commonly known as “white surface”. Finally, the surface covering the CSF/GM (known as “pial surface”) is created by expanding the white surface to the outer boundary of the GM segmentation and refining it (see Figure 1.8).

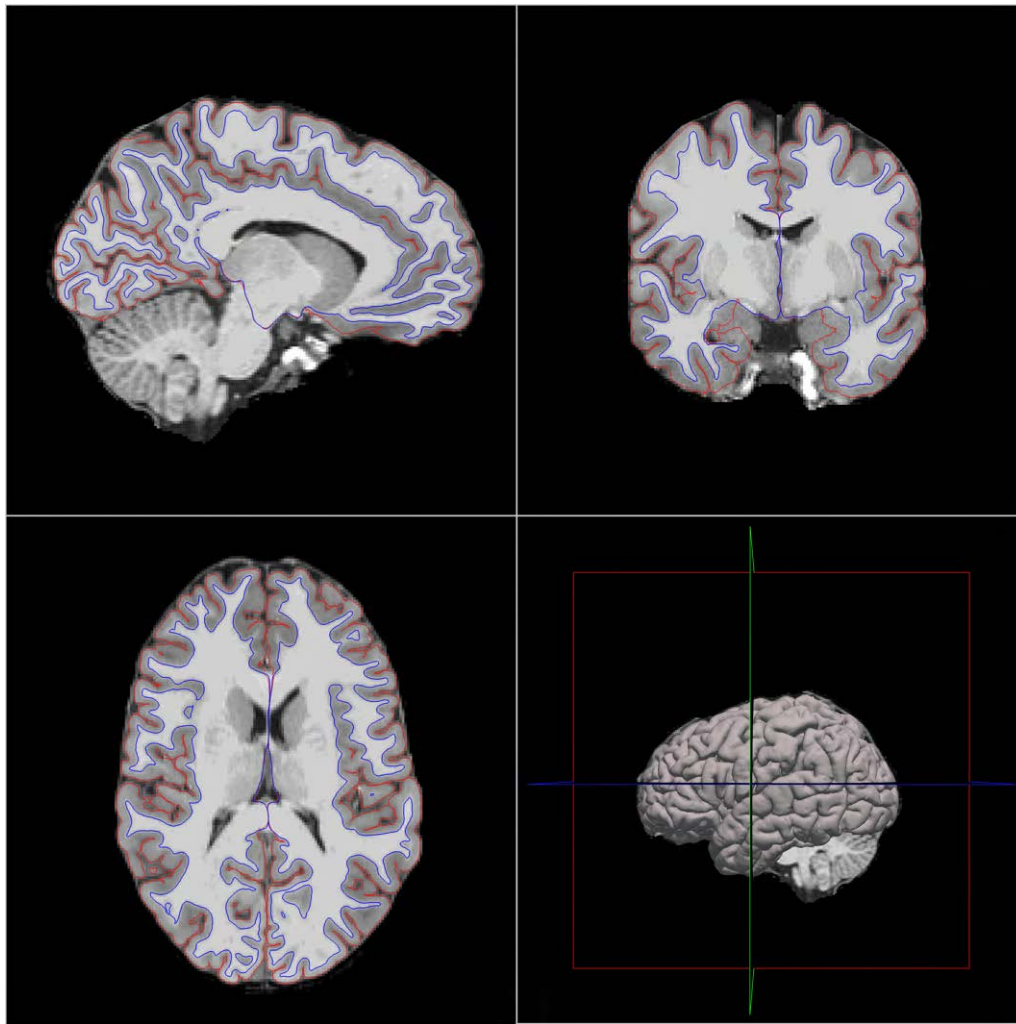


Figure 1.8: Cortical surfaces extracted for a single subject using FreeSurfer. The image shows, from left to right and up to down, the sagittal, coronal, axial, and 3D views of the T1w image overlaid with both “white” and “pial” surfaces. The lines in red and blue correspond to the surfaces created in the CSF/GM and GM/WM interfaces respectively. The right bottom panel depicts a 3D render of the “pial” surface of the left hemisphere.

The resulting surfaces or meshes are composed of a variable number of vertices and triangular faces. The vertices represent the position of the points that form the surface in a 3D space, while the faces express the direct connections between said vertices as depicted in Figure 1.9. Surface-Based Morphometry (SBM), which can be understood as the equivalent to VBM in the vertex space, presents some benefits with respect to its voxel counterpart. The topology of each cortical hemisphere can be represented as a 2D closed manifold [80] and then mapping the points to a regular sphere (actually, a uniform subdivision of an icosahedron projected to a sphere). These spheres present a straightforward geometry; hence, registration of the cortical structures between spheres can be simpler than using 3D volumes [81]. There are different algorithms for this registration, although the base tends to be similar: estimate the deformation field to establish correspondences between the cortical markers of a moving sphere and an objective one [80, 82–84]. Once

the deformation is estimated, the maps of interest (cortical thickness, volume, surface area, etc.) can be projected to a common space by applying this same transformation, allowing vertex-wise statistical data analysis.

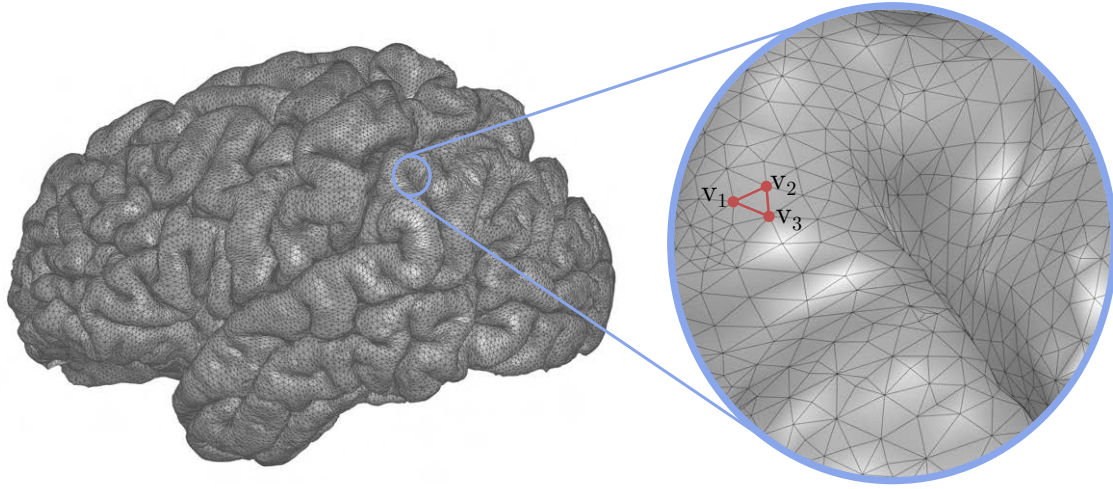


Figure 1.9: Representation of a 3D cortical surface depicting the wireframe formed by the vertices and triangular faces. On the right, a closeup highlighting a face and the vertices that form it (v_1 , v_2 , and v_3).

Despite the increase in computation complexity, operating in the vertex space presents some advantages with respect to the voxel space in addition to the above-mentioned increased registering capability. The meshes accurately capture the cortical topology, as it can be modeled as a corrugated 2D sheet. This permits to calculate the normal directions of the surface at each point, being useful, for instance, in the estimation of the origin of signals in Electroencephalography (EEG) or Magnetoencephalography (MEG) [85]. Another benefit of the surface approaches is that estimating Euclidean and geodesic distances between cortical points is now straightforward, making it easier to identify the points in the same or in the opposite sulcal banks. These properties greatly facilitate the estimation of metrics related to cortical gyrification, which have a great interest, as we have seen in Section 1.1.3.

These meshes, due to their organization in vertices and faces, allow for the estimation of the so-called vertex-wise maps. These maps contain local information of a particular metric for each vertex in the surface and can be statistically compared using SBM. An example of these metrics would be the curvature map. This map is based on calculating the mean of the two principal curvatures on the triangles of the surface [86]. This is especially useful for locating the relative position of brain areas, extensively applied in surface registration methods [80, 82, 83].

1.2.1.3. Regions of Interest

There is an alternative to the vertex or voxel-wise analyses that allows for avoiding the problematic registration step, which is to analyze the target features for a given region. These regions are commonly defined according to anatomic [87, 88], or functional [89]

criteria. This approach is compatible with metrics estimated in the vertex or voxel spaces. On one hand, Region Of Interest (ROI) analyses allow to work in the individual native space of the subjects, so the statistical comparisons can be performed for multiple participants without performing a spatial registration to a stereotactic space. On the other hand, this methodology has multiple limitations. First, it relies on the correct labeling of the cortical regions. Second, if the values in each ROIs are averaged, the intra-region variability is not accounted for, which can lead to a loss of local information. Finally, the selection of the ROIs for each study must be carefully selected *a priori* and according to the hypotheses of the study.

1.2.2. Cortical Morphometry

As it has been mentioned, through MRI, scientists can obtain information about the inner structures of the brain. There are multiple image processing techniques to compute different cortical features and perform accurate morphometric analyses using them. These metrics provide complementary information on cortical morphology, improving the global macroscopic picture of brain changes during neurodevelopment or pathologies that can help to infer the differences at a microscopic level. In the current section, I summarize the most commonly used metrics and some of their limitations.

1.2.2.1. Surface Area

Surface Area (SA) is related to the sulcal morphometry, as an increase in gyrification implies an increase in cortical area. Local variations on SA can respond to the number of cortical columns and their organization (schematized in Figure 1.1). This is closely associated with the brain's neurodevelopment and functional specialization of the different regions [90–92]. Reductions in SA have been reported in patients with schizophrenia [3, 93] that might indicate anomalies at different neurodevelopmental stages such as the neural stem cells division or dendritic arborization. However, the specific reasons driving these results remain unclear [93].

SA is a metric inherent to the vertex space. Estimating these maps is straightforward in a 3D mesh but can be challenging in volumetric images. This can be done, pointwise, by computing the area of each triangular face of the surface and assigning to each vertex one-third of the sum of the areas of all faces that meet at that vertex [92]. Despite its simplicity, this approach presents a drawback, as the tessellation of the brain is not evenly distributed; gyral regions tend to be more plain, so fewer triangles are needed for their accurate representation, while the opposite happens in sulcal regions. This translates into bigger triangles in gyral regions and smaller in sulcal areas, meaning higher SA for the first and lower for the later. In addition, this metric should not be understood as a pointwise measure but as a local or regional one. Therefore, the vertex-wise analysis of this metric can be confusing and needs to be performed with caution as the typical

interpolation and smoothing steps included in every SBM analysis make no sense for vertex-wise SA analyses [92].

As an alternative, some works propose indirect measures for the area, based, for example, on the expansion or contraction when registering a mesh to a standard template [94–96]. The main inconvenience of this approach is that the obtained values do not represent a real physical dimension but one relative to the template surface, so the interpretation of results only makes sense as a comparison [92].

1.2.2.2. Cortical Thickness

Cortical thickness (CT) is the most popular and widely-used vertex-wise metric in the literature. It can be seen as the distance that separates the outer (GM/CSF interface) and inner (GM/WM interface) layers of the cortex. This measure appears to be related to the regional neuronal density in the cortex [97]. We have stated that the number of cortical columns mediates the size of the cortical surface; however, its thickness appears to be modulated by the number of cells in each column [90, 98], appearing as complementary features. Hence, it is of great interest in the study of neurodevelopment, the changes in the brain through aging or natural processes, and the progress of numerous psychiatric or neurodegenerative disorders. Multiple studies report CT differences in patients with Alzheimer’s disease [99, 100], Parkinson’s disease [101], schizophrenia [3, 45, 102] or even pathologies such as children’s dyslexia [103], to mention some. In the field of normal development, we can find examples of differences in CT during adolescence [104, 105], or pregnancy [6, 105, 106] among multiple other studies.

In terms of estimation, CT has been extracted both in surface [107] and volumetric [108] methods. Measuring the CT in a 3D grid presents some inconveniences, as estimating the normal directions from one tissue to the other to calculate the shortest distances between them is not evident in this space. Methods like the one in Das *et al.* [108] tackle the issue by using prior constraints and minimally deforming solutions in finding correspondences between the points of both interfaces. In the case of surface-based methods, the solution is simpler. Despite existing different ways to define the Cortical Thickness [109], they are all based on finding a correspondence between the pial and white surfaces. Most of the developed algorithms typically define the distance between each vertex of the white surface to the closest part in the pial surface (vertex or face). This procedure is repeated to find the minimal distance from each point in the pial surface to the white mesh. Then, both distances are averaged to obtain the final estimation of the cortical thickness in each point [107] (see Figure 1.11A).

Despite its apparent simplicity, interpreting changes in CT can be challenging, as different biological processes can contribute to those. Changes in this feature can be related to atrophy in the affected regions, synaptic pruning [104, 105], differences in GM myelination or a lack of contrast between in the GM/WM interface [98]. This last scenario can be especially difficult in the analysis of images from older participants, as the tissues’

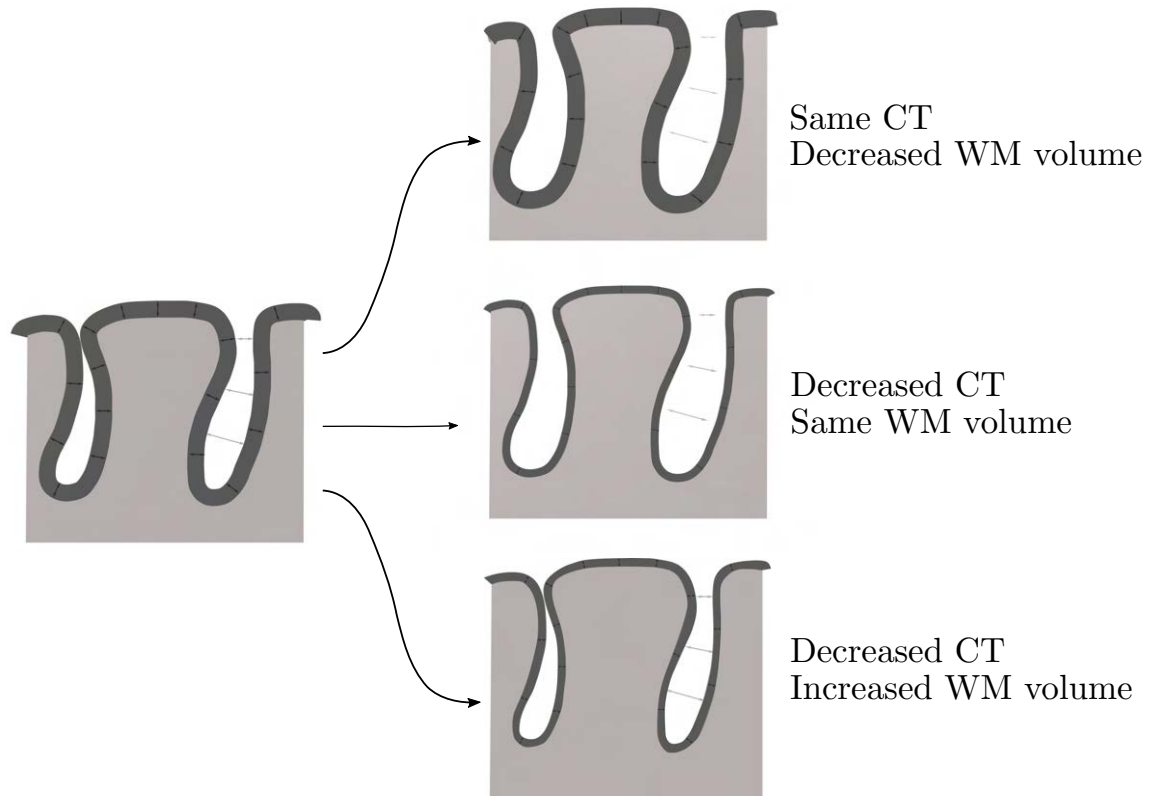


Figure 1.10: Different scenarios representing the limitations on the interpretation of cortical thickness (CT).

water content diminishes with age, leading to a lower difference in the proton density of GM and WM and, therefore, a poorer contrast [110]. An additional problem of this metric is the one depicted in Figure 1.10, as CT is sensitive to changes in the cortex width, but it might ignore other important anatomical changes like a widening of the sulci when it is not purely related to the GM thinning.

1.2.2.3. Cortical Volume

Cortical Volume (CV) measures the amount of GM in a given cortical region. This metric is widely popular because of the broad usage of VBM methods, where estimation of volume is effortless. Volume and thickness are frequently used indistinctly as markers for the cortical structure. Nevertheless, this assumption can be questionable, as volume can be understood as a product of thickness and area. Precisely, the estimation of CV in the vertex space is based on this property. Initially, FreeSurfer [76, 77] estimated volume as the multiplication of the area map by the thickness map for each surface vertex. The problem with this approach is that it tends to over- or underestimate the metric depending on the convexity of the surfaces [111]. The solution proposed by Winkler *et al.* [111] is to estimate the volume of each of the triangular prisms that the vertices in the pial and white surfaces form by decomposing the prisms into three tetrahedra (see Figure 1.11). This way, the volume can be univocally estimated, avoiding the aforementioned problems.

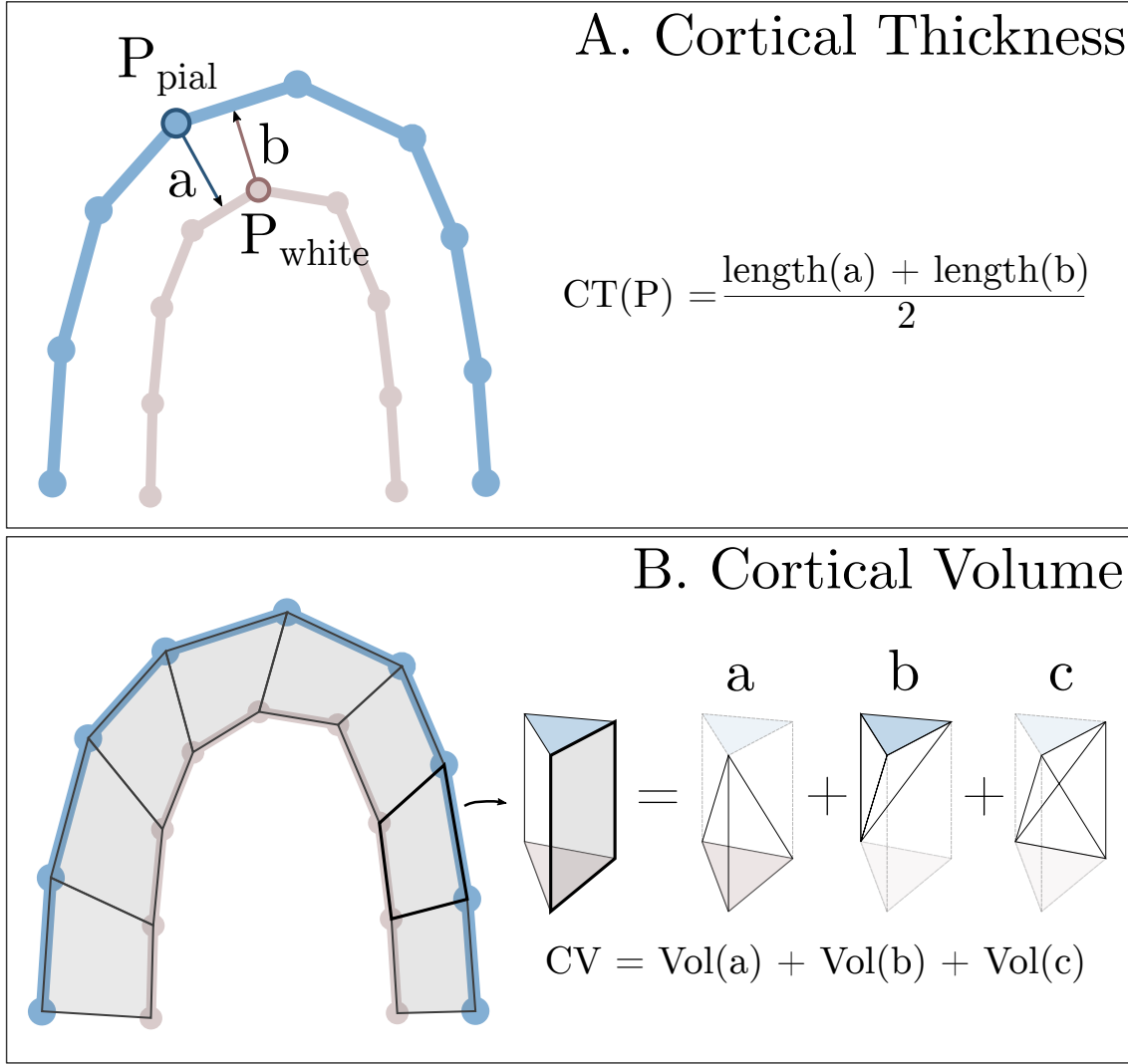


Figure 1.11: Scheme of the estimation of cortical thickness (CT) (A) and cortical volume (CV) (B).

The statistical analysis and interpretation of CV need to be cautious as well. As happens with surface area, volume is an areal quantity, so interpolation methods used need to be compatible [111].

1.2.2.4. Cortical Depth

Measuring the cortical depth can provide valuable information about brain organization, as there is evidence that deeper sulci are formed first compared to superficial ones, which appear later in the neurodevelopment [15], being those deep sulci more consistent and less variable across subjects [112]. This can also mean that deeper sulci, having an earlier origin, can be routed to functional areas [15, 113]. These properties, along with the fact that approximately 70% of the human cortex is buried in sulci [114] make depth a useful metric both for the study of neurodevelopment [113, 115–117] and the localization of cortical features [118–120].

There are different approaches to computing the cortical depth; however, the most common ones are based on the same principle: generating a zero-depth reference and estimating the distance of every point in the surface to this reference. Generally, this zero-depth reference is an outer hull that surrounds the brain covering the sulci without entering them, similar to how a rigid brain would fit into a smaller balloon. This way, methods estimate the distance from the mesh to the nearest point in the hull.

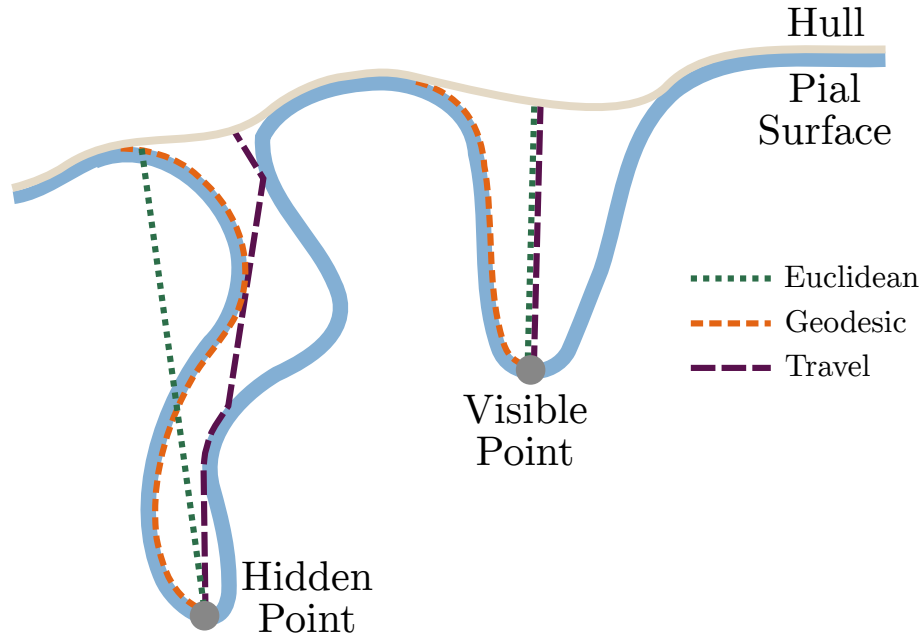


Figure 1.12: Representation of how the Euclidean (green), geodesic (orange), and travel (purple) depth work for a point hidden inside a convolution and a visible one.

There are three main choices for the depth metric (see Figure 1.12). The first one is the Euclidean distance, with the critical inconvenience that this metric would intercept the surface for most of the points lying in sulcal regions, thus underestimating the depth values. The second option is the geodesic distance, i.e., the shortest path following the surface morphology between the hull and any point on the surface. This metric presents the opposite problem to Euclidean distance, as it tends to overestimate the depth in certain regions, especially where the surface is irregular. The geodesic distance can also be unsuitable in some configurations of sulci, where the deepest values might not happen to meet in the fundi. The third option is the travel depth [121], initially conceived for estimating the depth in voxel images of macromolecules. This metric is a combination of geodesic and Euclidean distances. The path from one point to the other is geodesic in those stretches where the Euclidean distance would cross the surface and Euclidean where there is an unobstructed path. The obtained values for travel depth and geodesic depth are pretty similar except for the insula, where travel depth assigns lower values [122].

1.2.2.5. Gyrification Index

A frequently used metric to have a notion of the degree of cortical folding in a brain is the Gyrification Index (GI), estimated through a ratio between the area of the pial surface and the area of the outer hull of the cortex. Initially studied in *post mortem* slices of the brain [123], this metric has been widely employed in the analysis of neurodevelopment [104, 105, 124] or psychiatric disorders [45, 51, 125, 126].

Gyrification Index (GI), in its early conception, was a global measure, providing a unique value of the degree of folding for each hemisphere. The method relied on delineating the cortical perimeter using 2D slices and comparing it against the perimeter of the estimated hull enclosing the slice [123]. Limitations of this method include the possible bias by the slice orientation or the impossibility of delineating buried sulci in some cases [126]. The popular algorithm proposed by Schaer *et al.* [126] extends the concept of Local Gyrification Index (LGI), addressing the problem in a 3D space using cortical surfaces and providing local values of gyrification for every point in the cortex. In this case, two triangular meshes are used, one with the representation of the pial surface and a second with the outer hull that encloses the pial. For each point of the hull, a sphere is placed, estimating the ratio between the pial and hull area in this neighborhood. These values are subsequently mapped to the corresponding points in the pial surface, thus generating the vertex-wise LGI map. The resulting map highly depends on the radius selected for the sphere where the local index is measured. Very small values of the radius can lead to insufficient area coverage. In contrast, very high values can make the points in a region affected by a distant one, as can happen near the Sylvian fissure. Another concern of this metric is that the projection of the sphere to the pial surface leads to a different surface area covered for each region, which can also affect the results [126].

Intuitively, the GI is related to the sulcal depth and width. Decrements in gyrification degree are frequently associated with fold opening, i.e., an increase in the width [45]. It is also reasonable to think that more deep sulci will translate into increased LGI. As well, decrements in SA possibly are associated with the flattening of the folds [45].

1.2.2.6. Sulcal Width

Sulcal Width (SW), understood as the distance, filled with CSF, separating both banks of a sulcus, has been traditionally linked to the study of dementia, especially Alzheimer's disease, reporting its utility as a marker for the detection of early-onset manifestations of the pathology [127–131]. Neurodevelopmental disorders such as schizophrenia or bipolar disorders can also be linked to an increase in the SW [45, 132], being useful for the classification of schizophrenia patients [133]. It has also been used as a marker for the flattening of the cortex in adolescence [104], or pregnancy [105].

As it has been mentioned in Section 1.2.2.2, CT reports changes in the cortical gray matter; this metric alone cannot characterize if those changes occur in the interface be-

tween GM and WM or the one between GM and CSF (see Figure 1.10). This information, obtained through the width, can come in handy in interpreting the results.

Another advantage of the SW is that, while thickness depends on the GM/WM interface, width is estimated from an outer part of the cortex to another, depending on the GM/CSF interface. As it has been stated, the contrast between GM and WM decreases due to a reduction in the difference in proton density between the tissues. However, the contrast between GM and CSF is relatively stable through the life-span as the proton density of CSF is higher [110]. This makes SW less susceptible to partial volume errors and more metric in terms of age dependency.

Nevertheless, the estimation of this metric has been poorly explored. To date, the methods available are bounded to average values in ROIs. The four main methods existing in the literature are covered in the following paragraphs.

Fold Opening

The first method that addressed the estimation of sulcal width was presented by Mangin *et al.* [134]. This algorithm makes a geometrical approximation to the sulcal width, here named Fold Opening (FO). The basic idea underlying this method is that the sulcus can be approximated as a triangular prism, where two faces are the sulcal banks, and the remaining would be the surface covering the sulcus. This way, knowing the volume of the triangular prism, its length, and high, they can approximate the fold opening, i.e., the width of the mentioned sulcal cover. For this, the method relies on generating a mesh parallel to the sulcal banks that traverses the sulcus from the bottom (fundus) to the sulcal cover, perpendicular to this.

This medial mesh is created using the BrainVISA pipeline [79, 134], which uses a volumetric segmentation containing the CSF voxels of the brain. This segmentation is eroded and processed to generate a voxel skeleton that occupies the center of the fold. Then, a surface reconstruction of the voxel skeleton is performed, creating a thin triangular mesh. Knowing the area of this mesh ($A_{\text{MedialMesh}}$) and the volume occupied by the CSF (V_{CSF}), the width, or fold opening, can be approximated as:

$$\text{FO} = \frac{V_{\text{CSF}}}{A_{\text{MedialMesh}}} \quad (1.1)$$

The first drawback this method presents is that it assumes that the shape of the sulcus is regular and resembles a triangular prism. Given the intricate morphology of some sulci and their variable shape, this approximation seems overly simple. The second issue is that, as an approximation, the given value is not necessarily a physical magnitude, i.e., the output value gives a notion of the width but not its actual distance value. Additionally, the given metric is unique for the whole sulcal ROI, losing the local width variability inside the region.

Finally, the estimation and accurate labeling of the medial meshes using BrainVISA

[79] could become a complex and time-consuming task.

Sulcal Span

The Fold Opening model was refined by Kochunov *et al.* [110], where the starting point is the same medial mesh estimated by BrainVISA. In this case, the author proposes a direct measure for the sulcal width, named sulcal span. To achieve this, the normal vectors of the medial mesh are projected on the sulcal banks, avoiding the points near sulcal subdivisions. Then, Euclidean distances measured in both directions for the whole sulcus are averaged, discarding those that only cross the sulcal surface in one direction.

Compared to the FO, the main strength of this method is that the values presented in this case can be considered a real distance. However, the algorithm relies on estimating the medial mesh and provides an average value among all the sulcal width values obtained for the median mesh points. Similar to the previously described methodology, this can be controversial because the intra-sulcal variability is lost in the averaging process. Additionally, if the distribution of SW values for a region is not normal (as we might intuitively think, a sulcus would probably have more low-width values), using the average value instead of the median value can be misleading.

Finally, as in the previous case, this method relies on the BrainVISA pipeline for the generation of the medial mesh, which some users might find troubling.

Surface Based – calcSulc

The toolbox calcSulc [135] presents a method for estimating sulcal width that avoids the estimation of the sulcal medial mesh. This algorithm, built to work with the output data produced by FreeSurfer, takes the pial surface and the Destrieux cortical parcellation [88] as inputs. This atlas subdivides the hemispheric cortical surface into different gyri and sulci. The method identifies the boundaries where the sulcal regions meet their adjacent gyral regions. Ideally, this methodology assumes that this boundary should be located at a mid-distance between the hull and the fundus of the sulci. On this boundary, the algorithm matches each point, located in one of the sulcal banks with the closest (in Euclidean distance) boundary vertex on the opposite sulcal bank. Finally, having matched all the points with their opposing vertex, the median of the Euclidean distances is assigned as the value for the ROI.

The accuracy of this algorithm highly depends on the positioning of the atlas, being unstable if there are segmentation errors or the curvature matching to the reference atlas is not accurate. Another drawback is that it only samples the width in the boundary between sulcal and gyral regions, not accounting for the width variations in the rest of the sulcal basin. It is worth mentioning that a recent study has found difficulties in obtaining values for smaller sulci using this method [136].

Similar to previously described methods, calcSulc provides a unique value for a whole sulcal ROI, not accounting for the intra-sulcal variability.

Voxel Based – EDT-LM

On their side, Mateos *et al.* [137] present a voxel-based method that uses Local Maxima (LM) detection on a Euclidean Distance Transform (EDT) of the pial surface. The algorithm generates a Cartesian grid to create a voxel representation of the FreeSurfer's pial surface. In this grid, the EDT [138] is computed to estimate the closest distance from each voxel outside the cortical volume to the pial boundary. The voxels located in the center of the sulcal space are the ones with the highest values, as those are the most distant points from any sulcal bank. These local maximum voxels are detected using the proposed Local Maxima labeling algorithm [137]. Briefly, this algorithm analyzes spherical neighborhoods around every voxel outside of the pial volume. For every opposing pair of voxels in the neighborhood, the algorithm defines a path, where it analyzes the progression of EDT intensity values. If this progression follows a symmetric up-down pattern, with a maximum in the middle in at least seven of the opposing pair of voxels, the point is labeled as a local maximum. After performing these steps for every voxel, the detected LM are assigned twice the value of EDT in the point, as EDT measures the distance from the center to the sulcal wall.

The accuracy of width values obtained using this approach fully relies on the discretization of the pial cortical surface. Artifacts and voxel size of the generated volume can be limiting factors. In the paper, the reported metrics are averaged values for different sulcal regions of the Destrieux parcellation [88] and, although it is stated that sulcal width maps can be generated, there is no analysis on the matter. The reported Pearson's r correlation values between the method and the Sulcal Span [110] are over 0.5 only for the Central Sulcus, showing a limited correlation.

Finally, unlike the previous methods mentioned, the EDT-LM has no available implementation nor public code, making it difficult to test or apply in a study.

1.2.2.7. Cortical Lines Extraction

Metrics such as CV or CT are known to be affected by different factors as substance abuse [139, 140], age [141], or disease progress [142]. Conversely, the gyrification pattern is a more static factor, presenting a promising biomarker independent of said processes [51]. Moreover, it is known that the CT is higher in gyral crests than in sulcal fundi due to the deformation of the cortex during folding [143]. This translates into a different weighting of supra- and infragranular layers among those regions (see Figure 1.13). For instance, in the prefrontal cortex, the supragranular layers (cortical layers I-III) represent the 70% of the CT in the sulcal fundi, while the same layers only amount for the 49% in gyral crowns [143]. It is reasonable to think that processes affecting mainly the supragranular layers, such as schizophrenia, would have a higher impact on sulcal regions than gyral ones [143].

However, labeling such lines representing the gyral crown and sulcal fundus presents

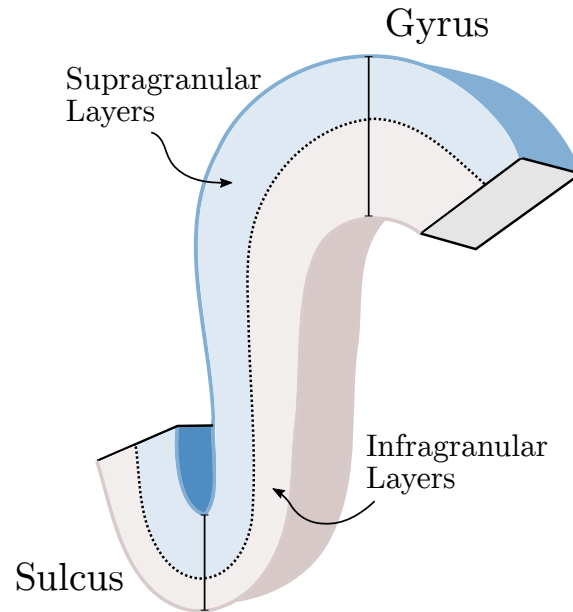


Figure 1.13: Difference of organization between supragranular (light blue) and infragranular (light red) layers in cortical regions of gyrus and sulcus. It is observable how the supragranular layers occupy most of the volume near the sulcal fundus, while the volume is more evenly distributed in the gyral crowns.

multiple challenges. The first one might be the lack of agreement in defining what is considered the top or the bottom of a fold, making it difficult to evaluate the accuracy of the segmentation. Secondly, the significant variability in the sulcal anatomy, both intra- and inter-subject, hampers the generalization of these methods.

Manual labeling of these landmarks is a laborious task, taking 2-3 days for a human operator to label a single brain [144], and presenting moderate inter-rater reliability [145]. This is why different approaches have been made to address this task.

Initial methods extracted lines on the voxel space based on criteria of maximal curvature [146, 147] or depth [148, 149]. However, due to the submillimetric vertex size and the more accurate representation of the cortical topology in the vertex, most of the subsequent methods shifted to surface approaches. Previous reviews of the existing literature have divided the existing methods into categories such as skeleton-based and line-based [150]. In the following epigraphs, I will follow this distinction categorization to present a summary of the most notable publications.

Skeleton-Based Methods

Skeleton-based methods [119, 151, 152] aim to generate the sulcal or gyral lines by removing faces from the mesh until obtaining a thin path that resembles the studied morphology. For instance, Kao *et al.* [119] compute a depth measure by estimating an outer hull and the geodesic distances from each surface point to that hull. This depth map is then used to segment the surface into sulcal regions. In these sulcal regions, the boundary faces are used to detect endpoints that remain fixed while the surface faces are decimated

without losing connectivity. Then, the longest non-branching path between the endpoints of the region is taken as the final sulcal line.

The method proposed by Yonggang Shi *et al.* [151] also starts with a segmentation between sulcal and gyral regions, in this case using a graph-cut method based on the curvature [153]. On the segmented surface regions, the method estimates the distance transform of the surfaces from their boundaries by solving the Eikonal equation (a form of the Hamilton-Jacobi equation) on the meshes. The solution to this equation can be interpreted as the minimal time a wavefront needs to propagate from one point in the surface to another; thus, starting from the points on the boundary, the points with higher magnitude would be those of the skeleton. Then, the estimation of the skeleton is achieved by a thinning algorithm that sequentially removes points from the surface, attending to the flux measures of the distance transform gradients. These skeletal points need to be pruned to generate the final set of lines.

This approach is similar to the one presented by Seong *et al.* [152]. In this case, the initial segmentation of the surface is based on a depth map that is thresholded to mark the boundary of sulcal regions. The main novelty of the method is the introduction of an anisotropic geodesic distance map that is computed using the Hamilton-Jacobi equation using a speed function based on curvature. Then, the gradient vector field of the distance map is used to estimate the central region of the sulcal basins, as in the center there is a change in the direction of the vertex coming from the boundaries. This information is used to perform the skeletonization of the surface and generate the sulcal lines.

Another that can be categorized as skeleton-based is the one included in the Mindboggle toolbox [122]. In this case, a travel depth threshold is used to segment the different sulcal basins. Then, the deepest vertices on the fold are located for located and used as seeds for the detection of endpoints. This is done by propagating geodesic paths from the seeds to the boundary, detecting at different levels the points with maximal values in the multiplication of depth by curvature on the vertex. The final endpoints are selected among those candidates that accumulate higher values of the product of those metrics. Finally, the surface is eroded, removing first the points with lower depth values given that their removal does not change the connectivity or topology of the surface.

In these examples, the quality of the mesh segmentation can induce problems in the computation of the flux or gradients of the distance transform, greatly affecting the resulting lines. Additionally, these methods present limited control over the anastomotic sulci during the pruning step. These anastomotic sulci are defined as small accessory branches usually under 5 mm [154]. These sulci present little interest as those labels are not really covering the fundus of the sulci, but small crests on the sulcal banks.

Line-based Methods

We can define line-based methods as those that seek to represent the sulcal fundi as lines on the surface. These lines are often estimated as the shortest path between two points on

the surface. The cost function used to define this shortest path varies between methods. For example, Shattuck *et al.* [155] propose a semi-automated method where the user selects two endpoints, and the algorithm delineates the corresponding gyral crown or sulcal line attending to the local convexity of the surface. The convexity is estimated by averaging the cosines of the surface normal at each vertex and the surface normals at the 1-ring neighbors. This way, local convex zones would present positive values, while local concave vertices present negative values.

However, this method requires manual input from the user having to define the endpoints of each region. This is a very time-consuming task, so Le Troter *et al.* [150] extended the idea to generate the sulcal lines without user intervention. For this, they introduce the concept of Geodesic Path Density Map (GPDM). The method takes the sulcal basin labeling from BrainVISA [79]. On each basin, they compute the shortest distance between each pair of points of the boundary, generating a density map where the value of every vertex is the number of paths that crosses it. This map is normalized so that the values are contained between 0 and 1. Finally, an adaptive threshold is applied to the density map, thus generating a line representing the fundus of the sulcus. It is worth mentioning that, unlike Shattuck *et al.* [155], in this case, the shortest path is weighted using the geodesic depth.

The main advantage of this method is that it completely avoids the endpoint extraction step, which is always challenging. However, the main drawback of this method is that it does not delineate branches in the sulci. It is also a very conservative approach, often underestimating the sulcal length.

Another example in this category would be the method proposed in Lyu *et al.* [156]. The method is divided into two principal processes. The first one consists of detecting which points of the surface correspond to sulcal regions, thus avoiding the initial segmentation of the cortex. For this, the algorithm first applies a threshold to the maximum principal curvature. Then, the resulting points are filtered out by slicing the surface using a plane perpendicular to the direction of the sulcus, creating a 2D contour where the maximum curvatures are detected with a line simplification method [157, 158]. The second part of the method consists of processing these filtered points to detect their endpoints and the optimal paths connecting them. This algorithm employs the Eikonal equation to define the geodesic distances between the points detected in the first step, while the endpoints are selected as those in the extremes of the said set of points.

In this case, the algorithm tends to label every minimal crest as a sulcal fundus, overestimating the sulcal length and introducing in the definition multiple points located in sulcal banks.

As reflected, there are different approaches to generating sulcal and gyral lines; however, the usage of these methods is not always straightforward. Many of them do not have an accessible implementation or code available. In other cases, they are not directly compatible with FreeSurfer, which is probably the most famous cortical surface creation

method. Additionally, most of these methods tend to over- or underestimate the sulcal length, including anastomotic sulci or being too restrictive. This final point is challenging, as there is no formal definition of what is a sulcal line or a gyral crown. The absence of a ground truth makes it difficult to assess the methods or decide which is correct, making this a subject of what is the interest of the researcher or the objective of the study in particular.

2. MOTIVATION AND OBJECTIVES

2.1. Motivation

The study of the human brain’s cortical morphology has been critical for an increased understanding of the pathological processes driving psychiatric disorders such as schizophrenia, bipolar disorders, autism, or major depression [45, 46, 49, 51, 54, 143]. Furthermore, charting the normal developmental changes in cortical morphology during adolescence or aging can be of great importance for detecting deviances that may be precursors for pathology [104, 105, 110, 117, 124].

It is of great interest to analyze these changes at a microscopic level to comprehend what is occurring in the cortical layer organization, neuron arrangement, or glial changes, to mention some of the possible biological processes involved. However, with the currently available tools, this microscopic level is only achievable in *post-mortem* studies.

Through MRI, we can observe and assess the brain at a macro- or mesoscale, complementing the information obtained from *post-mortem* studies in larger *in-vivo* datasets. Structural T1w magnetic resonance images are probably the most popular acquisition in brain MRI investigations, as they are relatively fast to acquire and provide good contrast between brain tissues. Even in studies focused on analyzing functional MRI or Diffusion-Weighted Imaging, anatomical images are generally obtained for tasks like segmentation or registration between subjects. The wide availability of T1w images and the above-mentioned ability to differentiate brain tissues make this modality a perfect fit for analyzing macroscopic brain properties.

As it has been stated in the Introduction, several metrics can be extracted from structural magnetic resonance images to measure the anatomy and infer the microscopic processes happening in the brain. One of the most widely used is cortical thickness, defined as the distance from the GM/WM interface to the GM/CSF interface. Precisely this dependence of the GM/WM interface can be a limitation for this technique, as it is known that the contrast between gray and white matter declines with age, making this measure age-dependent [110]. This drawback can also be associated with cortical volume, as it relies on the same GM/WM contrast.

Another important metric is the gyrification index. This is an ingenious morphometric feature that has great potential for assessing brain maturation as well as aiding in prognosis, patient stratification, and diagnosis in different pathologies [46, 51]. However, its interpretability is severely limited as it is a composite measure made up of sulcal depth, width, and length.

Sulcal width overcomes those handicaps. First, it depends only on the GM/CSF contrast which is more stable with age [110]. Second, it presents a more physical measure

than the gyrification index. However, the existing methods fail to adequately characterize sulcal width as the available algorithms only estimate averaged values for different ROIs, ignoring the possible intra-sulcal variability and, in some cases failing in small sulci [136].

The analysis of sulcal and gyral lines can also be of interest as there is a direct relation between neurodevelopment and gyral organization [30, 46, 159]. In this sense, these lines have shown potential as macroscopic landmarks for functional and cytoarchitectonic areas [57]. However, among the different line extraction methods, few capture gyral regions. Additionally, many of these methods are outdated or lack public code and implementation, making them difficult to use. Furthermore, among those with publicly available executables, there is a trend to over- or underestimate the sulcal length, labeling many sulcal banks as sulcal fundi or way too few points, thus making the output less representative of those regions.

Bearing these gaps in mind, this dissertation presents two novel methods for characterizing the brain's cortical morphology. The first one in Chapter 3 introduces and validates a sulcal and gyral line extraction method that makes an effort to avoid the delineation of anastomotic sulci [160]. The second method, in Chapter 4 contains a vertex-wise estimation of sulcal width, along with its validation. The development of these new cortical feature extraction methods also allows for improved evaluation of treatment results and clinical trial outcomes, better exchange, and comparison of information among treatment centers, and it can serve as a foundation for further research.

These two methods are conceived to be publicly available, easily used by all researchers, and ready to work with the outputs of the prevalent FreeSurfer toolbox.

2.2. Hypothesis and Objectives

The main hypothesis of the present work is that accurate cortical lines and sulcal width can provide the neuroimaging community with new high-resolution biomarkers to complement existing and widely-used metrics such as cortical thickness, gyrification index, or sulcal depth.

This thesis is divided into three main objectives:

- The first objective of this thesis, covered in Chapter 3, is to develop and validate a gyral and sulcal lines extraction method that tackles the limitations of existing algorithms. Thus, we aim to develop a line extraction tool that can avoid anastomotic sulci while maintaining the main morphology of the folds. The developed method will be compared and validated against existing algorithms to assess its reliability.
- Covered in Chapter 4, the second objective aims to fill the gap in the existing sulcal width algorithms by creating a new methodology to estimate vertex-wise maps of the cortical sulcal width. The designed algorithm is validated through the compari-

son with a simulated sulcus and in a test-retest database, assessing its performance with the one provided by two widely-used ROI-aggregated methods.

- The third objective of this dissertation presented in Chapter 5 is to apply and assess the developed tools in real clinical scenarios. The new morphometric features will be computed for a subset of structural images obtained from a freely available dataset. Several cortical features will be computed for the regions defined by gyral and sulcal lines, and vertex-wise sulcal width maps will also be estimated. The objective includes the assessment of these cortical features as well as the evaluation of their relationship with age.

3. AUTOMATED BRAIN LINES EXTRACTION BASED ON LAPLACIAN SURFACE COLLAPSE

This Chapter includes the journal publication correspondent to:

A. Fernández-Pena, D. Martín de Blas, F. J. Navas-Sánchez, L. Marcos-Vidal, P. M. Gordaliza, J. Santonja, J. Janssen, S. Carmona, M. Desco, and Y. Alemán-Gómez, “ABLE: Automated Brain Lines Extraction Based on Laplacian Surface Collapse,” *Neuroinformatics*, Aug. 2022. doi: [10.1007/s12021-022-09601-7](https://doi.org/10.1007/s12021-022-09601-7). [Online]. Available: <https://link.springer.com/10.1007/s12021-022-09601-7>

4. ESTIMATION OF VERTEX-WISE SULCAL WIDTH MAPS ON CORTICAL SURFACES

This Chapter includes the journal publication correspondent to:

A. Fernández-Pena, F. J. Navas-Sánchez, D. Martín de Blas, L. Marcos-Vidal, P. M. Gordaliza, I. Martinez-Tejada, J. Janssen, S. Carmona, M. Desco, and Y. Alemán-Gomez, “Estimation of Vertex-wise Sulcal Width Maps on Cortical Surfaces,” *bioRxiv*, Nov. 2022. doi: [10.1101/2022.11.09.515775](https://doi.org/10.1101/2022.11.09.515775). [Online]. Available: <https://www.biorxiv.org/content/10.1101/2022.11.09.515775v1>. (Submitted to NeuroImage)

Abstract

Sulcal width, defined as the physical distance between opposing sulcal banks, has shown promise as a biomarker. We present the first method to obtain a vertex-wise representation of this metric directly on the brain’s cortical surface. The algorithm samples the surface at different depths and estimates the distances between the opposing sulcal banks. The method is validated against a simulated sulcus and compared to other sulcal width tools based on regions of interest, showing solid correlations between the proposed algorithm and two widely-used reference methods. A vertex-wise assessment of the sulcal width is carried out by evaluating the correlation between sulcal width and age in a sample of an aging population, revealing clusters in the central, cingulate, and temporal sulcus regions associating wider sulci for older participants. The results confirm that the algorithm is reliable for obtaining sulcal width maps, allowing for vertex-wise analyses, and providing aggregated measures similar to the existing methods. The present algorithm is publicly available via <https://github.com/HGGM-LIM/SWiM>.

4.1. Introduction

The sulcal morphology of the human brain cortex can be quantified using magnetic resonance imaging (MRI). Sulcal width, defined as the physical distance between opposing sulcal banks, has shown promise as a biomarker for brain changes in disease, maturation, aging, or pregnancy [45, 104, 105, 133, 154, 186–189].

Most current methods for assessing sulcal width are limited to the Region Of Interest (ROI) level. The first automatic 3D ROI-based approach for sulcal width calculation was developed by Mangin *et al.* [190] and implemented in the BrainVISA image processing suite [79]. This method does not directly measure the physical distance between the sulcal banks. The method relies on the generation of a fold-specific medial mesh that follows the sulcal fundus and rises from the fundus to the intersection with a convex brain hull. The

average sulcal width for a given fold is then approximated by the quotient of the volume of the CSF buried inside the hull-covered fold with the surface area of the medial mesh [134].

Another approach is presented by Kochunov *et al.* [191] which also relies on the extraction of sulcal medial surfaces obtained from BrainVISA. The algorithm traces two opposite vectors along the normal direction up to their intersections with the sulcal bank for each point on the sulcal medial mesh. These vectors intersect on both sides of the sulcal basin, and the Euclidean distance between both intersection points is considered the sulcal width for a given medial surface point. All sulcal width values are averaged to obtain one mean sulcal width measure for each fold. While this method is a more direct measure of the distance between sulcal banks than the one presented in Mangin *et al.* [190], it has the same limitation as the previous algorithm: it only provides an average width value for a given fold (ROI).

Similarly, Madan [135] proposes a method to obtain a sulcal width measure based on the standard outputs obtained by FreeSurfer [77, 192] while avoiding the calculus of a medial surface of the folds. Here, opposing vertices in the boundaries between sulcal and gyral regions in the Destrieux cortical parcellation [88] are detected. The final metric is the median of the Euclidean distances between these opposite vertices, providing a single value for each ROI. This method depends on the gyri/sulci definition proposed by the Destrieux atlas. The sulcal width measures are only obtained in the gyri/sulci boundary, relying on the accuracy of the mapping of the sulcal labels to the individual cortical anatomy.

A voxel-based sulcal width estimation approach is presented in Mateos *et al.* [137]. The algorithm uses a voxel representation of the pial surface and estimates voxels located in the center of the sulcal space using the Euclidean Distance Transform (EDT) [193] and a Local Maxima detection algorithm. The sulcal width is given by double the distance to those estimated voxels. This method is limited by the possible discretization artifacts and the resolution selected for this discretization. Also, in their provided analyses, the method does not supply a value for each voxel in the pial boundary, but rather an aggregated metric for each region, remaining unclear how the values can be projected to the cortical surface. Additionally, the lack of an accessible implementation of the method hampers its usage.

Complementing prior methods, a vertex-wise assessment of sulcal width would enable quantification of the effects of width and its relationship with other morphological and non-morphological data at high spatial resolution. Furthermore, vertex-wise estimates of sulcal width would also allow for the mapping of width along the sulcal banks' depth to the sulcal fundus. Normalization of such profile maps may provide new clues about, e.g., at which sulcal depth sulcal widening is more pronounced and whether diseases are associated with changes in profile maps [194].

In the present work, we present a novel and robust method that provides a vertex-wise sulcal width map estimation based on the estimation of isolines at different depth levels.

Then, the points in each isoline are paired with the corresponding on the opposite sulcal wall. The distances between these points are used to estimate the vertex-wise sulcal width map. The proposed approach tackles the main issues from prior methods: 1) contrary to prior methods [190, 191], it does not rely on a medial surface of the sulci to obtain the sulcal width map; 2) the method produces full vertex-wise maps for the sulcal width instead of sulcal averages [135, 190, 191]; 3) the estimation computes the sulcal width by sampling the surface at different depth levels; 4) the method works entirely over the pial mesh triangulation, avoiding possible artifacts derived from the voxelization of the cortical surface [137], and 5) the method is entirely compatible with standard FreeSurfer output.

The performance of the developed algorithm is assessed in two different ways: First, using a synthetic (computed generated) sulcus surface as a ground truth. Second, comparing the reproducibility and distribution of averaged sulcal width values obtained using MRI data from the Human Connectome Project (HCP) [178] between the proposed algorithm and two well-known, publicly available methods: BrainVISA [190] and Kochunov *et al.* [191]. Finally, a relationship between aging and the increase of average ROI-based sulcal width has been described [8, 110, 188, 195]. However, it is not clear whether the age association is constant across sulci or whether there are focal regions that show a stronger association. We, therefore, present a vertex-wise analysis of the correlation between sulcal width and age in a subset of the Open Access Series of Imaging Studies (OASIS) [196].

The method is freely available in (<https://github.com/HGGM-LIM/SWiM>).

4.2. Methods

4.2.1. Cortical Surface Extraction and Sulcal Depth Computation

The algorithm begins with the surface extraction process from T1w anatomical images to generate a triangular mesh that wraps the boundary between grey and CSF tissues, i.e., the pial surface. The obtained mesh comprises vertices connected by edges where a set of three closed edges defines a face. In this work, this process is performed by the FreeSurfer pipeline [197, 198]. However, this methodology can be applied to triangular meshes generated using any other image processing software such as BrainVISA [79] or BrainSuite [78].

Once the cortical mesh is obtained, the first step is to estimate a vertex-wise depth map of the pial surface. In this case, we are using travel depth, understood as the shortest distance from any vertex to the convex hull without intersecting the surface [121]. The travel depth is computed using Mindboggle⁶ [122]. Travel depth is selected over geodesic depth because the latter tends to overestimate the metric, especially in areas such as the

⁶<https://github.com/nipy/mindboggle>

insula [122].

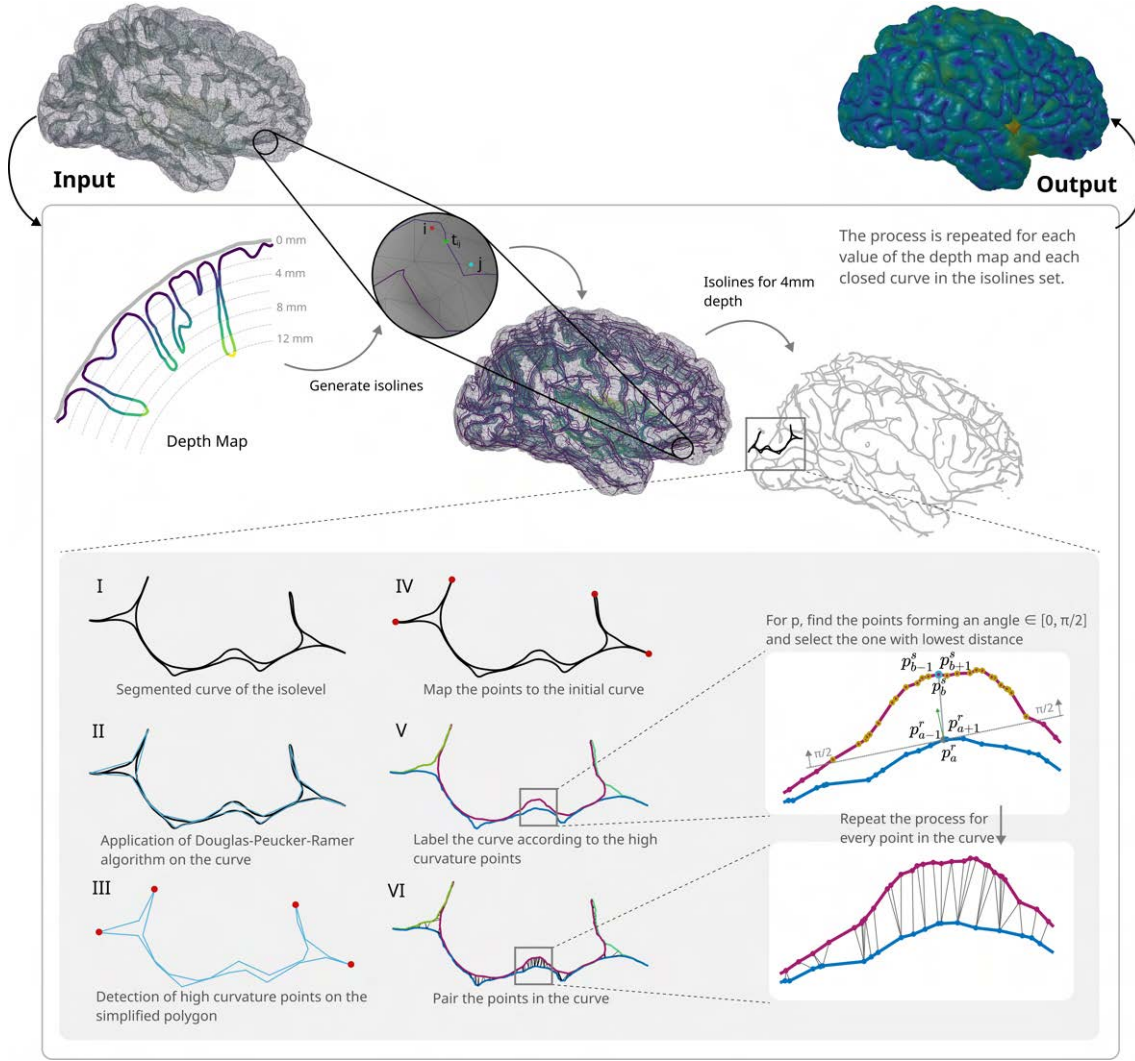


Figure 4.1: Graphic representation of the method steps. The algorithm takes the pial surface as input, generates the depth map, and for each depth level, the resulting isolines are processed as represented in the gray box. Finally, the output is a vertex-wise sulcal width map generated by aggregating all the width measures for each vertex.

4.2.2. Depth-based Isolines Construction and Labeling

The designed algorithm samples the local characteristics of the generated pial surface at different depth levels. For this, a set of isolines is created using the mentioned surface and its corresponding depth map⁷.

These isolines are a collection of closed curves over the individual surface, computed for a discrete set of equispaced depth levels starting from a minimum initial depth (Figure 4.1). The distance between depth levels should be chosen to obtain a set of isoline points denser than the surface vertices, guaranteeing that every edge on the surface is thor-

⁷<https://github.com/alecjacobson/gptoolbox>

oughly covered but without increasing the computational costs unreasonably (see SA.7 of the Supplementary Material). A reasonable value for this parameter is 1/5 of the average edge length of the surface (approximately 1 mm for the pial surfaces obtained from FreeSurfer). Therefore, for this work, we create a depth profile of sulcal depth values for every 0.20 mm. We also set the initial depth value to generate the isolines to 1.5 mm to avoid crests of the gyral regions where the definition of sulcal width is unclear.

For each depth level, we obtain the points where the isoline crosses the surface edges (see the zoomed input map in Figure 4.1) by computing the following ratio for each surface edge:

$$t_{i,j} = \frac{K - d_i}{d_j - d_i}, \quad (4.1)$$

where K is the depth value for the isoline, i and j are any pair of vertices connected by the edge, and d_i and d_j are the corresponding depth values. The resulting $t_{i,j}$ is the parameter where the depth value K falls over the line defined by the edge with vertices i and j . Only values of $t_{i,j} \in [0, 1]$ represent valid intersections between the edges and the isoline; hence, the edges yielding values out of that interval are discarded. Finally, the positions in which the isoline intersects the edges are computed as $p_{i,j} = v_i + t_{i,j}(v_j - v_i)$, where v_i denotes the position of the i vertex.

Then, each closed curve in the isoline is segmented attending to the sulcal banks where it lies. To do this, we need to identify the points where the change of sulcal wall occurs, which would be those points with a high curvature value. As the curves are continuous and contain a high number of points (Figure 4.1-I), the angles between consecutive points tend to be very plain, making it challenging to identify sharp angles. This problem is tackled using a line simplification algorithm to transform the curve into a polygon [157, 158] (Figure 4.1-II). This algorithm decimates a curve by selecting a minimum number of points from a given shape based on the maximum distance between the original curve and the simplified polygon. Supposing the new polygon is formed by the points $\{r_1, r_2, \dots, r_{n-1}, r_n\}$, the cosines of the angles between the consecutive segments in the resulting simplified polygon are estimated using the dot product between those corresponding vectors $\vec{w}_i = r_{i-1} - r_i$ and $\vec{w}'_i = r_{i+1} - r_i$.

The polygon points forming an angle lower than $3/5\pi$ with their neighbors are considered the points that mark the sulcal bank change, as wider angles are considered an effect of the normal sulcal sinuosity (Figure 4.1-III). This parameter was selected in a heuristic manner after a visual inspection of different subjects. Then, as there is correspondence between the simplified polygon and the original curve, these high curvature points are marked on the initial curve (Figure 4.1-IV). As these high curvature points divide the curves according to their sulcal banks, the algorithm assigns a different label to each curve section enclosed between two markers (Figure 4.1-V). Those labels are used in the next step to match points in different labels and estimate the sulcal width.

The label segmentation process is repeated for each closed curve of each depth-level isoline.

4.2.3. Sulcal Width Computation

The isoline I is composed of a set of N points, p_n^s , organized in S labels, where $s \in \{1, \dots, S\}$ denotes the label to which the point belongs, and $n \in \{1, \dots, N\}$ represents the index of the point in the isoline.

We pair each isoline point, p_n^s , with its corresponding in the opposite sulcal bank, q_n . For this, we first define the set of candidate points, $Q(p_n^s)$ as:

$$Q(p_n^s) = \{ p_m^r \in I \mid s \neq r, \overline{p_n^s p_m^r} \subset V_{\text{out}} \}, \quad (4.2)$$

where $\overline{p_n^s p_m^r}$ denotes the line segment, connecting the points p_n^s and p_m^r , and V_{out} the volume outside the pial surface. To obtain the set of candidates, $Q(p_n^s)$, first, we restrict the candidate points to those on a different label where the angle between the normal of the surface at p_n^s and the vector $\overrightarrow{p_n^s p_m^r}$ is in the range of $[0, \pi/2]$ (see yellow points in Figure 4.1-V close-up). This ensures that the segment $\overline{p_n^s p_m^r}$ goes outwards the surface, as otherwise it would measure gyral span. Then, the intersections between the segment $\overline{p_n^s p_m^r}$ and the pial surface are calculated [199]. The connections where $\|\overrightarrow{p_n^s p_m^r}\|$ is greater than the distance from p_n^s to the first surface intersection in the direction of p_m^r are discarded, as the segment is intersecting and crossing the pial mesh. From these candidate points, we select the corresponding point, q_n , on the opposite sulcal bank as the one with minimum Euclidean distance, i.e.,

$$q_n = \arg \min_{p_m^r \in Q(p_n^s)} \|\overrightarrow{p_n^s p_m^r}\|. \quad (4.3)$$

Repeating this process for every point in the isolines generates a list of point pairs where the Euclidean distance among each pair of points is computed and imputed to the vertices in the pial surface to obtain the sulcal width map. As each point in the isolines lies in a mesh edge, we assign the distance $\|\overrightarrow{p_n^s p_m^r}\|$ to each of the vertices forming that mesh edge. Most of the vertices in the surface have contributions from multiple isolines, so the final width value for each vertex takes the median value of all the contributed width measures. The isolines are generated using a depth step small enough to have multiple isoline values contributing to each vertex; hence, most vertices in the width map should be covered. For those that remain unlabeled (primarily those in the upper gyral regions), the values are interpolated by iteratively averaging the values of their neighbors.

Finally, we apply a linear smoothing step to the width map to refine the possible discontinuities that can appear in some regions. This smoothing averages the value of each vertex with those in its neighbors to ensure spatial coherence.

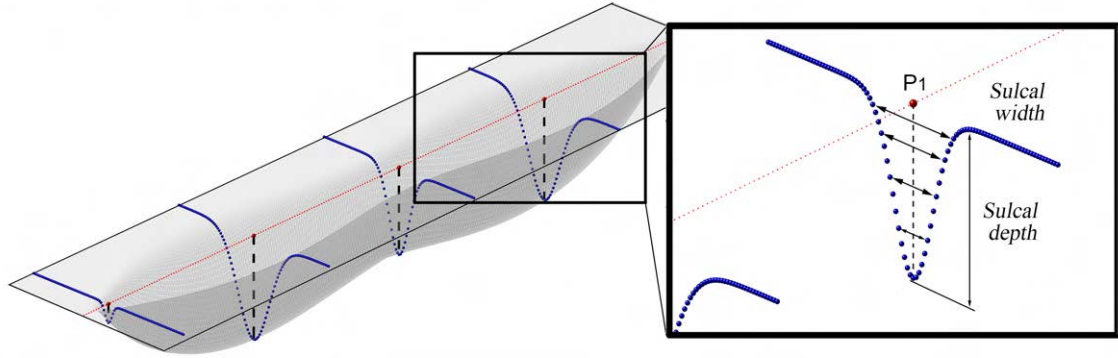
4.2.4. Validation

4.2.4.1. Validation Using Simulated Data

A triangular mesh mimicking a cortical sulcus is created to assess the performance of the proposed method. Parameters such as sulcal length, width, or depth profile are used to reproduce the morphology of a cortical sulcus, serving as a control item for the quality and reliability of the vertex-wise maps.

This synthetic sulcus has a total length of 25 cm with a spatial resolution of 10 points/cm along the longitudinal axis. For each point of the longitudinal axis, a Gaussian distribution is generated and placed orthogonally to this axis with its mean spatially located over the point (see Figure 4.2A). The width and depth of the simulated surface along the longitudinal axis are adjusted by altering the parameters of these Gaussian distributions. First, the standard deviation (σ) is varied to modify the width across its longitudinal axis. This variation is generated by a cosine function between 0 and 2π . Finally, depth fluctuation is set by multiplying the Gaussian distribution by a different amplitude factor at each longitudinal point. Both width and depth variations throughout σ and the amplitude parameters create a narrow and shallow sulcus in the sharp ends that rapidly gain width and depth and then lightly decreases again in the central region. Figure 4.2B depicts the resulting shape of the simulated sulcus.

A Gaussian distributions along the longitudinal axis



B Simulated vertex-wise sulcal width map (mm)

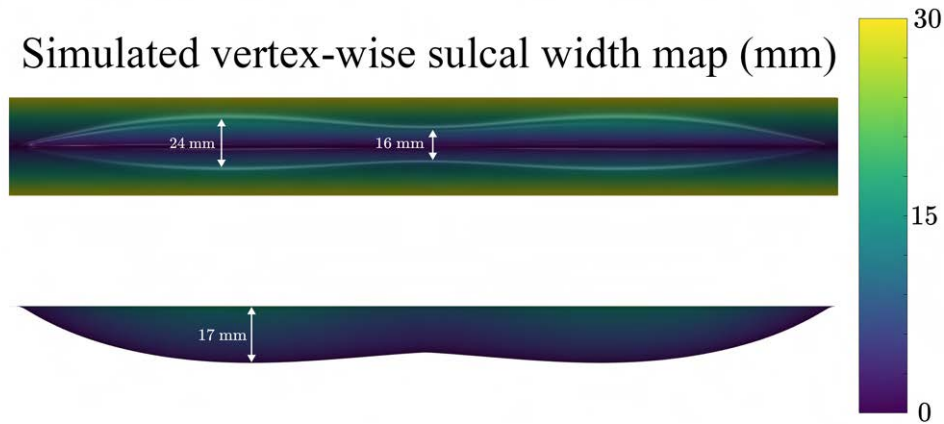


Figure 4.2: **A:** Schematic view of the generation of the simulated sulcus. **B:** Top and front perspective views of the simulated sulcus. The color bar and color map show the simulated width values in millimeters. Annotations show the main dimensions of the sulcus.

As the Gaussian distributions are symmetric, pairs of points belonging to the same Gaussian distribution, located at the same depth but in opposite sulcal banks, are paired, and the Euclidean distance between them is taken as their reference (ground truth) sulcal width value (see Figure 4.2A). Finally, the mesh is generated by creating triangular faces linking each point to its corresponding top and left neighbors.

The resulting mesh is fed into the width estimation algorithm to create the vertex-wise width map. This map is compared to the reference sulcal width map. Only vertices with depth over 0.1 mm are used for the comparisons to avoid the top flat region that is not considered part of the sulcus.

4.2.4.2. Validation Using HCP Test-Retest Dataset

The proposed algorithm is also validated through comparison against two well-known sulcal width (or fold opening) estimation methods: BrainVISA [190] and Kochunov [191].

The data used for this validation is provided by the HCP Test-Retest dataset⁸ [178]. This dataset includes 45 healthy subjects (13 male, age range of 22–35 years old) scanned twice (4.7 ± 2 months interval, minimum = 1 month, maximum = 11 months) on a Siemens 3T Skyra scanner in Washington University or University of Minnesota. T1w sagittal images were acquired using a Magnetization-Prepared Rapid Acquisition Gradient Echo (MPRAGE) sequence with 3D inversion recovery, echo time (TE) = 2.14 ms, repetition time (TR) = 2400 ms, inversion time (IT) = 1000 ms, flip angle (FA) = 8° , field of view (FOV) = $180 \times 224 \times 224$ mm³, voxel size = $0.7 \times 0.7 \times 0.7$ mm³. The HCP consortium also provides the cortical surfaces (pial and white) and their curvature maps, obtained by a project-specific FreeSurfer pipeline [179].

The pial surfaces are imported to the BrainVISA’s Morphologist [79] pipeline, where the medial sulcal surfaces are created. The medial sulcal surfaces are automatically labeled according to the sulcal region they occupy [200] and are manually corrected to minimize the individual differences in labeling between test and retest cortical surfaces. These medial meshes are projected over the gyral banks to generate sulcal basins corresponding to each labeled sulcus. This way, we generate corrected sulcal region maps for every subject.

All analyses are performed in ten primary sulci (five for each hemisphere) that are consistently present across individuals and show less inter-individual variability than other sulci: central sulcus, calcarine, superior temporal sulcus, parieto-occipital fissure, and cingulate sulcus on both hemispheres [182].

For each of these sulci, we evaluate the performance of the proposed method for computing sulcal width values compared to the ones obtained by the other two methodologies (BrainVISA and Kochunov). These methods provide a unique sulcal width value for each sulcus. Hence, we average the width map generated by the proposed method in each vertex belonging to the same sulcal basins extracted from the Morphologist pipeline, discarding the points relative to gyral regions (i.e., vertices with depth below 1.5 mm).

4.2.4.3. Application to the OASIS-3 Dataset

To demonstrate the potential usages of the tool, the algorithm is applied to a cohort of adults drawn from the OASIS-3 dataset⁹ [196]. The selected subset contains individual T1w MR images of 362 subjects, ages 42 to 95 years old. These images were acquired at the same Siemens TrioTim 3T scanner using a 3D GR/IR scanning sequence with the following parameters: echo time (TE) = 3.16 ms, repetition time (TR) = 2400 ms, inversion time (IT) = 1000 ms, flip angle (FA) = 8° , field of view (FOV) = $176 \times 256 \times 256$ mm³, voxel size = $1 \times 1 \times 1$ mm³.

This analysis aims to assess, vertex-wise, the effect of age over the sulcal width.

⁸<https://db.humanconnectome.org/>

⁹<https://www.oasis-brains.org/>

FreeSurfer (v.7.2) [197, 198] is used to extract the cortical surfaces (white and pial) and to perform all statistical analyses. The individual sulcal width maps are estimated using the FreeSurfer outputs and then registered to the *fsaverage* surface. A geodesic Gaussian smoothing with a full width at half maximum (FWHM) of 5 mm is performed previous to the statistical analyses.

4.2.5. Statistical Analyses

4.2.5.1. Simulated Data

Pearson’s correlation coefficient and a Bland-Altman plot are used to assess the estimated sulcal width map’s accuracy compared to the ground-truth values.

4.2.5.2. Test-Retest Dataset

The mean width values of each of the ten sulci were compared between different methods using paired Student’s t-test analyses.

The similarities between methods are assessed by linear regression. The width values of the proposed method are regressed against the two control algorithms, and Pearson’s correlation coefficients are calculated.

Finally, the reproducibility of each method is measured using both the Intraclass Correlation (ICC) and the Root Mean Square Error (RMSE) between the width values computed for test and retest acquisitions. ICC describes how similar are the width measures in the test and retest acquisitions compared to the total variation of the width measures across all acquisitions and all subjects, while RMSE gives a notion of the magnitude of the error between test and retest values.

For each analysis, resulting p-values are corrected for multiple comparisons (10 comparisons, 5 for each hemisphere) using False Discovery Rate (FDR) [183], considering $q \leq 0.05$ as significant. All statistical analyses are performed using Python packages Pingouin [185], and Scipy [201].

4.2.6. Subcohort of OASIS-3 Dataset

A general linear model including gender and age as a factor and continuous covariate respectively is designed, and 10,000 Montecarlo permutations are used to obtain a Cluster-Wise Probability (CWP) [202] using FreeSurfer. A p-value < 0.0001 as the cluster-forming threshold for multiple comparisons correction is selected.

4.3. Results

4.3.1. Results on the Simulated Sulcus

Figure 4.3 shows the results of the comparison between the simulated and estimated data. The correlation coefficient between vertex-wise simulated and estimated width values is 1 (Figure 4.3A). In the Bland-Altman plot (Figure 4.3B), the differences between simulation and estimation are reported on the vertical axis, while their mean is depicted on the horizontal axis. This plot shows higher discrepancies in regions with lower sulcal width which are located near the extremities and the fundus of the simulated sulcus (Figure 4.3C).

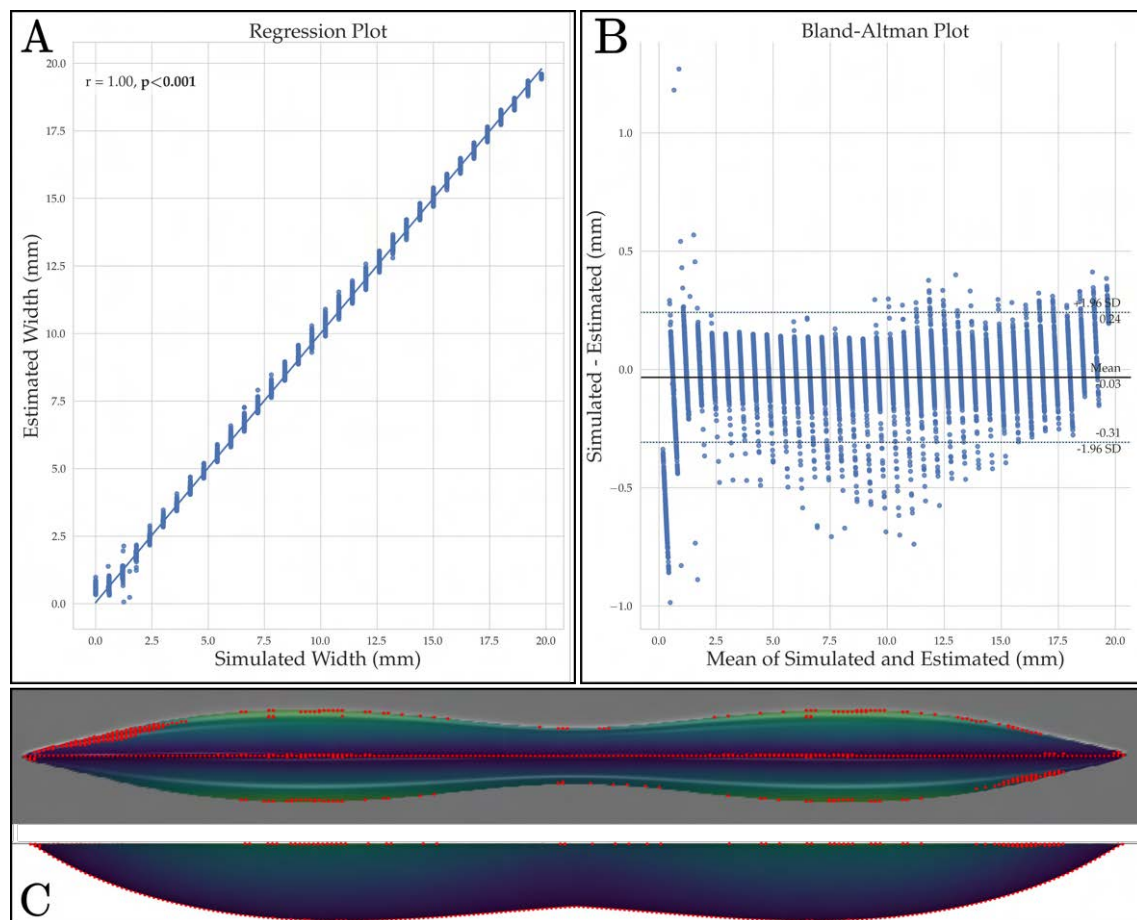


Figure 4.3: **A:** Regression plot between simulated and estimated width values of the vertices of the synthetic sulcus. **B:** Bland-Altman plot comparing simulated and estimated sulcal widths. **C:** Simulated sulcus with the points presenting width values out of the confidence interval highlighted in red. The gray region indicates depth values lower than 0.1 mm.

4.3.2. Results on the HCP Test-Retest Dataset

For each of the ten sulci of interest, we can observe the mean width distribution in Figure 4.4 for the three inspected methods. Table 4.1 reports the pairwise comparison results

of the distribution differences between the proposed method and the two control methods.

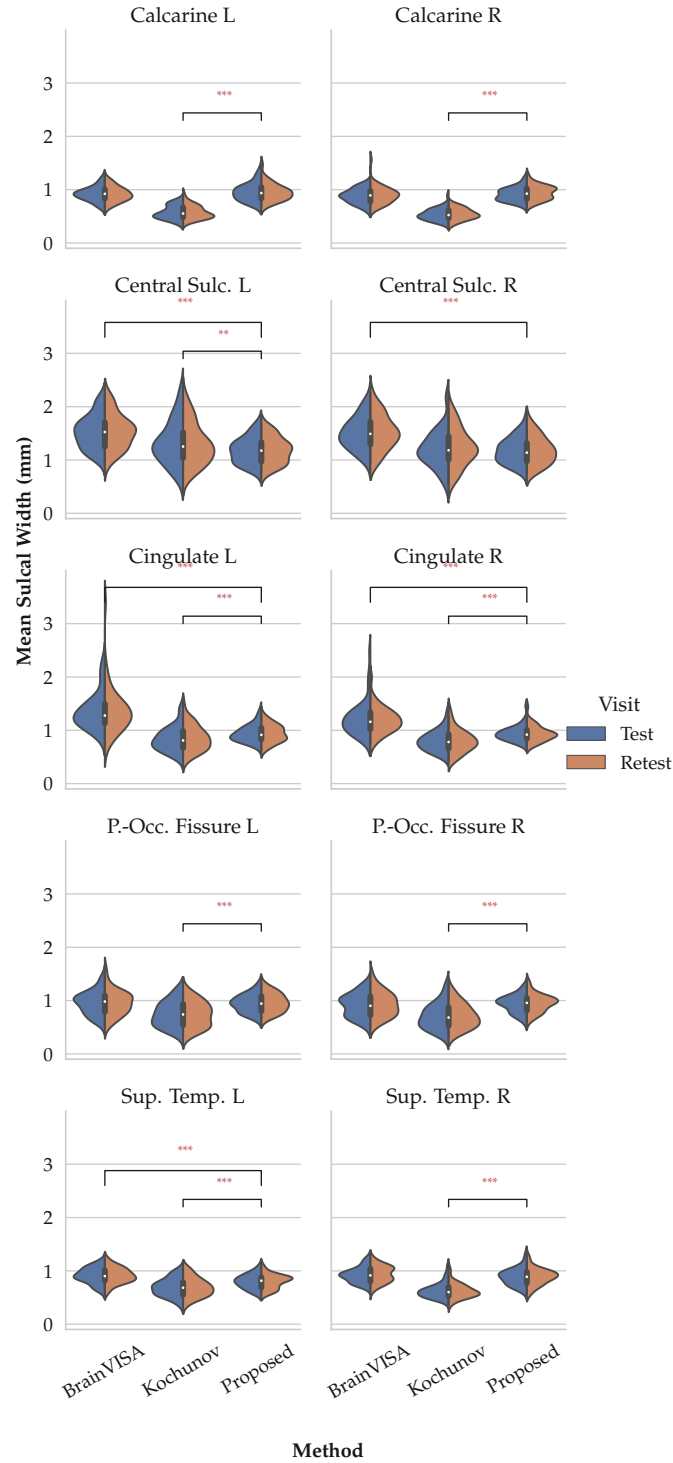


Figure 4.4: Violin plot representing the mean sulcal width for the ten selected sulci. For each method, the blue part of the plot represents the values obtained for the test acquisition, while the orange part represents the mean sulcal width values for the retest acquisition. Symbols “*”, “**”, and “***”, stand for significant differences between methods with FDR-corrected p-values lower than 0.05, 0.01, and 0.001 respectively.

Compared to the proposed method, BrainVISA displays higher values of width in the central sulcus (left: $p < 0.001$, $t = -22.23$; right: $p < 0.001$, $t = -21.90$) cingulate sulcus

(left: $p < 0.001$, $t = -10.65$; right: $p < 0.001$, $t = -10.46$), and left superior temporal sulcus ($p < 0.001$, $t = -7.35$), while the rest of comparisons are not significant.

The proposed method shows width values higher than the ones reported by Kochunov for the calcarine (left: $p < 0.001$, $t = 19.85$; right: $p < 0.001$, $t = 26.64$), cingulate (left: $p < 0.001$, $t = 4.83$; right: $p < 0.001$, $t = 9.52$), parieto-occipital fissure (left: $p < 0.001$, $t = 8.71$; right: $p < 0.001$, $t = 10.56$), and superior temporal sulcus (left: $p < 0.001$, $t = 5.58$; right: $p < 0.001$, $t = 12.80$). Kochunov reports higher values than the proposed method for the left central sulcus ($p = 0.006$, $t = -3.47$).

The regressions between the proposed method and the other two methodologies (BrainVISA and Kochunov), along with Pearson's correlation coefficient, are shown in Figure 4.5. On one hand, the correlation coefficient between BrainVISA and the proposed method is minimum in the left cingulate sulcus ($r = 0.58$, $p < 0.001$), while for left and right central sulcus, the correlation is $r = 0.96$ ($p < 0.001$). For the left and right parieto-occipital fissures r values are 0.80 and 0.84, respectively (both $p < 0.01$). On the other hand, the correlation coefficients between the proposed method and Kochunov are higher for the cingulate sulcus (left: $r = 0.80$, $p < 0.001$, right: $r = 0.88$, $p < 0.001$). Lowest correlation values between the proposed method and Kochunov are found in the superior temporal sulcus left: $r = 0.61$, $p < 0.001$; right: $r = 0.52$, $p < 0.001$.

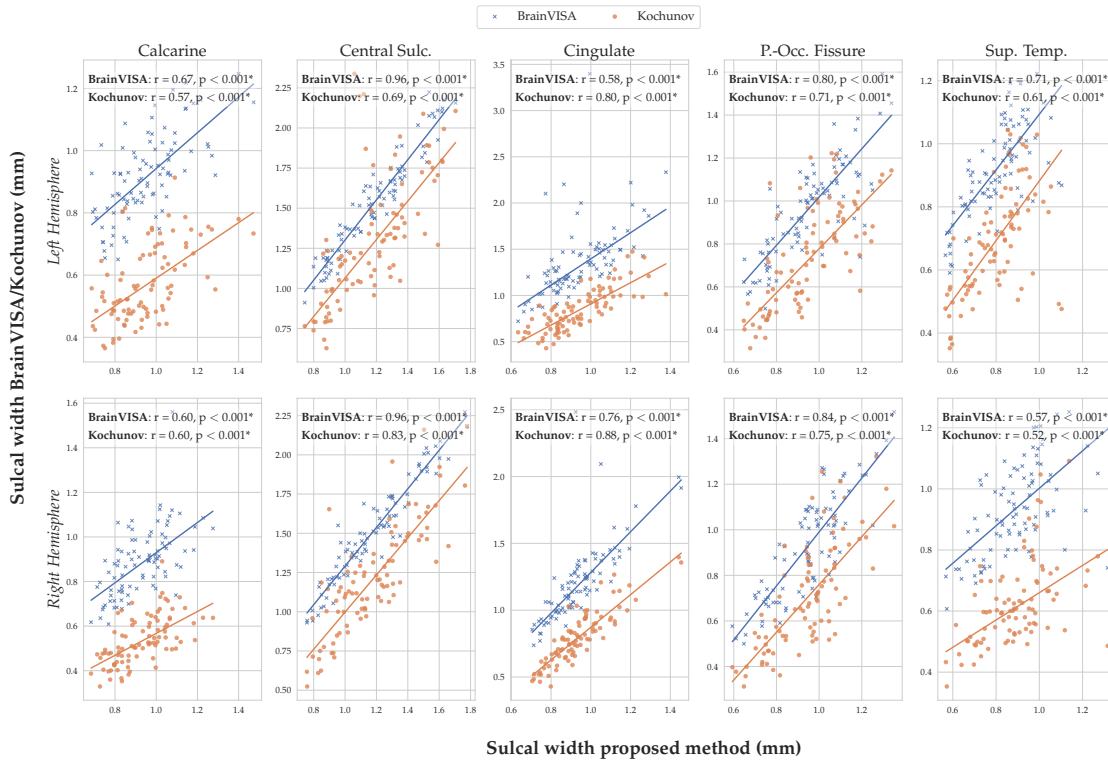


Figure 4.5: Width regression per sulcus. All p-values reported are corrected using FDR. Symbol “*” stands for significant values ($p < 0.05$) after correction. P.-Occ. Fissure stands for Parieto-Occipital Fissure. Sup. Temp. stands for Superior Temporal sulcus.

The ICC results (Table 4.2) indicate that the proposed method has a minimum ICC

Sulcal Width Pairwise t-tests

Sulcus Name	Proposed	BrainVISA	Kochunov	Proposed - BrainVISA		Proposed - Kochunov	
		Mean (std)		t (p-corrected)	Cohen's D (CI[95%])	t (p-corrected)	Cohen's D (CI[95%])
Left Hemisphere							
Calcarine	0.95 (0.16)	0.92 (0.13)	0.57 (0.12)	2.04 (0.201)	0.24 (-0.07, 0.54)	19.85 (<0.001)	2.72 (2.07, 3.38)
Central Sulcus	1.18 (0.24)	1.53 (0.32)	1.31 (0.39)	-22.23 (<0.001)	-1.25 (-1.65, -0.85)	-3.47 (0.006)	-0.43 (-0.75, -0.12)
Cingulate	0.94 (0.16)	1.36 (0.39)	0.84 (0.23)	-10.65 (<0.001)	-1.61 (-2.07, -1.16)	4.83 (<0.001)	0.50 (0.19, 0.82)
Parieto-Occipital Fissure	0.95 (0.17)	0.95 (0.22)	0.74 (0.24)	-0.16 (1.000)	-0.02 (-0.32, 0.28)	8.71 (<0.001)	1.03 (0.65, 1.40)
Superior Temporal	0.80 (0.13)	0.91 (0.14)	0.69 (0.17)	-7.35 (<0.001)	-0.83 (-1.18, -0.48)	5.58 (<0.001)	0.74 (0.40, 1.08)
Right Hemisphere							
Calcarine	0.93 (0.13)	0.89 (0.15)	0.54 (0.11)	2.40 (0.098)	0.31 (0.00, 0.61)	26.64 (<0.001)	3.45 (2.65, 4.24)
Central Sulcus	1.18 (0.25)	1.51 (0.31)	1.22 (0.35)	-21.90 (<0.001)	-1.19 (-1.58, -0.80)	-1.62 (0.451)	-0.15 (-0.45, 0.16)
Cingulate	0.94 (0.14)	1.20 (0.29)	0.80 (0.20)	-10.46 (<0.001)	-1.26 (-1.67, -0.86)	9.52 (<0.001)	0.81 (0.46, 1.15)
Parieto-Occipital Fissure	0.94 (0.16)	0.92 (0.22)	0.71 (0.23)	1.37 (0.676)	0.12 (-0.18, 0.42)	10.56 (<0.001)	1.18 (0.79, 1.57)
Superior Temporal	0.89 (0.15)	0.93 (0.15)	0.62 (0.14)	-2.09 (0.190)	-0.29 (-0.60, 0.01)	12.80 (<0.001)	1.89 (1.39, 2.39)

Table 4.1: Sulcal width comparisons. Mean values and standard deviations are reported in millimeters. In bold, the values that remained significant differences ($p < 0.05$) after FDR correction in the pairwise t-test.

value for the right calcarine sulcus (ICC = 0.821) and maximum ICC value for the left central sulcus (ICC = 0.961). ICC for BrainVISA ranges between 0.484 (left cingulate sulcus) and 0.971 (left central sulcus). For Kochunov, the ICC values vary from 0.796 in the right calcarine sulcus to 0.946 in the left superior temporal sulcus. The results for every combined sulcus show that the proposed method's ICC value is 0.930, while BrainVISA has an ICC of 0.869 and Kochunov scores 0.934.

Intraclass Correlation (ICC)

Sulcus Name	Proposed		BrainVISA		Kochunov	
	ICC (CI[95%])	<i>p</i> -corrected	ICC (CI[95%])	<i>p</i> -corrected	ICC (CI[95%])	<i>p</i> -corrected
<i>Left Hemisphere</i>						
Calcarine	0.862 (0.760, 0.920)	<0.001	0.894 (0.820, 0.940)	<0.001	0.854 (0.750, 0.920)	<0.001
Central Sulcus	0.961 (0.930, 0.980)	<0.001	0.971 (0.950, 0.980)	<0.001	0.813 (0.690, 0.890)	<0.001
Cingulate	0.886 (0.800, 0.940)	<0.001	0.484 (0.220, 0.680)	0.002	0.904 (0.830, 0.950)	<0.001
Parieto-Occipital Fissure	0.896 (0.820, 0.940)	<0.001	0.940 (0.890, 0.970)	<0.001	0.944 (0.900, 0.970)	<0.001
Superior Temporal	0.883 (0.800, 0.930)	<0.001	0.877 (0.790, 0.930)	<0.001	0.946 (0.900, 0.970)	<0.001
<i>Right Hemisphere</i>						
Calcarine	0.821 (0.660, 0.900)	<0.001	0.678 (0.480, 0.810)	<0.001	0.796 (0.660, 0.880)	<0.001
Central Sulcus	0.954 (0.920, 0.970)	<0.001	0.965 (0.940, 0.980)	<0.001	0.845 (0.740, 0.910)	<0.001
Cingulate	0.918 (0.850, 0.950)	<0.001	0.710 (0.530, 0.830)	<0.001	0.905 (0.830, 0.950)	<0.001
Parieto-Occipital Fissure	0.890 (0.810, 0.940)	<0.001	0.911 (0.840, 0.950)	<0.001	0.942 (0.900, 0.970)	<0.001
Superior Temporal	0.851 (0.740, 0.920)	<0.001	0.837 (0.720, 0.910)	<0.001	0.861 (0.760, 0.920)	<0.001
All	0.930 (0.880, 0.960)	<0.001	0.896 (0.820, 0.940)	<0.001	0.934 (0.880, 0.960)	<0.001

Table 4.2: Intraclass correlation coefficient (ICC) estimating the resemblance between two different measures of a sulcus for the same subject. Bold values in *p*-corrected column indicate significant results ($p < 0.05$) after correcting for multiple comparisons using FDR.

Finally, RMSE results (Table 4.3) indicate the proposed method scores lower errors for central sulcus (left: 0.005 mm; right: 0.006 mm), cingulate (left: 0.006 mm; right: 0.003 mm), and parieto-occipital fissure (left: 0.006 mm; right: 0.006 mm). BrainVISA shows lower errors for the left calcarine sulcus (0.004 mm), while Kochunov reports lower errors for the right calcarine sulcus (0.005 mm) and superior temporal sulcus (left: 0.003 mm, right: 0.005 mm). The combined value for every sulcus is lower for the proposed method with 0.006 mm.

4.3.3. Relationship Between Vertex-wise Sulcal Width and Age

Vertex-wise analyses revealed a significant positive correlation between age and sulcal width. Clusters surviving the multiple comparisons correction (CFT < 0.0001, CWP < 0.0001) are those located in the central, superior temporal, and temporoparietal sulci, as well as the lateral fissure and some parts of the cingulate sulcus and the parieto-occipital fissure (see Figure 4.6).

Root Mean Square Errors (mm)			
Sulcus Name	Proposed	BrainVISA	Kochunov
<i>Left Hemisphere</i>			
Calcarine	0.007	0.004	0.004
Central Sulcus	0.005	0.006	0.058
Cingulate	0.006	0.156	0.010
Parieto-Occipital Fissure	0.006	0.006	0.006
Superior Temporal	0.004	0.005	0.003
<i>Right Hemisphere</i>			
Calcarine	0.006	0.014	0.005
Central Sulcus	0.006	0.007	0.037
Cingulate	0.003	0.048	0.008
Parieto-Occipital Fissure	0.006	0.009	0.006
Superior Temporal	0.007	0.007	0.005
All	0.006	0.026	0.014

Table 4.3: Root mean square errors (mm) between test and retest measures for each method and sulcus. Bold values indicate the minimum value for each row.

Vertex-wise Correlation Between Sulcal Width and Age

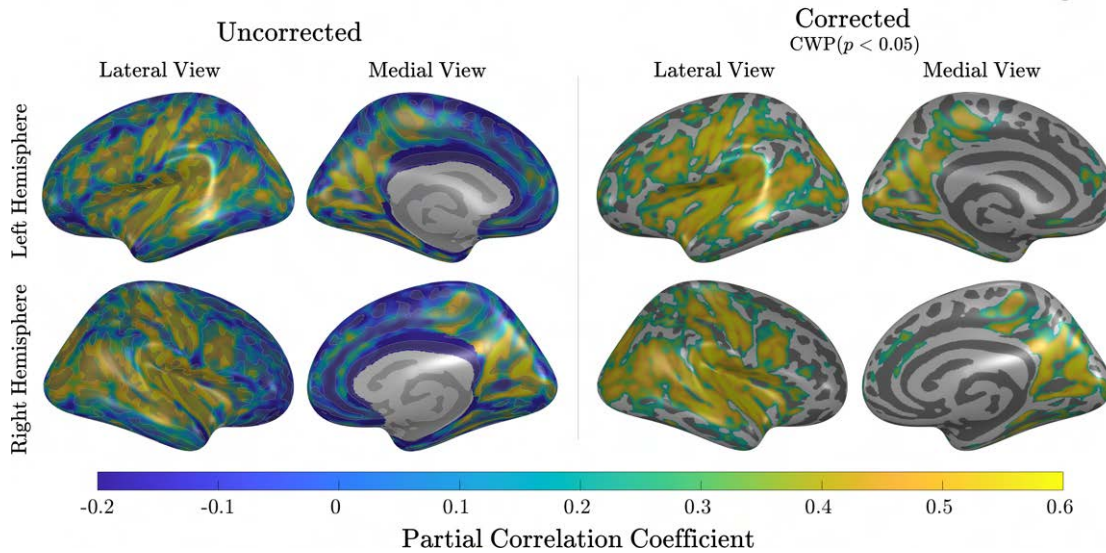


Figure 4.6: Vertex-wise partial correlation coefficients between age and width. The figures on the right side present results with a Cluster Forming Threshold (CFT) of 0.0001 and a Cluster-Wise Probability (CWP) threshold of $p < 0.05$.

4.4. Discussion

The presented results demonstrate that the proposed method provides a reliable vertex-wise measure of the physical distance between cortical sulcal banks. The algorithm, validated using simulated data and real data and compared against two widely-used sulcal width estimation algorithms, provides the community with an innovative method for creating cortical vertex-wise sulcal width maps.

First, validation using simulated data shows the accuracy of the results in a controlled

environment. Secondly, using the HCP test-retest dataset and averaging vertex-wise values of sulcal width across ROIs, we enabled comparison with the ROI-based methods of BrainVISA [190] and Kochunov [191]. Results from our algorithm displayed a high correlation with the values obtained using BrainVISA and Kochunov. In addition, the results indicate a robust reproducibility of our method, very similar to the one scored by the two mentioned toolboxes. Finally, the results from our group-wise vertex-wise analysis on OASIS-3 data extend prior findings from ROI studies by demonstrating individual, within-sulci variability in the positive association between age and sulcal width.

Validating sulcal width estimation methods is challenging as there is no available gold standard or ground truth. Therefore, by creating a simulated sulcus with known width for each vertex, we intended to approximate a ground truth to assess our method. Although the simulated sulcus does not reach the complexity of the most intricate sulci, it can mimic the characteristics of the regular sections of the sulcal basins, providing a well-described setting to evaluate the algorithm's performance. Across the grand majority of vertices, our method produces width values that show a high correlation with the ground truth values. This provides the certainty that the algorithm properly measures widths for a simple representation of a sulcus.

We further validated our method using test-retest real data. Given the absence of real-life ground truth vertex-wise sulcal width data, we compared results from our method against results from existent ROI-based sulcal width toolboxes as BrainVISA [190], and Kochunov [191]. Notably, the width values from these three approaches are similar for most sulci. Cross-method comparisons show, for example, that correlation coefficients between our method and Kochunov are between 0.52 and 0.88 for every sulcus, which is considerably higher than previous cross-method comparisons not involving our algorithm as the EDT-based approach in Mateos *et al.* [137], that reports $r > 0.5$ only for the central sulcus. This analysis demonstrates that the proposed method behaves similarly to the reference methods at the ROI level. Furthermore, ICC values show excellent reproducibility for all the algorithms analyzed, except the left cingulate for BrainVISA. Precisely, the lower ICC value for BrainVISA in the left cingulate sulcus could explain the lower correlation between our method and BrainVISA for that ROI.

Having established that our method produces, at the ROI level, highly similar results to the ones delivered by Kochunov and BrainVISA, we now must mention that these two methods, along with others such as calcSulc [135], present a fundamental issue: they are bounded to a given atlas and provide averaged or median values for a whole region. The proposed method generates a vertex-wise map that boosts the number of analyses available for this metric. For instance, one can perform analyses in native space using any atlas of interest. Of course, vertex-wise studies are also an option, allowing the user to develop advanced models, e.g., investigate the relationship between changes in cortical thickness and sulcal width.

Employing the OASIS-3 healthy aging dataset, we used our method to analyze the

vertex-wise association between age and sulcal width across individuals. The results reveal considerable variability of association strength across sulcal regions. This clearly demonstrates an advantage of our algorithm over ROI-based methods. That is, our method allows for the detection of within-sulci variability, whereas ROI-based methods only produce width averages that obscure within-sulci variability. The clusters of vertices that survived the multiple comparisons correction are located primarily in the central sulcus, superior frontal sulcus, inferior temporal sulcus, and lateral sulcus or parieto-occipital fissure. These results extend the findings of Jin *et al.* [188] and Kochunov *et al.* [110] by showing that the widening of sulci during senescence is widespread but also varies considerably within the ROIs.

4.4.1. Limitations

The developed algorithm relies on identifying the different sulcal banks that compose each isoline. This critical step relies on detecting the points of high curvature of the curve based on a threshold. This threshold, chosen after visual inspection of different sulci in the dataset, is high enough to capture the most pronounced ones without including unnecessary divisions. However, fine-tuning might be needed when applying the method to populations with different characteristics, such as Alzheimer’s disease or infants.

After segmenting the isoline curves into different sulcal banks, the next step is to identify the matching points on the opposite wall. Using the Euclidean distance to find this closest point presents one inconvenience: it tends to match points close to the division between sulcal banks with points adjacent to the division point instead of the one across the sulcus. This problem is noticeable when analyzing the results of the simulated sulcus, where errors are located in the regions near the wall division. However, this should not significantly affect the overall results since the error is limited to minimal areas near the junction between walls.

Finally, the results of vertex-wise analyses involving gyral regions must be addressed carefully, as those regions might not fit well in the sulcal width definition. These regions might be excluded from the analyses masking the gyral areas, providing only results for the sulcal regions to simplify the interpretation of the results.

4.5. Conclusions

In light of the presented results, the developed method produces a reliable direct measure of the sulcal width, providing vertex-wise maps while tackling the main problems found in the previous literature. The algorithm and its source code are publicly available in <https://github.com/HGGM-LIM/SWiM>.

Acknowledgments

This work was supported by the project exAScale ProgramIng models for extreme Data procEssing (ASPIDE), that has received funding from the European Union's Horizon 2020 research and innovation program under grant agreement No 801091. This work has received funding from "la Caixa" Foundation under the project code LCF/PR/HR19/52160001. Susanna Carmona is funded by Instituto de Salud Carlos III, co-funded by European Social Fund "Investing in your future" (Miguel Servet Type I research contract CP16/00096). The CNIC is supported by the Instituto de Salud Carlos III (ISCIII), the Ministerio de Ciencia e Innovación (MCIN) and the Pro CNIC Foundation, and is a Severo Ochoa Center of Excellence (SEV-2015-0505).

Data were provided in part by the Human Connectome Project, WU-Minn Consortium (Principal Investigators: David Van Essen and Kamil Ugurbil; 1U54MH091657) funded by the 16 NIH Institutes and Centers that support the NIH Blueprint for Neuroscience Research; and by the McDonnell Center for Systems Neuroscience at Washington University.

Data were provided in part by OASIS-3 (Principal Investigators: T. Benzinger, D. Marcus, J. Morris; NIH P50 AG00561, P30 NS09857781, P01 AG026276, P01 AG003991, R01 AG043434, UL1 TR000448, R01 EB009352. AV-45 doses were provided by Avid Radiopharmaceuticals, a wholly owned subsidiary of Eli Lilly).

5. MORPHOLOGICAL EVALUATION OF AN AGING DATASET

This chapter contains an application of the methods presented in Chapters 3 and 4 for a subsample of the OASIS-3 database [196]. The main goal is to characterize changes relative to aging using the proposed tools as a basis. For this, three analyses are presented. The first one investigates how the cortical thickness varies in gyral and sulcal regions along age, assessing the differences between the sulcal and gyral regions. The second analysis characterizes the relationship between sulcal and gyral length and age. Finally, the third study provides the vertex-wise correlation between age and thickness, age and width, age and width excluding the effect of cortical thickness, and width and thickness excluding the effect of age.

5.1. Sample Description

The sample is composed of 620 (370 females) cognitively normal adults from the OASIS-3 database with ages ranging from 42.7 to 95.2 years. The distribution of ages can be found in Figure 5.1.

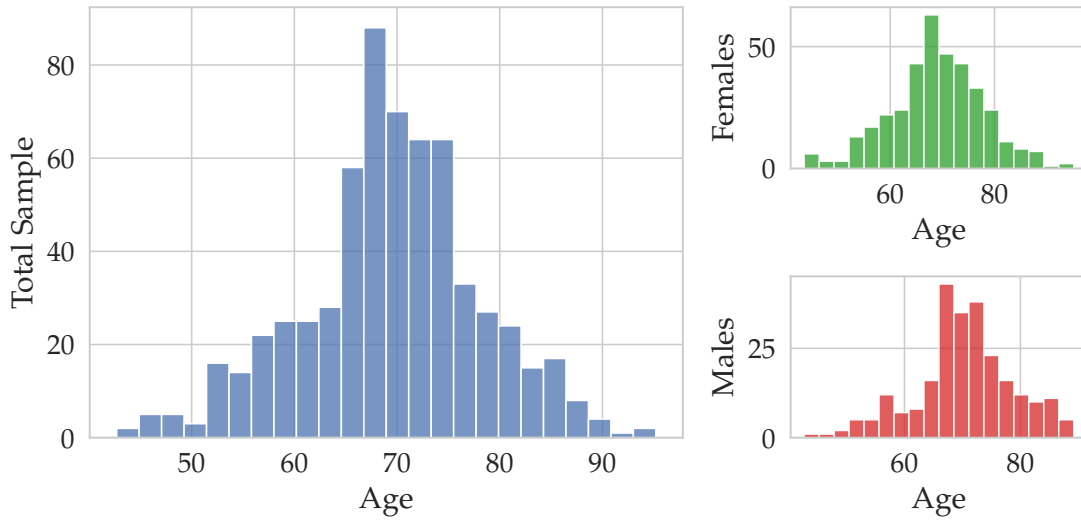


Figure 5.1: Histogram reporting the age distribution, on the left, in blue, distribution for the total sample. The plot on the upper right, in green, depicts the distribution of female participants. Below this, in red, the plot shows the age distribution of male participants.

The selected subsample includes participants acquired in three different scanners: two 3T Siemens MAGNETOM Tim Trio and a 3T Siemens Biograph mMR. The distribution of participants per scanner can be seen in Figure 5.2. Siemens Tim Trio 3T scanners use a 3D GR/IR scanning sequence with the following parameters: echo time (TE) = 3.16 ms, repetition time (TR) = 2400 ms, inversion time (IT) = 1000 ms, flip angle (FA) = 8°,

field of view (FOV) = $176 \times 256 \times 256 \text{ mm}^3$, voxel size = $1 \times 1 \times 1 \text{ mm}^3$. On its side, Siemens Biograph 3T scanner uses a 3D GR/IR scanning sequence with the following parameters: echo time (TE) = 2.95 ms, repetition time (TR) = 2300 ms, inversion time (IT) = 900 ms, flip angle (FA) = 9° , field of view (FOV) = $176 \times 240 \times 256 \text{ mm}^3$, voxel size = $1.2 \times 1.05 \times 1.05 \text{ mm}^3$.

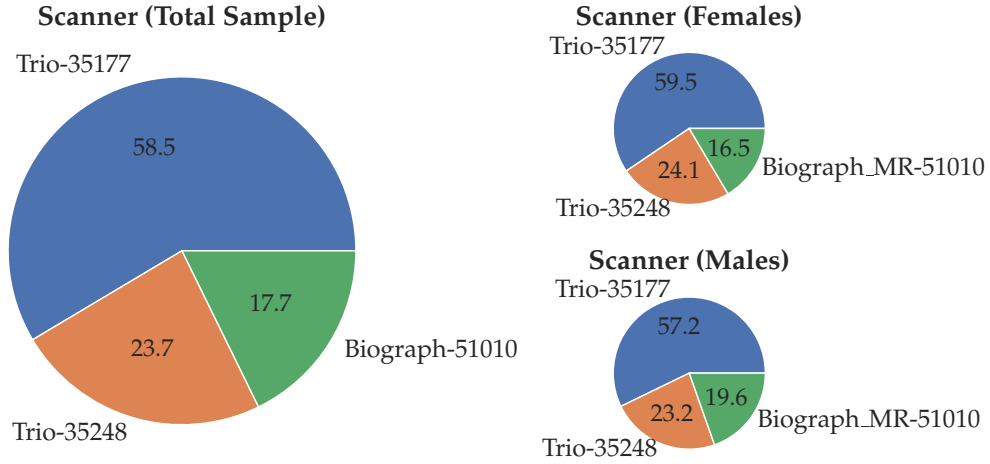


Figure 5.2: Pie charts showing the sample distribution by scanner. The chart on the left reports the distributions for the total sample. In the upper right is reported the distribution for female participants. Below this, the chart shows the scanner distribution for male participants.

All the T1w images are processed using FreeSurfer (v.7.2) [77, 198] to extract the cortical surfaces (white and pial), estimate the cortical thickness measures, the total brain volume, and obtain their Desikan parcellations [87].

The output surfaces are used for the estimation of sulcal and gyral lines using the method described in Chapter 3. The pial surface is used to estimate vertex-wise width maps following the method reported in Chapter 4.

5.2. Interaction Between Age and Cortical Thickness in Sulcal/Gyral Lines

The objective of this analysis is to quantify possible differences in CT trajectories with age among the regions defined by gyral and sulcal lines. For this, the lines, estimated using the methodology developed in Chapter 3, are grouped into different lobes according to the Desikan cortical parcellation [87] provided by FreeSurfer, grouping the correspondent labels to the frontal, parietal, temporal, and occipital lobes as can be seen in the Appendix of Klein and Tourville [144]. Then, for each lobe, an average value is calculated for the gyral and sulcal regions.

5.2.1. Statistical Analysis

The statistical analysis is performed using a linear mixed-effects model [203] for each lobe, including thickness as the dependent variable and age, location for each lobe (gyri or sulci), scanner, sex, total brain volume, and age by location interaction as independent variables. To study differential age trajectories for each location, we test the effect of age-by-location interaction in this model. The results of the interaction between location and age are corrected using False Discovery Rate (FDR) [183] along with the results of Section 5.3.

5.2.2. Results

Figure 5.3 reports the adjusted linear mixed-effects model prediction for each lobe in the gyral and sulcal regions. Table 5.1 shows the statistics of the models for the age-by-location interactions.

		t-value (95% CI)	p-value (FDR)
Hemisphere	Lobe		
Left	Frontal	4.16 (2.20, 6.12)	< 0.001
	Occipital	7.21 (5.25, 9.17)	< 0.001
	Parietal	5.97 (4.01, 7.93)	< 0.001
	Temporal	8.93 (6.97, 10.89)	< 0.001
Right	Frontal	4.12 (2.16, 6.08)	< 0.001
	Occipital	6.10 (4.14, 8.06)	< 0.001
	Parietal	3.76 (1.80, 5.72)	0.001
	Temporal	7.40 (5.44, 9.36)	< 0.001

Table 5.1: Results of the interaction between age and location (sulcus/gyrus) for cortical thickness per lobe. All reported p-values are significant (p-FDR < 0.05) correcting by FDR.

In Figure 5.3, it is apparent that the trajectories of thickness in gyral regions are more horizontal with age than those in sulcal regions, where there is a clear steady decrease in thickness as years progress. This difference between slopes is more pronounced in the temporal lobes (left: $t = 8.93$, $p\text{-FDR} < 0.001$; right: $t = 7.40$, $p\text{-FDR} < 0.001$), while the regressions for the right parietal lobe appear more parallel ($t = 3.76$, $p\text{-FDR} = 0.001$).

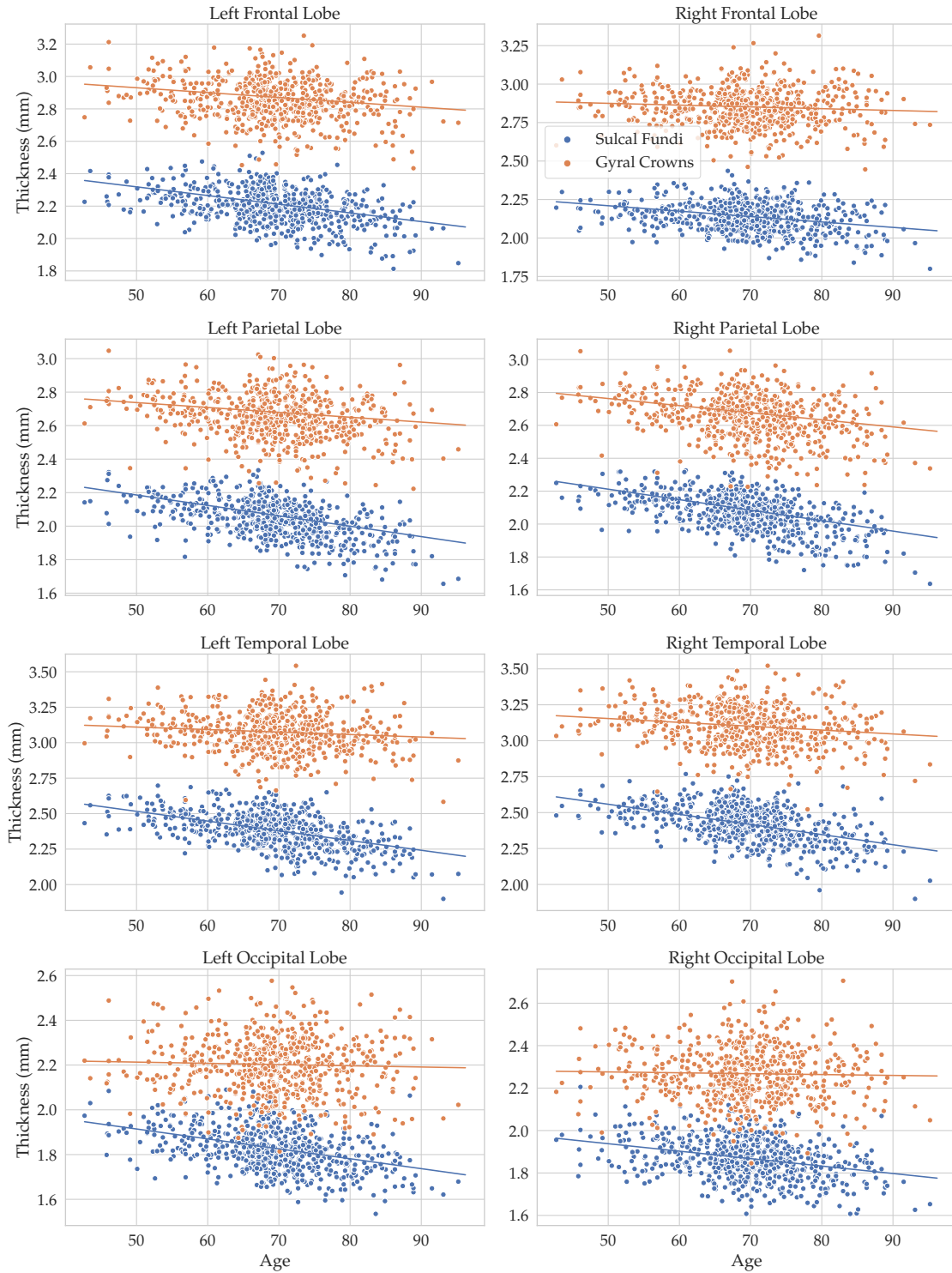


Figure 5.3: Scatter plots for the thickness in gyral (orange) and sulcal (blue) lines along with the predictions of the linear mixed-effects models.

All the p-values for the age-by-location interactions in Table 5.1 are equal or below 0.001, reinforcing the graphic information of Figure 5.3. This indicates that the slopes characterizing the relationship between cortical thickness and age are significantly different between sulcal fundi and gyral crowns regions.

5.3. Correlation Between the Length of Sulcal/Gyral Lines and Age

This analysis evaluates the change in sulcal and gyral length with age. Similar to the previous section, the cortical lines are extracted for each hemisphere and grouped into lobes by merging the corresponding labels on the Desikan atlas [87] as indicated in the Appendix of Klein and Tourville [144]. Then, for each lobe, the global length of gyral and sulcal lines is estimated.

5.3.1. Statistical Analysis

The statistical analysis for this comparison is performed using a General Linear Model. In each lobe, two models are adjusted, one for the sulcal length and another for the gyral length. Each model includes the length as the dependent variable and scanner, sex, total brain volume, and age as independent variables. Then, we test the effect of age to assess its relationship with length. Hence, we study the change in length across ages, controlled by the effect of the scanner, sex, and total brain volume. The p-values of the age regression are corrected using False Discovery Rate (FDR) [183] along with the results of Section 5.2.

5.3.2. Results

Figure 5.4 depicts the linear regressions per lobe between measured lengths and age. The plots show that sulcal and gyral lengths behave similarly throughout age, with a slight increase in those metrics. These relationships are stronger in both parietal lobes.

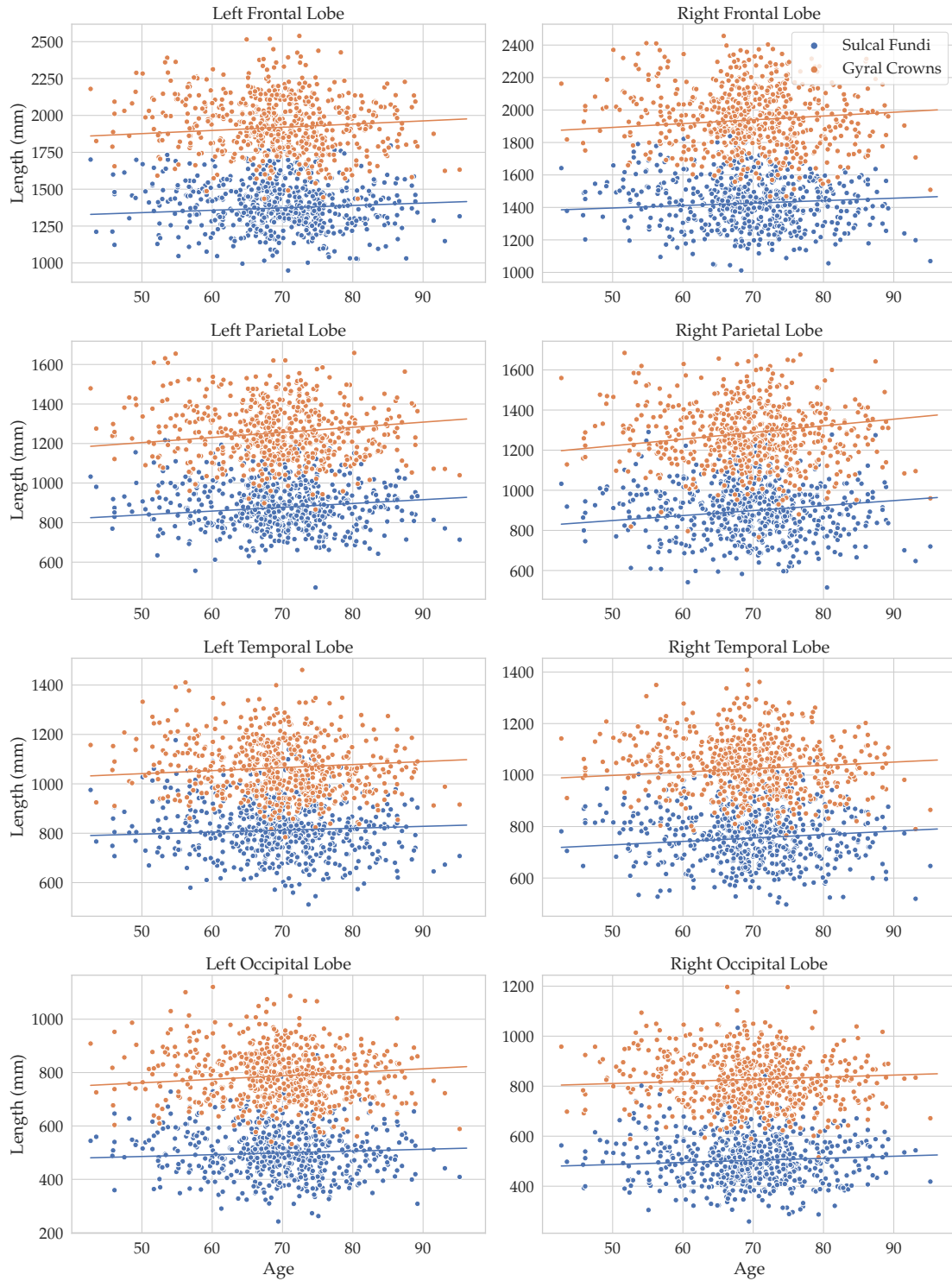


Figure 5.4: Scatter plots for the sulcal (blue) and gyral (orange) length with age along with their linear regressions.

Results in Table 5.2 confirm the findings in Figure 5.4, as the statistics show stronger correlations between age and length in parietal lobes for both sulci (left: $t = 3.94$, $p\text{-FDR} = 0.001$; right: $t = 4.81$, $p\text{-FDR} < 0.001$) and gyri (left: $t = 4.97$, $p\text{-FDR} < 0.001$; right: $t = 5.84$, $p\text{-FDR} < 0.001$). On the opposite side, the relation is weaker in the occipital

lobes, where only the regression for the gyri in the left occipital is significant ($t = 3.22$, $p\text{-FDR} = 0.008$).

Position	Hemisphere	Lobe	t-value (95% CI)	p-value (FDR)
Gyrus	Left	Frontal	3.37 (1.41, 5.34)	0.005
		Occipital	3.22 (1.26, 5.18)	0.008
		Parietal	4.97 (3.01, 6.93)	< 0.001
		Temporal	3.10 (1.14, 5.06)	0.011
	Right	Frontal	3.74 (1.78, 5.71)	0.001
		Occipital	1.86 (-0.10, 3.82)	0.274
		Parietal	5.84 (3.88, 7.80)	< 0.001
		Temporal	3.35 (1.39, 5.32)	0.005
Sulcus	Left	Frontal	2.70 (0.74, 4.66)	0.034
		Occipital	1.56 (-0.40, 3.52)	0.450
		Parietal	3.94 (1.98, 5.91)	0.001
		Temporal	1.78 (-0.18, 3.75)	0.298
	Right	Frontal	2.68 (0.72, 4.65)	0.034
		Occipital	1.78 (-0.18, 3.74)	0.298
		Parietal	4.81 (2.84, 6.77)	< 0.001
		Temporal	3.01 (1.05, 4.98)	0.014

Table 5.2: Results of the correlation between age and length in gyral and sulcal regions per lobe. In boldface, p-values significant ($p\text{-FDR} < 0.05$) corrected by FDR.

5.4. Vertex-wise Correlations Between Age, Thickness, and Width

The aim of this analysis is to demonstrate the potential of vertex-wise studies using sulcal width maps. For this, we estimate and compare the per-vertex correlations between age and thickness and age and width. These analyses allow us to observe the sensitivity of each metric to age dependency. The individual FreeSurfer's pial surfaces are used as input of the algorithm described in Chapter 4. The cortical thickness maps used in the analysis are also computed using FreeSurfer's pipeline.

5.4.1. Statistical Analysis

FreeSurfer's group analysis is employed to generate the surface-based study using cluster-wise correction for multiple comparisons [202]. On one hand, a general linear model including width as the dependent variable and sex, scanner, total brain volume, and age as independent variables is designed. We test if there is a significant relationship between

sulcal width and age. Ten thousand Montecarlo permutations are used to obtain a Cluster-Wise Probability (CWP) ($p < 0.0125$) [202] using FreeSurfer. A p -value < 0.0001 as the Cluster Forming Threshold (CFT) for multiple comparisons correction is selected. In this case, a more restrictive p -value of the usual 0.05 for the CWP was selected to correct for the multiple comparisons we performed in the vertex-wise models (three different analyses).

On the other hand, the relation between age and thickness is assessed using a model that includes CT as the dependent variable, age as the variable of interest and sex, scanner and total brain volume as factors and continuous covariates, respectively.

Finally, to investigate the relationship between width and age accounting for the effect of thickness, the same General Linear Model as the first analysis is used, taking the sulcal width as the dependent variable, age as the variable of interest, and sex, scanner, total brain volume, and thickness as factors and continuous covariates respectively. Once again, a p -value < 0.0001 as the CFT, and ten thousand Montecarlo permutations are used to obtain a Cluster-Wise Probability (CWP) ($p < 0.0125$).

5.4.2. Results

Figure 5.5A shows the results of the correlations of age with thickness and width. In this cortical plot, Pearson's r values of the 'Age * Thickness' correlation are around -0.5. The clusters surviving the correction are mainly located in the central sulcus, lateral fissure, cingulate sulcus, and around the parieto-occipital fissure. On the other hand, the 'Age * Width' correlation has bigger clusters surviving the corrections. These clusters are mainly located in the central sulcus, the temporal region, the lateral fissure, and some in the parieto-occipital fissure and the cingulate sulcus. In this second case, the correlation is positive, with peak values around 0.6.

The analysis in Figure 5.5B shows the model where thickness is added as a covariate. The results of this analysis are quite similar to the ones in Figure 5.5A for 'Age * Width' correlation, with results appearing in the same regions and comparable Pearson's r values.

5.5. Discussion

This chapter aims to demonstrate the potential applications of the tools presented in this dissertation on a set of aging cognitively normal adults. First, the comparison of cortical thickness in gyral and sulcal lines shows that, as expected, the gray matter in the former is thicker than in the latter. A more interesting finding is that the atrophy trajectory with age in sulcal regions is significantly steeper than in gyri. This finding replicates, using a very different methodology and database, the results of Lin *et al.* [204]. This difference can be due to the general flattening of the cortex, as the curvature in the white surface increases while it decreases in the pial surface [204]. The findings of this scenario are similar to

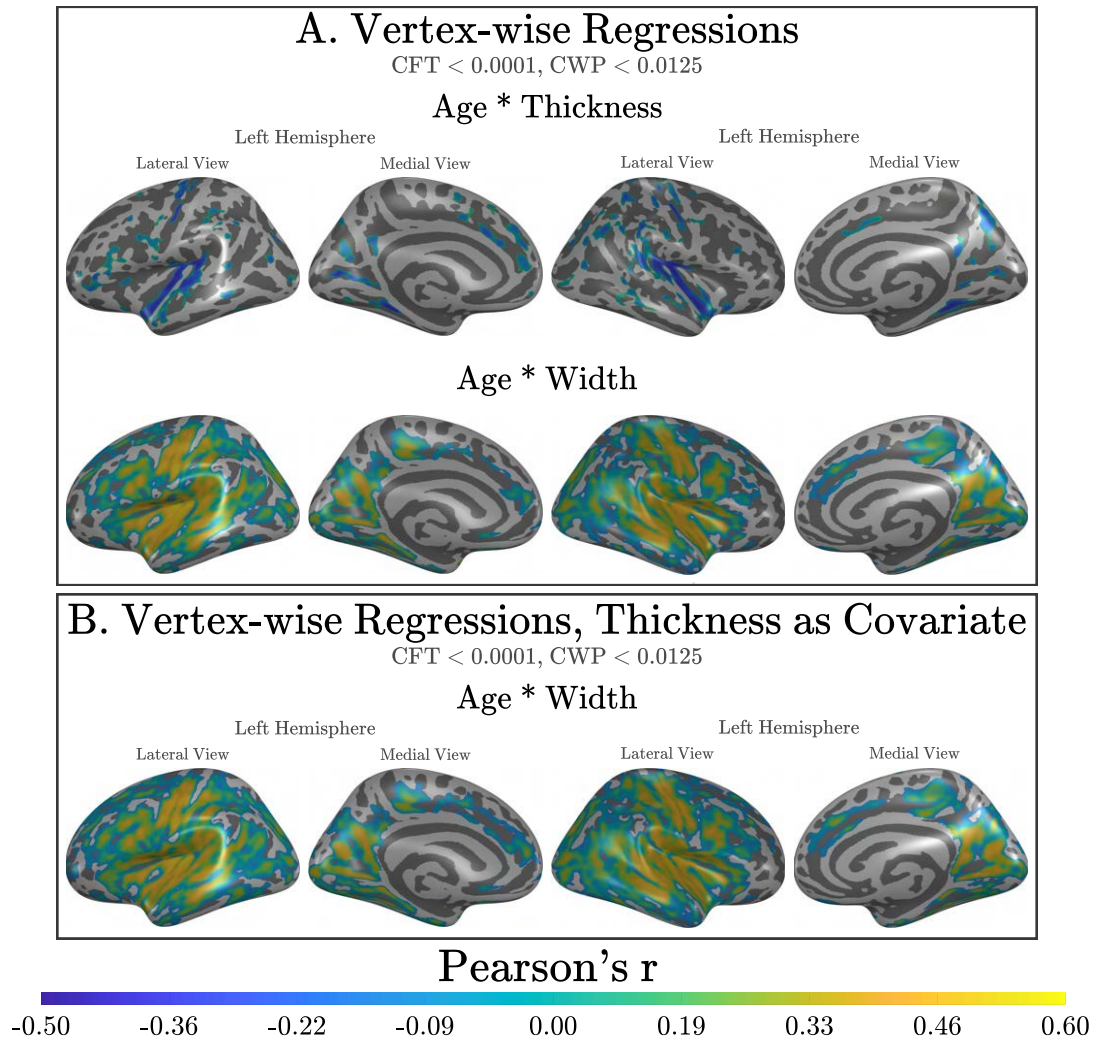


Figure 5.5: Vertex-wise maps reporting correlation results. The selected Cluster Forming Threshold (CFT) is 0.0001. Then, a threshold of $p < 0.0125$ is selected as Cluster-Wise Probability (CWP). A: regression between age and width, and age and thickness regressing by total brain volume, scanner, and sex. B: the same model as A, adding thickness as a regressor. The map shows the correlations between age and width.

those in schizophrenia, where it has been reported that thickness in sulcal fundi is thinner than in gyral crowns due to the different affection of the supragranular layers [143]. This theory indicates that, as supragranular layers represent a higher volume in sulci than in gyri, pathologies affecting those would have a greater impact on sulci. The same principle could apply to patients with Alzheimer's disease or other types of dementia, as it has been documented that supragranular layers appear compressed in those pathologies, at least for the inferior temporal and superior frontal cortex [205]. This documented compression is coherent with the analysis results, as the temporal lobe seems to be the region where the thickness in the sulci suffers a higher thinning with age compared to gyri.

The analysis of the thinning trajectories in sulcal and gyral regions could serve as a biomarker. This way, if schizophrenia or dementia patients present increased differences

between thickness in sulci and gyri, a normative model can be proposed to detect possible anomalies early.

The analysis of the sulcal and gyral length variation across ages shows a slight increase in length for older participants. This variation can be explained by the general flattening of the surface with aging, as a plainer gyrus or sulcus would present longer tails, adding to a longer length.

The results from the vertex-wise analysis of the sulcal width show a widening of sulci for older participants. This has been previously reported in ROI analyses [8, 110, 188]. In this case, the vertex-wise results show some intra-sulcal variability; for example, results in the cingulate sulcus are located mainly in the posterior region. This general widening supports the findings in the length analysis as wider sulci would translate into a flatter cortex, slightly increasing the total measured sulcal and gyral longitudes.

It is worth noting that the sulcal width is more sensitive to age than thickness. The analysis of CT changes with age shows few significant clusters for the selected thresholds. Previous studies have linked the width changes to a GM [110, 188]; however, the model adding thickness as a regressor indicates that most of the detected width changes are not due to GM thinning. It is reasonable to think that if the sulcal width enlarges while thickness remains largely stable, the changes can come from the flattening of the cortex or a decrease in the gyral WM.

The combination of the results of the vertex-wise analysis with the thickness in gyral and sulcal lines might suggest that cortical thinning is occurring, but those changes are local. A restrictive surface-based analysis such as the one performed for the thickness might not be sensitive enough to detect those changes that could be more perceptible in a localized study.

In summary, the present analyses in a real dataset illustrate the potential applications of the developed tools. These methods show high sensitivity to biological processes such as aging, increasing the available data that can be extracted from the structural MRI. In these few examples, it has been stated that the tools could help in defining normative models [206] through anomalous patterns in the gyral/sulcal lengths or thickness or even complement the existing cortical thickness surface maps to detect morphological changes that might have been overlooked in previous studies.

6. GENERAL DISCUSSION

The study of the human brain's cortical morphology has been critical for an increased understanding of the pathological processes driving psychiatric disorders such as schizophrenia, bipolar disorders, autism, or major depression [45, 46, 49, 51, 54, 143]. Furthermore, charting the normal developmental changes in cortical morphology that occur during adolescence or aging can be of great importance for detecting deviances that may be precursors for pathology [104, 105, 110, 117, 124]. However, the existing methodologies fail to adequately capture some of the brain's morphological features. The current dissertation presents and validates two novel methods for measuring certain aspects of human cortical morphology, addressing the limitations of previous methods. These new tools can help define new biomarkers, complement existing methods, and help fill gaps when inferring the processes happening at a mesoscale level using MRI macroscale data.

First, the tool for delineation of sulcal and gyral lines presented in Chapter 3 has been validated against three publicly available methods: GPDM [150], TRACE [156], and Mindboggle [122]. The results show that the proposed approach is the best trade-off between length and positioning, labeling sulcal lines that go through zones with high depth and curvature, showing high correlation with, and similar lengths as, the reference values from BrainVISA [79], and reporting good reproducibility indicators. The main strength of this method is that it manages to avoid anastomotic sulci [110, 207] in contrast to methods such as GPDM, which produces very short lines by avoiding every sulcal bifurcation, or others like TRACE that label every small crest in the brain as sulcal fundi, overestimating the total length.

Second, Chapter 4 introduces a new tool for generating high-resolution (i.e. vertex-wise) sulcal width maps. Methods to compute surface area and sulcal depth maps have been proposed but to the best of our knowledge, this thesis is the first to propose a vertex-wise sulcal width map computed directly over the cortical surfaces. This approach will allow for 1) the detection of sulcal width alterations at high resolution and 2) the assessment of whether GI subcomponents are differentially altered during neurodevelopment or along clinical subtypes.

The method is validated through a simulated sulcus resembling a simple fold's morphology. Additionally, the algorithm's reliability is assessed using a test-retest database and comparing the obtained metrics with those of two popular previous methods: Fold Opening [134], and Sulcal Span [110]. These comparisons, averaging the results of the proposed method in the regions specified by BrainVISA, show strong correlations between the proposed and the existing algorithms, with Pearson's r values over 0.96 for the central sulcus. In a previous study that performed a similar method comparison [137], the highest correlations with the Sulcal Span method also appeared in the central sulcus, but their Pearson's r values were considerably lower, around 0.6.

Our method opens up new possibilities, as the ROI analysis is now open for any user-defined region. Additionally, our algorithm allows for so-called vertex-wise studies, discerning the possible intra-sulcus deviations. Also, the existence of a vertex-wise map makes it possible to extend the analyses to, for example, non-parametric permutations [208] of sulcal width and cortical thickness, studying the joint inference of both metrics at the vertex-level.

Having assessed the reproducibility and performance of the proposed methods, Chapter 5 proved their potential in a use-case scenario. For this, the algorithms were applied to a subset of the OASIS-3 database [196] with 620 cognitively normal adults ranging from 42 to 95 years old. The main idea was to elucidate fine-grained morphological changes in the human cortex with aging. After applying our methods, we conducted three analyses: a comparison of the age-dependencies of cortical thickness in gyral and sulcal lines, an analysis of how the sulcal and gyral length changes with age, and a vertex-wise study of sulcal width and cortical thickness.

These analyses showed, as expected, a general flattening of the cortex with aging [104, 110], with interesting findings such as a differential age-dependency of thickness thinning in the sulcal and gyral regions. By demonstrating that our method is capable of detecting this difference, our results can pave the way for future in vivo studies focusing on macro- and microscopic changes that are specific to gyri or sulci, for example, the notion that supragranular layer pathology in schizophrenia is differentially expressed in sulci versus gyri [143]. In addition, our method can generate new brain-based biomarkers specific to sulci and gyri, and these can be used on large samples to establish normative models [206] to which patients can be compared. Moreover, sulcal and gyral lines can be used to investigate the diverging patterns in cortico-cortical, functional, or structural connectivity between these topological opposite regions [16, 209]. In parallel, the vertex-wise analyses show that sulcal width is very sensitive to changes during aging, independent of cortical thickness. This corroborates the concept of sulcal width as a metric that explains, in the least, the unique variance of morphology not fully captured by existing metrics. Our method allows for sulcal width vertex-wise analyses that were not possible previously, potentially changing our understanding of how changes in sulcal width shape cortical morphology.

Finally, it is worth mentioning that the developed tools are conceived to be fully automated and easily employed by any user. Unlike other published articles, our methods are publicly available in their respective repositories (<https://github.com/HGGM-LIM/ABLE>, <https://github.com/HGGM-LIM/SWiM>), open to community contributions. The publicly available FreeSurfer software suite is probably the most widely used image processing toolkit for generating cortical surfaces and traditional metrics from T1-weighted images [192]. The election of FreeSurfer is based on its huge popularity, with over 40,000 results in Google Scholar¹⁰. Our methods are designed to work with standard FreeSurfer output as well as output from other toolkits. This means that for the hundreds of existing

¹⁰https://scholar.google.com/scholar?as_q=%22FreeSurfer%22

databases already processed with FreeSurfer, using these tools does not require additional analysis, just executing those methods, potentially reaching a wider user base.

In summary, this thesis presents two new publicly available tools for estimating cortical morphometrics that have been validated and assessed against existing algorithms. The proposed methods have also been tested on a real dataset, providing new, interesting, insights into cortical morphology and showing their potential for defining innovative biomarkers.

6.1. Limitations

The principal limitation when addressing methods that measure cortical characteristics is the lack of ground truth or gold standard. From the cortical thickness to the position of sulcal fundi, there is no clear-cut dataset for validation of our results. In the case of lines delimiting the folding morphology, the problem is even more emphasized; there is no general consensus about what entails a sulcal fundus or a gyral crown. Thus, the validation of these methods must be handled carefully. In this work, the validation has been twofold, first comparing the methods against similar metrics, and then applying the tools to real datasets and assessing if the obtained results are coherent.

Another important limitation when addressing line extraction is postprocessing. In this case, the metrics for sulcal and gyral lines are provided as aggregated metrics per lobe, labeling them according to an existing well-defined parcellation. Registration-based labeling of the lines can be useful when the division comprises big regions, as in the case of lobes. However, a more fine-grained subdivision based on sulcal definitions might be desirable for hypothesis-driven studies. In those cases, registration-based labeling can induce gross errors due to the great inter-subject variability. In recent years, some Deep Learning tools have tried to generate sulcal-level labels [210, 211], but the methods are still limited, requiring a very specific format of data or labeling only a few sulci.

Finally, using vertex-wise sulcal width maps for generating group comparisons can be controversial for the gyral regions. Interpreting the significant results obtained in those parts might be delicate, as the definition of sulcal width is unclear in gyral crests. The results obtained for ‘Age * Width’ regressions in the present dissertation lie mainly in sulcal regions; however, the introduction of a gyral mask that discards undesired areas should be studied.

6.2. Future Lines

- The developed method for the cortical lines extraction might be a good candidate for the generation of normative models that measure how well a participant fits in the curve of normal development, serving for the detection and classification of anomalous patterns.

- Joint inference analyses of area, depth, and sulcal width can serve as an alternative to the local Gyrification Index, providing a more immediate interpretation of the metrics driving the results.
- The sulcal width method can be adapted to measuring gyral span. This new metric, in combination with sulcal width and cortical thickness, can completely characterize the changes in folding morphology.

7. CONCLUSIONS

- We have developed a fully automated sulcal and gyral line extraction method. The method has been assessed against existing algorithms, providing a solution that generates lines that travel through deeper and more curved regions, with length metrics similar and highly correlated with the reference values. The obtained reproducibility indicators are similar to or better than the compared methods.
- We have created a tool for the estimation of vertex-wise sulcal width maps. The method has been validated using a simulated sulcus that resembles a simple fold. In parallel, the algorithm has been assessed in terms of accuracy and reproducibility, comparing the results against two widely-used ROI-based width estimation tools. The obtained results show a high correlation between the existing methods and the designed algorithm for the studied regions.
- The developed algorithms have been applied to a real database of aging cognitively normal participants. The results of the analyses demonstrate that our methods can detect age-dependent cortical changes both in sulcal width and related to gyral and sulcal lines.
- The two developed tools are open-source and publicly available in their respective repositories. Both algorithms are conceived to be easily used with FreeSurfer's outputs.

BIBLIOGRAPHY

- [1] A. Fernández-Pena, D. Martín de Blas, F. J. Navas-Sánchez, L. Marcos-Vidal, P. M. Gordaliza, J. Santonja, J. Janssen, S. Carmona, M. Desco, and Y. Alemán-Gómez, “ABLE: Automated Brain Lines Extraction Based on Laplacian Surface Collapse,” *Neuroinformatics*, Aug. 2022. doi: [10.1007/s12021-022-09601-7](https://doi.org/10.1007/s12021-022-09601-7). [Online]. Available: <https://link.springer.com/10.1007/s12021-022-09601-7>.
- [2] A. Fernández-Pena, F. J. Navas-Sánchez, D. Martín de Blas, L. Marcos-Vidal, P. M. Gordaliza, I. Martinez-Tejada, J. Janssen, S. Carmona, M. Desco, and Y. Alemán-Gomez, “Estimation of Vertex-wise Sulcal Width Maps on Cortical Surfaces,” *bioRxiv*, Nov. 2022. doi: [10.1101/2022.11.09.515775](https://doi.org/10.1101/2022.11.09.515775). [Online]. Available: <https://www.biorxiv.org/content/10.1101/2022.11.09.515775v1>.
- [3] J. Janssen, C. Alloza, C. Díaz-Caneja, J. Santonja, L. Pina-Camacho, P. Gordaliza, *et al.*, “Longitudinal Allometry of Sulcal Morphology in Health and Schizophrenia,” *Journal of Neuroscience*, vol. 42, no. 18, 2022. doi: [10.1523/JNEUROSCI.0606-21.2022](https://doi.org/10.1523/JNEUROSCI.0606-21.2022).
- [4] F. Navas-Sánchez, D. Martín De Blas, A. Fernández-Pena, Y. Alemán-Gómez, A. Lage-Castellanos, L. Marcos-Vidal, *et al.*, “Corticospinal tract and motor cortex degeneration in pure hereditary spastic paraparesis type 4 (SPG4),” *Amyotrophic Lateral Sclerosis and Frontotemporal Degeneration*, vol. 23, no. 1-2, 2022. doi: [10.1080/21678421.2021.1962353](https://doi.org/10.1080/21678421.2021.1962353).
- [5] F. Navas-Sánchez, L. Marcos-Vidal, D. Martín de Blas, A. Fernández-Pena, Y. Alemán-Gómez, J. Guzmán-de-Villoria, *et al.*, “Tract-specific damage at spinal cord level in pure hereditary spastic paraplegia type 4: a diffusion tensor imaging study,” *Journal of Neurology*, vol. 269, no. 6, 2022. doi: [10.1007/s00415-021-10933-8](https://doi.org/10.1007/s00415-021-10933-8).
- [6] M. Martínez-García, M. Paternina-Die, E. Barba-Müller, D. Martín de Blas, L. Beumala, R. Cortizo, *et al.*, “Do pregnancy-induced brain changes reverse? The brain of a mother six years after parturition,” *Brain Sciences*, vol. 11, no. 2, 2021. doi: [10.3390/brainsci11020168](https://doi.org/10.3390/brainsci11020168).
- [7] F. Navas-Sánchez, A. Fernández-Pena, D. Martín de Blas, Y. Alemán-Gómez, L. Marcos-Vidal, J. Guzmán-de-Villoria, *et al.*, “Thalamic atrophy in patients with pure hereditary spastic paraplegia type 4,” *Journal of Neurology*, vol. 268, no. 7, 2021. doi: [10.1007/s00415-020-10387-4](https://doi.org/10.1007/s00415-020-10387-4).

- [8] C. M. Díaz-Caneja, C. Alloza, P. M. Gordaliza, A. Fernández-Pena, L. de Hoyos, J. Santonja, *et al.*, “Sex Differences in Lifespan Trajectories and Variability of Human Sulcal and Gyrus Morphology,” *Cerebral Cortex*, vol. 31, no. 11, pp. 5107–5120, Oct. 2021. doi: [10.1093/cercor/bhab145](https://doi.org/10.1093/cercor/bhab145). [Online]. Available: <https://academic.oup.com/cercor/article/31/11/5107/6309923>.
- [9] D. Talia, P. Trunfio, F. Marozzo, L. Belcastro, J. Garcia-Blas, D. del Rio, *et al.*, “A Novel Data-Centric Programming Model for Large-Scale Parallel Systems,” in *Lecture Notes in Computer Science (including subseries Lecture Notes in Artificial Intelligence and Lecture Notes in Bioinformatics)*, vol. 11997 LNCS, 2020, pp. 452–463. doi: [10.1007/978-3-030-48340-1_35](https://doi.org/10.1007/978-3-030-48340-1_35). [Online]. Available: http://link.springer.com/10.1007/978-3-030-48340-1_35.
- [10] G. F. Striedter, S. Srinivasan, and E. S. Monuki, “Cortical Folding: When, Where, How, and Why?” *Annual Review of Neuroscience*, vol. 38, no. 1, pp. 291–307, Jul. 2015. doi: [10.1146/annurev-neuro-071714-034128](https://doi.org/10.1146/annurev-neuro-071714-034128). [Online]. Available: <https://www.annualreviews.org/doi/10.1146/annurev-neuro-071714-034128>.
- [11] L. Ronan, N. Voets, C. Rua, A. Alexander-Bloch, M. Hough, C. Mackay, T. J. Crow, A. James, J. N. Giedd, and P. C. Fletcher, “Differential Tangential Expansion as a Mechanism for Cortical Gyration,” *Cerebral Cortex*, vol. 24, no. 8, pp. 2219–2228, Aug. 2014. doi: [10.1093/cercor/bht082](https://doi.org/10.1093/cercor/bht082). [Online]. Available: <https://academic.oup.com/cercor/article-lookup/doi/10.1093/cercor/bht082>.
- [12] P. Rakic, “Evolution of the neocortex: Perspective from developmental biology,” *Nature reviews. Neuroscience*, vol. 10, no. 10, p. 724, Oct. 2009. doi: [10.1038/NRN2719](https://doi.org/10.1038/NRN2719). [Online]. Available: <https://www.ncbi.nlm.nih.gov/pmc/articles/PMC2913577/>.
- [13] A. Kriegstein, S. Noctor, and V. Martínez-Cerdeño, “Patterns of neural stem and progenitor cell division may underlie evolutionary cortical expansion,” *Nature Reviews Neuroscience* 2006 7:11, vol. 7, no. 11, pp. 883–890, Oct. 2006. doi: [10.1038/nrn2008](https://doi.org/10.1038/nrn2008). [Online]. Available: <https://www.nature.com/articles/nrn2008>.
- [14] K. E. Garcia, C. D. Kroenke, and P. V. Bayly, “Mechanics of cortical folding: stress, growth and stability,” *Philosophical Transactions of the Royal Society B: Biological Sciences*, vol. 373, no. 1759, p. 20170321, Nov. 2018. doi: [10.1098/rstb.2017.0321](https://doi.org/10.1098/rstb.2017.0321). [Online]. Available: <https://royalsocietypublishing.org/doi/10.1098/rstb.2017.0321>.
- [15] W. Welker, “Why Does Cerebral Cortex Fissure and Fold?” In *Cerebral Cortex*, Springer US, 1990, pp. 3–136. doi: [10.1007/978-1-4615-3824-0_1](https://doi.org/10.1007/978-1-4615-3824-0_1). [Online]. Available: http://link.springer.com/10.1007/978-1-4615-3824-0_1.

- [16] L. Ronan and P. C. Fletcher, “From genes to folds: a review of cortical gyrification theory,” *Brain Structure and Function*, vol. 220, no. 5, pp. 2475–2483, Sep. 2015. doi: [10.1007/s00429-014-0961-z](https://doi.org/10.1007/s00429-014-0961-z). [Online]. Available: <http://link.springer.com/10.1007/s00429-014-0961-z>.
- [17] V. Fernández, C. Llinares-Benadero, and V. Borrell, “Cerebral cortex expansion and folding: what have we learned?” *The EMBO Journal*, vol. 35, no. 10, pp. 1021–1044, May 2016. doi: [10.15252/embj.201593701](https://doi.org/10.15252/embj.201593701). [Online]. Available: <https://onlinelibrary.wiley.com/doi/10.15252/embj.201593701>.
- [18] K. E. Garcia, X. Wang, and C. D. Kroenke, “A model of tension-induced fiber growth predicts white matter organization during brain folding,” *Nature Communications*, vol. 12, no. 1, p. 6681, Dec. 2021. doi: [10.1038/s41467-021-26971-9](https://doi.org/10.1038/s41467-021-26971-9). [Online]. Available: <https://www.nature.com/articles/s41467-021-26971-9>.
- [19] L. Del-Valle-Anton and V. Borrell, “Folding brains: from development to disease modeling,” *Physiological Reviews*, vol. 102, no. 2, pp. 511–550, Apr. 2022. doi: [10.1152/physrev.00016.2021](https://doi.org/10.1152/physrev.00016.2021). [Online]. Available: <https://journals.physiology.org/doi/10.1152/physrev.00016.2021>.
- [20] W. E. Le Gros Clark, “Deformation patterns on the cerebral cortex,” *Essays on Growth and Form*, pp. 1–22, 1945.
- [21] D. H. Barron, “An experimental analysis of some factors involved in the development of the fissure pattern of the cerebral cortex,” *Journal of Experimental Zoology*, vol. 113, no. 3, pp. 553–581, Apr. 1950. doi: [10.1002/JEZ.1401130304](https://doi.org/10.1002/JEZ.1401130304). [Online]. Available: <https://onlinelibrary.wiley.com/doi/10.1002/jez.1401130304>.
- [22] H. Chen, L. Guo, J. Nie, T. Zhang, X. Hu, and T. Liu, “A Dynamic Skull Model for Simulation of Cerebral Cortex Folding,” in *International Conference on Medical Image Computing and Computer-Assisted Intervention*, Pt 2, vol. 13, Springer, Berlin, Heidelberg, 2010, pp. 412–419. doi: [10.1007/978-3-642-15745-5_51](https://doi.org/10.1007/978-3-642-15745-5_51). [Online]. Available: <http://www.ncbi.nlm.nih.gov/pubmed/20879342>.
- [23] J. Nie, L. Guo, G. Li, C. Faraco, L. Stephen Miller, and T. Liu, “A computational model of cerebral cortex folding,” *Journal of Theoretical Biology*, vol. 264, no. 2, pp. 467–478, May 2010. doi: [10.1016/j.jtbi.2010.02.002](https://doi.org/10.1016/j.jtbi.2010.02.002). [Online]. Available: <https://pubmed.ncbi.nlm.nih.gov/20167224/>.
- [24] P. Bayly, L. Taber, and C. Kroenke, “Mechanical forces in cerebral cortical folding: A review of measurements and models,” *Journal of the Mechanical Behavior of Biomedical Materials*, vol. 29, pp. 568–581, Jan. 2014. doi: [10.1016/j.jmbbm.2013.02.018](https://doi.org/10.1016/j.jmbbm.2013.02.018). [Online]. Available: <https://linkinghub.elsevier.com/retrieve/pii/S175161611300074X>.

- [25] D. P. Richman, R. M. Stewart, J. Hutchinson, and V. S. Caviness, “Mechanical Model of Brain Convolutional Development,” *Science*, vol. 189, no. 4196, pp. 18–21, Jul. 1975. doi: [10.1126/science.1135626](https://doi.org/10.1126/science.1135626). [Online]. Available: <https://www.science.org/doi/10.1126/science.1135626>.
- [26] J. Dervaux and M. Ben Amar, “Morphogenesis of growing soft tissues,” *Physical Review Letters*, vol. 101, no. 6, p. 068 101, Aug. 2008. doi: [10.1103/PhysRevLett.101.068101](https://doi.org/10.1103/PhysRevLett.101.068101). [Online]. Available: <https://journals.aps.org/prl/abstract/10.1103/PhysRevLett.101.068101>.
- [27] T. Tallinen, J. Y. Chung, J. S. Biggins, and L. Mahadevan, “Gyrification from constrained cortical expansion,” *Proceedings of the National Academy of Sciences of the United States of America*, vol. 111, no. 35, pp. 12 667–12 672, Sep. 2014. doi: [10.1073/PNAS.1406015111](https://doi.org/10.1073/PNAS.1406015111). [Online]. Available: <https://www.pnas.org/doi/abs/10.1073/pnas.1406015111>.
- [28] T. Tallinen, J. Y. Chung, F. Rousseau, N. Girard, J. Lefèvre, and L. Mahadevan, “On the growth and form of cortical convolutions,” *Nature Physics* 2016 12:6, vol. 12, no. 6, pp. 588–593, Feb. 2016. doi: [10.1038/nphys3632](https://doi.org/10.1038/nphys3632). [Online]. Available: <https://www.nature.com/articles/nphys3632>.
- [29] G. Xu, A. K. Knutsen, K. Dikranian, C. D. Kroenke, P. V. Bayly, and L. A. Taber, “Axons Pull on the Brain, But Tension Does Not Drive Cortical Folding,” *Journal of biomechanical engineering*, vol. 132, no. 7, p. 071 013, Jul. 2010. doi: [10.1115/1.4001683](https://doi.org/10.1115/1.4001683). [Online]. Available: <https://www.ncbi.nlm.nih.gov/pmc/articles/PMC3170872/>.
- [30] D. C. Van Essen, “A tension-based theory of morphogenesis and compact wiring in the central nervous system,” *Nature*, vol. 385, no. 6614, pp. 313–318, Jan. 1997. doi: [10.1038/385313a0](https://doi.org/10.1038/385313a0). [Online]. Available: <http://www.nature.com/articles/385313a0>.
- [31] R. Toro and Y. Burnod, “A Morphogenetic Model for the Development of Cortical Convolutions,” *Cerebral Cortex*, vol. 15, no. 12, pp. 1900–1913, Dec. 2005. doi: [10.1093/cercor/bhi068](https://doi.org/10.1093/cercor/bhi068). [Online]. Available: <https://pubmed.ncbi.nlm.nih.gov/15758198/>.
- [32] S. R. Heidemann and R. E. Buxbaum, “Mechanical tension as a regulator of axonal development,” *eng, Neurotoxicology*, vol. 15, no. 1, pp. 95–107, 1994. [Online]. Available: <http://www.ncbi.nlm.nih.gov/pubmed/8090366>.
- [33] P. Lamoureux, S. R. Heidemann, N. R. Martzke, and K. E. Miller, “Growth and elongation within and along the axon,” *Developmental Neurobiology*, vol. 70, no. 3, pp. 135–149, Feb. 2010. doi: [10.1002/DNEU.20764](https://doi.org/10.1002/DNEU.20764).

- [34] D. C. Van Essen, “A 2020 view of tension-based cortical morphogenesis,” *Proceedings of the National Academy of Sciences of the United States of America*, vol. 117, no. 52, pp. 32 868–32 879, Dec. 2020. doi: [10 . 1073 / PNAS . 2016830117/- /DCSUPPLEMENTAL](https://doi.org/10.1073/PNAS.2016830117/-/DCSUPPLEMENTAL). [Online]. Available: <https://www.ncbi.nlm.nih.gov/pmc/articles/PMC7780001/>.
- [35] T. Sun and R. F. Hevner, “Growth and folding of the mammalian cerebral cortex: from molecules to malformations,” *Nature reviews. Neuroscience*, vol. 15, no. 4, p. 217, Apr. 2014. doi: [10.1038/NRN3707](https://doi.org/10.1038/NRN3707). [Online]. Available: <https://www.ncbi.nlm.nih.gov/pmc/articles/PMC4107216/>.
- [36] P. V. Bayly, R. J. Okamoto, G. Xu, Y. Shi, and L. A. Taber, “A cortical folding model incorporating stress-dependent growth explains gyral wavelengths and stress patterns in the developing brain,” *Physical biology*, vol. 10, no. 1, p. 016 005, Feb. 2013. doi: [10 . 1088 / 1478 - 3975 / 10 / 1 / 016005](https://doi.org/10.1088/1478-3975/10/1/016005). [Online]. Available: <https://www.ncbi.nlm.nih.gov/pmc/articles/PMC3616769/>.
- [37] C. C. Hilgetag and H. Barbas, “Developmental mechanics of the primate cerebral cortex,” *Anatomy and Embryology*, vol. 210, no. 5-6, pp. 411–417, Dec. 2005. doi: [10.1007/S00429-005-0041-5/FIGURES/4](https://doi.org/10.1007/S00429-005-0041-5/FIGURES/4). [Online]. Available: <https://link.springer.com/article/10.1007/s00429-005-0041-5>.
- [38] A. Gupta, L. H. Tsai, and A. Wynshaw-Boris, “Life is a journey: a genetic look at neocortical development,” *Nature Reviews Genetics* 2002 3:5, vol. 3, no. 5, pp. 342–355, 2002. doi: [10.1038/nrg799](https://doi.org/10.1038/nrg799). [Online]. Available: <https://www.nature.com/articles/nrg799>.
- [39] K. Brodmann, *Vergleichende Lokalisationslehre der Grosshirnrinde in ihren Prinzipien dargestellt auf Grund des Zellenbaues*. Barth, 1909.
- [40] D. Purves, G. J. Augustine, D. Fitzpatrick, L. C. Katz, A.-S. LaMantia, J. O. McNamara, and S. M. Williams, “An Overview of Cortical Structure,” in *Neuroscience*, D. Purves, G. J. Augustine, D. Fitzpatrick, L. C. Katz, A.-S. LaMantia, J. O. McNamara, and S. M. Williams, Eds., 2nd edition, Sinauer Associates, 2001, ch. Chapter 26. [Online]. Available: <https://www.ncbi.nlm.nih.gov/books/NBK10870/>.
- [41] K. Amunts and K. Zilles, “Architectonic Mapping of the Human Brain beyond Brodmann,” *Neuron*, vol. 88, no. 6, pp. 1086–1107, Dec. 2015. doi: [10.1016/j.neuron.2015.12.001](https://doi.org/10.1016/j.neuron.2015.12.001). [Online]. Available: <http://dx.doi.org/10.1016/j.neuron.2015.12.001>.
- [42] A. J. Barkovich, R. Guerrini, R. I. Kuzniecky, G. D. Jackson, and W. B. Dobyns, “A developmental and genetic classification for malformations of cortical development: update 2012,” *Brain*, vol. 135, no. 5, pp. 1348–1369, May 2012. doi: [10.1093/BRAIN/AWS019](https://doi.org/10.1093/BRAIN/AWS019). [Online]. Available: <https://academic.oup.com/brain/article/135/5/1348/304670>.

- [43] L. Garey, “When cortical development goes wrong: schizophrenia as a neurodevelopmental disease of microcircuits,” *Journal of Anatomy*, vol. 217, no. 4, pp. 324–333, Oct. 2010. doi: [10.1111/J.1469-7580.2010.01231.X](https://doi.org/10.1111/J.1469-7580.2010.01231.X). [Online]. Available: <https://onlinelibrary.wiley.com/doi/10.1111/j.1469-7580.2010.01231.x>.
- [44] A. Cachia, M. L. Paillère-Martinot, A. Galinowski, D. Januel, R. de Beaurepaire, F. Bellivier, *et al.*, “Cortical folding abnormalities in schizophrenia patients with resistant auditory hallucinations,” *NeuroImage*, vol. 39, no. 3, pp. 927–935, Feb. 2008. doi: [10.1016/j.neuroimage.2007.08.049](https://doi.org/10.1016/j.neuroimage.2007.08.049). [Online]. Available: <https://pubmed.ncbi.nlm.nih.gov/17988891/>.
- [45] J. Janssen, Y. Alemán-Gómez, H. Schnack, E. Balaban, L. Pina-Camacho, F. Alfaro-Almagro, *et al.*, “Cortical morphology of adolescents with bipolar disorder and with schizophrenia,” *Schizophrenia Research*, vol. 158, no. 1-3, pp. 91–99, Sep. 2014. doi: [10.1016/j.schres.2014.06.040](https://doi.org/10.1016/j.schres.2014.06.040). [Online]. Available: <https://linkinghub.elsevier.com/retrieve/pii/S0920996414003545>.
- [46] B. Cao, B. Mwangi, I. C. Passos, M. J. Wu, Z. Keser, G. B. Zunta-Soares, D. Xu, K. M. Hasan, and J. C. Soares, “Lifespan Gyrfication Trajectories of Human Brain in Healthy Individuals and Patients with Major Psychiatric Disorders,” *Scientific Reports 2017 7:1*, vol. 7, no. 1, pp. 1–8, Mar. 2017. doi: [10.1038/s41598-017-00582-1](https://doi.org/10.1038/s41598-017-00582-1). [Online]. Available: <https://www.nature.com/articles/s41598-017-00582-1>.
- [47] S. J. Palmen, H. Van Engeland, P. R. Hof, and C. Schmitz, “Neuropathological findings in autism,” *Brain*, vol. 127, no. 12, pp. 2572–2583, Dec. 2004. doi: [10.1093/BRAIN/AWH287](https://doi.org/10.1093/BRAIN/AWH287). [Online]. Available: <https://academic.oup.com/brain/article/127/12/2572/335111>.
- [48] C. Falcone, N. Y. Mevises, T. Hong, B. Dufour, X. Chen, S. C. Noctor, and V. Martínez Cerdeño, “Neuronal and glial cell number is altered in a cortical layer-specific manner in autism,” *Autism*, vol. 25, no. 8, pp. 2238–2253, Nov. 2021. doi: [10.1177/13623613211014408](https://doi.org/10.1177/13623613211014408). [Online]. Available: <https://journals.sagepub.com/doi/full/10.1177/13623613211014408>.
- [49] C. W. Nordahl, D. Dierker, I. Mostafavi, C. M. Schumann, S. M. Rivera, D. G. Amaral, and D. C. Van Essen, “Cortical folding abnormalities in autism revealed by surface-based morphometry,” *The Journal of neuroscience : the official journal of the Society for Neuroscience*, vol. 27, no. 43, pp. 11 725–11 735, Oct. 2007. doi: [10.1523/JNEUROSCI.0777-07.2007](https://doi.org/10.1523/JNEUROSCI.0777-07.2007). [Online]. Available: <https://pubmed.ncbi.nlm.nih.gov/17959814/>.
- [50] G. Auzias, M. Viellard, S. Takerkart, N. Villeneuve, F. Poinso, D. D. Fonséca, N. Girard, and C. Deruelle, “Atypical sulcal anatomy in young children with autism

- spectrum disorder,” *NeuroImage: Clinical*, vol. 4, pp. 593–603, Jan. 2014. doi: [10.1016/J.NICL.2014.03.008](https://doi.org/10.1016/J.NICL.2014.03.008).
- [51] D. Sasabayashi, T. Takahashi, Y. Takayanagi, and M. Suzuki, “Anomalous brain gyration patterns in major psychiatric disorders: a systematic review and trans-diagnostic integration,” *Translational Psychiatry*, vol. 11, no. 1, pp. 1–12, Mar. 2021. doi: [10.1038/s41398-021-01297-8](https://doi.org/10.1038/s41398-021-01297-8). [Online]. Available: <https://www.nature.com/articles/s41398-021-01297-8>.
- [52] G. Rajkowska, “Cell pathology in bipolar disorder,” *Bipolar Disorders*, vol. 4, no. 2, pp. 105–116, Apr. 2002. doi: [10.1034/J.1399-5618.2002.01149.X](https://doi.org/10.1034/J.1399-5618.2002.01149.X). [Online]. Available: <https://onlinelibrary.wiley.com/doi/10.1034/j.1399-5618.2002.01149.x>.
- [53] G. Rajkowska, J. J. Miguel-Hidalgo, J. Wei, G. Dilley, S. D. Pittman, H. Y. Meltzer, J. C. Overholser, B. L. Roth, and C. A. Stockmeier, “Morphometric evidence for neuronal and glial prefrontal cell pathology in major depression,” *Biological Psychiatry*, vol. 45, no. 9, pp. 1085–1098, May 1999. doi: [10.1016/S0006-3223\(99\)00041-4](https://doi.org/10.1016/S0006-3223(99)00041-4).
- [54] L. A. O’Leary and N. Mechawar, “Implication of cerebral astrocytes in major depression: A review of fine neuroanatomical evidence in humans,” *Glia*, vol. 69, no. 9, pp. 2077–2099, Sep. 2021. doi: [10.1002/GLIA.23994](https://doi.org/10.1002/GLIA.23994). [Online]. Available: <https://onlinelibrary.wiley.com/doi/10.1002/glia.23994>.
- [55] X. Li, W. Wang, P. Wang, C. Hao, and Z. Li, “Atypical sulcal pattern in boys with attention-deficit/hyperactivity disorder,” *Human Brain Mapping*, vol. 42, no. 13, pp. 4362–4371, Sep. 2021. doi: [10.1002/HBM.25552](https://doi.org/10.1002/HBM.25552).
- [56] X. W. Li, Y. H. Jiang, W. Wang, X. X. Liu, and Z. Y. Li, “Brain morphometric abnormalities in boys with attention-deficit/hyperactivity disorder revealed by sulcal pits-based analyses,” *CNS Neuroscience and Therapeutics*, vol. 27, no. 3, pp. 299–307, Mar. 2021. doi: [10.1111/CNS.13445](https://doi.org/10.1111/CNS.13445).
- [57] K. Zilles, N. Palomero-Gallagher, and K. Amunts, “Development of cortical folding during evolution and ontogeny,” *Trends in Neurosciences*, vol. 36, no. 5, pp. 275–284, May 2013. doi: [10.1016/J.TINS.2013.01.006](https://doi.org/10.1016/J.TINS.2013.01.006).
- [58] S. Ogawa, T. M. Lee, A. R. Kay, and D. W. Tank, “Brain magnetic resonance imaging with contrast dependent on blood oxygenation,” *Proceedings of the National Academy of Sciences of the United States of America*, vol. 87, no. 24, pp. 9868–9872, 1990. doi: [10.1073/PNAS.87.24.9868](https://doi.org/10.1073/PNAS.87.24.9868). [Online]. Available: <https://pubmed.ncbi.nlm.nih.gov/2124706/>.
- [59] D. Le Bihan, “Diffusion, Perfusion and Functional MRI,” *Functional MRI*, pp. 23–27, 1996. doi: [10.1007/978-88-470-2194-5_5](https://doi.org/10.1007/978-88-470-2194-5_5). [Online]. Available: https://link.springer.com/chapter/10.1007/978-88-470-2194-5_5.

- [60] M. Chappell, T. Okellm, and M. Jenkinson, “Short introduction to MRI Physics for Neuroimaging,” in *Introduction to Neuroimaging Analysis*, M. Jenkinson and M. Chappell, Eds., Oxford: Oxford University Press, 2018, pp. 1–25. [Online]. Available: https://www.fmrib.ox.ac.uk/primers/appendices/mri_physics.pdf.
- [61] N. J. Tustison, B. B. Avants, P. A. Cook, Y. Zheng, A. Egan, P. A. Yushkevich, and J. C. Gee, “N4ITK: Improved N3 Bias Correction,” *IEEE transactions on medical imaging*, vol. 29, no. 6, p. 1310, Jun. 2010. doi: [10.1109/TMI.2010.2046908](https://doi.org/10.1109/TMI.2010.2046908). [Online]. Available: <https://www.ncbi.nlm.nih.gov/pmc/articles/PMC3071855/>.
- [62] I. C. Wright, P. K. McGuire, J. B. Poline, J. M. Travers, R. M. Murray, C. D. Frith, R. S. Frackowiak, and K. J. Friston, “A Voxel-Based Method for the Statistical Analysis of Gray and White Matter Density Applied to Schizophrenia,” *NeuroImage*, vol. 2, no. 4, pp. 244–252, Dec. 1995. doi: [10.1006/NIMG.1995.1032](https://doi.org/10.1006/NIMG.1995.1032).
- [63] J. Ashburner and K. J. Friston, “Voxel-Based Morphometry—The Methods,” *NeuroImage*, vol. 11, no. 6, pp. 805–821, Jun. 2000. doi: [10.1006/NIMG.2000.0582](https://doi.org/10.1006/NIMG.2000.0582).
- [64] S. S. Keller and N. Roberts, “Voxel-based morphometry of temporal lobe epilepsy: An introduction and review of the literature,” *Epilepsia*, vol. 49, no. 5, pp. 741–757, May 2008. doi: [10.1111/J.1528-1167.2007.01485.X](https://doi.org/10.1111/J.1528-1167.2007.01485.X). [Online]. Available: <https://onlinelibrary.wiley.com/doi/10.1111/j.1528-1167.2007.01485.x>.
- [65] C. Hutton, B. Draganski, J. Ashburner, and N. Weiskopf, “A comparison between voxel-based cortical thickness and voxel-based morphometry in normal aging,” *NeuroImage*, vol. 48, no. 2, pp. 371–380, Nov. 2009. doi: [10.1016/J.NEUROIMAGE.2009.06.043](https://doi.org/10.1016/J.NEUROIMAGE.2009.06.043).
- [66] S. Ramanoël, E. Hoyau, L. Kauffmann, F. Renard, C. Pichat, N. Boudiaf, A. Krainik, A. Jaillard, and M. Baci, “Gray matter volume and cognitive performance during normal aging. A voxel-based morphometry study,” *Frontiers in Aging Neuroscience*, vol. 10, no. AUG, p. 235, Aug. 2018. doi: [10.3389/FNAGI.2018.00235/BIBTEX](https://doi.org/10.3389/FNAGI.2018.00235/BIBTEX).
- [67] F. Zhang, S. Tian, S. Chen, Y. Ma, X. Li, and X. Guo, “Voxel-Based Morphometry: Improving the Diagnosis of Alzheimer’s Disease Based on an Extreme Learning Machine Method from the ADNI cohort,” *Neuroscience*, vol. 414, pp. 273–279, Aug. 2019. doi: [10.1016/J.NEUROSCIENCE.2019.05.014](https://doi.org/10.1016/J.NEUROSCIENCE.2019.05.014).
- [68] S. Kandilarova, D. Stoyanov, N. Sirakov, M. Maes, and K. Specht, “Reduced grey matter volume in frontal and temporal areas in depression: contributions from voxel-based morphometry study,” *Acta Neuropsychiatrica*, vol. 31, no. 5, pp. 252–257, Oct. 2019. doi: [10.1017/NEU.2019.20](https://doi.org/10.1017/NEU.2019.20). [Online]. Available: <https://www.cambridge.org/core/journals/acta-neuropsychiatrica/>

- [article/reduced-grey-matter-volume-in-frontal-and-temporal-areas-in-depression-contributions-from-voxelbased-morphometry-study/A37D540A48A8E30316C990B5425ED101.](#)
- [69] Y. Tang, M. Wang, T. Zheng, F. Yuan, H. Yang, F. Han, and G. Chen, “Grey matter volume alterations in trigeminal neuralgia: A systematic review and meta-analysis of voxel-based morphometry studies,” *Progress in Neuro-Psychopharmacology and Biological Psychiatry*, vol. 98, p. 109 821, Mar. 2020. doi: [10.1016/J.PNPBP.2019.109821](#).
 - [70] K. Keramatian, T. Chakrabarty, G. Saraf, J. V. Pinto, and L. N. Yatham, “Grey matter abnormalities in first-episode mania: A systematic review and meta-analysis of voxel-based morphometry studies,” *Bipolar Disorders*, vol. 23, no. 3, pp. 228–240, May 2021. doi: [10.1111/BDI.12995](#). [Online]. Available: <https://onlinelibrary.wiley.com/doi/10.1111/bdi.12995>.
 - [71] V. Rajagopalan and E. P. Piro, “Disparate voxel based morphometry (VBM) results between SPM and FSL softwares in ALS patients with frontotemporal dementia: which VBM results to consider?” *BMC neurology*, vol. 15, no. 1, Mar. 2015. doi: [10.1186/S12883-015-0274-8](#). [Online]. Available: <https://pubmed.ncbi.nlm.nih.gov/25879588/>.
 - [72] V. Popescu, M. M. Schoonheim, A. Versteeg, N. Chaturvedi, M. Jonker, R. X. De Menezes, F. G. Garre, B. M. Uitdehaag, F. Barkhof, and H. Vrenken, “Grey Matter Atrophy in Multiple Sclerosis: Clinical Interpretation Depends on Choice of Analysis Method,” *PloS one*, vol. 11, no. 1, Jan. 2016. doi: [10.1371/JOURNAL.PONE.0143942](#). [Online]. Available: <https://pubmed.ncbi.nlm.nih.gov/26745873/>.
 - [73] X. Zhou, R. Wu, Y. Zeng, Z. Qi, S. Ferraro, L. Xu, *et al.*, “Choice of Voxel-based Morphometry processing pipeline drives variability in the location of neuroanatomical brain markers,” *Communications Biology*, vol. 5, no. 1, Dec. 2022. doi: [10.1038/S42003-022-03880-1](#). [Online]. Available: <https://www.ncbi.nlm.nih.gov/pmc/articles/PMC9448776/>.
 - [74] A. Mechelli, C. Price, K. Friston, and J. Ashburner, “Voxel-Based Morphometry of the Human Brain: Methods and Applications,” *Current Medical Imaging Reviews*, vol. 1, no. 2, pp. 105–113, Jun. 2005. doi: [10.2174/1573405054038726](#). [Online]. Available: <http://www.eurekaselect.com/openurl/content.php?genre=article&issn=1573-4056&volume=1&issue=2&spage=105>.
 - [75] B. Fischl, A. Liu, and A. M. Dale, “Automated manifold surgery: Constructing geometrically accurate and topologically correct models of the human cerebral cortex,” *IEEE Transactions on Medical Imaging*, vol. 20, no. 1, pp. 70–80, Jan. 2001. doi: [10.1109/42.906426](#).

- [76] B. Fischl, M. I. Sereno, and A. M. Dale, "Cortical Surface-Based Analysis," *NeuroImage*, vol. 9, no. 2, pp. 195–207, Feb. 1999. doi: [10.1006/nimg.1998.0396](https://doi.org/10.1006/nimg.1998.0396). [Online]. Available: <https://linkinghub.elsevier.com/retrieve/pii/S1053811998903962>.
- [77] A. M. Dale, B. Fischl, and M. I. Sereno, "Cortical Surface-Based Analysis," *NeuroImage*, vol. 9, no. 2, pp. 179–194, Feb. 1999. doi: [10.1006/nimg.1998.0395](https://doi.org/10.1006/nimg.1998.0395). [Online]. Available: <https://linkinghub.elsevier.com/retrieve/pii/S1053811998903950>.
- [78] D. W. Shattuck and R. M. Leahy, "BrainSuite: An automated cortical surface identification tool," *Medical Image Analysis*, vol. 6, no. 2, S. L. Delp, A. M. DiGoia, and B. Jaramaz, Eds., pp. 129–142, Jun. 2002. doi: [10.1016/S1361-8415\(02\)00054-3](https://doi.org/10.1016/S1361-8415(02)00054-3). [Online]. Available: http://link.springer.com/10.1007/978-3-540-40899-4_6.
- [79] C. Fischer, G. Operto, S. Laguitton, M. Perrot, I. Denghien, and D. Rivière, "Morphologist 2012: the new morphological pipeline of BrainVISA," *Proceedings of the 18th HBM Scientific Meeting, Beijing, China. NeuroImage*, 2012.
- [80] B. Fischl, M. I. Sereno, R. B. Tootell, and A. M. Dale, "High-resolution intersubject averaging and a coordinate system for the cortical surface," *Human Brain Mapping*, vol. 8, no. 4, pp. 272–284, 1999. doi: [10.1002/\(SICI\)1097-0193\(1999\)8:4<272::AID-HBM10>3.0.CO;2-4](https://doi.org/10.1002/(SICI)1097-0193(1999)8:4<272::AID-HBM10>3.0.CO;2-4). [Online]. Available: <http://www.pubmedcentral.nih.gov/articlerender.fcgi?artid=PMC6873338>.
- [81] T. S. Coalson, D. C. Van Essen, and M. F. Glasser, "The impact of traditional neuroimaging methods on the spatial localization of cortical areas," *Proceedings of the National Academy of Sciences of the United States of America*, vol. 115, no. 27, E6356–E6365, Jul. 2018. doi: [10.1073/pnas.1801582115](https://doi.org/10.1073/pnas.1801582115). [Online]. Available: <https://www.pnas.org/doi/abs/10.1073/pnas.1801582115>.
- [82] B. T. Yeo, M. R. Sabuncu, T. Vercauteren, N. Ayache, B. Fischl, and P. Golland, "Spherical demons: fast diffeomorphic landmark-free surface registration," *IEEE transactions on medical imaging*, vol. 29, no. 3, pp. 650–668, Mar. 2010. doi: [10.1109/TMI.2009.2030797](https://doi.org/10.1109/TMI.2009.2030797). [Online]. Available: <https://pubmed.ncbi.nlm.nih.gov/19709963/>.
- [83] E. C. Robinson, S. Jbabdi, M. F. Glasser, J. Andersson, G. C. Burgess, M. P. Harms, S. M. Smith, D. C. Van Essen, and M. Jenkinson, "MSM: A new flexible framework for Multimodal Surface Matching," *NeuroImage*, vol. 100, pp. 414–426, Oct. 2014. doi: [10.1016/j.neuroimage.2014.05.069](https://doi.org/10.1016/j.neuroimage.2014.05.069). [Online]. Available: <https://www.ncbi.nlm.nih.gov/pmc/articles/PMC4190319/>.

- [84] F. Zhao, Z. Wu, F. Wang, W. Lin, S. Xia, D. Shen, L. Wang, and G. Li, "S3Reg: Superfast Spherical Surface Registration Based on Deep Learning," *IEEE Transactions on Medical Imaging*, vol. 40, no. 8, pp. 1964–1976, Aug. 2021. doi: [10.1109/TMI.2021.3069645](https://doi.org/10.1109/TMI.2021.3069645).
- [85] A. M. Dale and M. I. Sereno, "Improved Localizadon of Cortical Activity by Combining EEG and MEG with MRI Cortical Surface Reconstruction: A Linear Approach," *Journal of Cognitive Neuroscience*, vol. 5, no. 2, pp. 162–176, Apr. 1993. doi: [10.1162/JOCN.1993.5.2.162](https://doi.org/10.1162/JOCN.1993.5.2.162). [Online]. Available: <https://direct.mit.edu/jocn/article/5/2/162/3095/Improved-Localizadon-of-Cortical-Activity-by>.
- [86] X. Chen and F. Schmitt, "Intrinsic surface properties from surface triangulation," *Lecture Notes in Computer Science (including subseries Lecture Notes in Artificial Intelligence and Lecture Notes in Bioinformatics)*, vol. 588 LNCS, pp. 739–743, 1992. doi: [10.1007/3-540-55426-2_{_}83](https://doi.org/10.1007/3-540-55426-2_{_}83).
- [87] R. S. Desikan, F. Ségonne, B. Fischl, B. T. Quinn, B. C. Dickerson, D. Blacker, *et al.*, "An automated labeling system for subdividing the human cerebral cortex on MRI scans into gyral based regions of interest," *NeuroImage*, vol. 31, no. 3, pp. 968–980, 2006. doi: [10.1016/j.neuroimage.2006.01.021](https://doi.org/10.1016/j.neuroimage.2006.01.021).
- [88] C. Destrieux, B. Fischl, A. Dale, and E. Halgren, "Automatic parcellation of human cortical gyri and sulci using standard anatomical nomenclature," *NeuroImage*, vol. 53, no. 1, pp. 1–15, Oct. 2010. doi: [10.1016/J.NEUROIMAGE.2010.06.010](https://doi.org/10.1016/J.NEUROIMAGE.2010.06.010).
- [89] B. T. Thomas Yeo, F. M. Krienen, J. Sepulcre, M. R. Sabuncu, D. Lashkari, M. Hollinshead, *et al.*, "The organization of the human cerebral cortex estimated by intrinsic functional connectivity," *Journal of Neurophysiology*, vol. 106, no. 3, p. 1125, Sep. 2011. doi: [10.1152/JN.00338.2011](https://doi.org/10.1152/JN.00338.2011). [Online]. Available: <https://www.ncbi.nlm.nih.gov/pmc/articles/PMC3174820/>.
- [90] P. Rakic, "Specification of Cerebral Cortical Areas," *Science*, vol. 241, no. 4862, pp. 170–176, Jul. 1988.
- [91] K. Zilles and K. Amunts, "Centenary of Brodmann's map — conception and fate," *Nature Reviews Neuroscience*, vol. 11, no. 2, pp. 139–145, Feb. 2010. doi: [10.1038/nrn2776](https://doi.org/10.1038/nrn2776). [Online]. Available: <https://www.nature.com/articles/nrn2776>.
- [92] A. M. Winkler, M. R. Sabuncu, B. T. Yeo, B. Fischl, D. N. Greve, P. Kochunov, T. E. Nichols, J. Blangero, and D. C. Glahn, "Measuring and comparing brain cortical surface area and other areal quantities," *NeuroImage*, vol. 61, no. 4, pp. 1428–1443, Jul. 2012. doi: [10.1016/J.NEUROIMAGE.2012.03.026](https://doi.org/10.1016/J.NEUROIMAGE.2012.03.026).

- [93] L. M. Rimol, R. Nesvåg, D. J. Hagler, Ø. Bergmann, C. Fennema-Notestine, C. B. Hartberg, *et al.*, “Cortical Volume, Surface Area, and Thickness in Schizophrenia and Bipolar Disorder,” *Biological Psychiatry*, vol. 71, no. 6, pp. 552–560, Mar. 2012. doi: [10.1016/J.BIOPSYCH.2011.11.026](https://doi.org/10.1016/J.BIOPSYCH.2011.11.026).
- [94] D. Sun, G. W. Stuart, M. Jenkinson, S. J. Wood, P. D. McGorry, D. Velakoulis, *et al.*, “Brain surface contraction mapped in first-episode schizophrenia: a longitudinal magnetic resonance imaging study,” *Molecular psychiatry*, vol. 14, no. 10, pp. 976–986, 2009. doi: [10.1038/MP.2008.34](https://doi.org/10.1038/MP.2008.34). [Online]. Available: <https://pubmed.ncbi.nlm.nih.gov/18607377/>.
- [95] A. H. Joyner, J. C. Roddey, C. S. Bloss, T. E. Bakken, L. M. Rimol, I. Melle, *et al.*, “A common MECP2 haplotype associates with reduced cortical surface area in humans in two independent populations,” *Proceedings of the National Academy of Sciences of the United States of America*, vol. 106, no. 36, pp. 15 483–15 488, Sep. 2009. doi: [10.1073/PNAS.0901866106](https://doi.org/10.1073/PNAS.0901866106) / SUPPL{_}FILE / 0901866106SI.PDF. [Online]. Available: <https://www.pnas.org/doi/abs/10.1073/pnas.0901866106>.
- [96] J. Hill, T. Inder, J. Neil, D. Dierker, J. Harwell, and D. Van Essen, “Similar patterns of cortical expansion during human development and evolution,” *Proceedings of the National Academy of Sciences of the United States of America*, vol. 107, no. 29, pp. 13 135–13 140, Jul. 2010. doi: [10.1073/PNAS.1001229107](https://doi.org/10.1073/PNAS.1001229107) / SUPPL{_}FILE / PNAS.201001229SI.PDF. [Online]. Available: <https://www.pnas.org/doi/abs/10.1073/pnas.1001229107>.
- [97] J. Jelsing, E. Rostrup, K. Markenroth, O. B. Paulson, H. J. G. Gundersen, R. Hemmingsen, and B. Pakkenberg, “Assessment of in vivo MR imaging compared to physical sections in vitro—A quantitative study of brain volumes using stereology,” *NeuroImage*, vol. 26, no. 1, pp. 57–65, May 2005. doi: [10.1016/j.neuroimage.2005.01.005](https://doi.org/10.1016/j.neuroimage.2005.01.005). [Online]. Available: <https://linkinghub.elsevier.com/retrieve/pii/S1053811905000327>.
- [98] M. S. Panizzon, C. Fennema-Notestine, L. T. Eyler, T. L. Jernigan, E. Prom-Wormley, M. Neale, *et al.*, “Distinct Genetic Influences on Cortical Surface Area and Cortical Thickness,” *Cerebral Cortex*, vol. 19, no. 11, pp. 2728–2735, Nov. 2009. doi: [10.1093/CERCOR/BHP026](https://doi.org/10.1093/CERCOR/BHP026). [Online]. Available: <https://academic.oup.com/cercor/article/19/11/2728/381508>.
- [99] J. C. Masdeu, “Tau and Cortical Thickness in Alzheimer Disease,” *JAMA Neurology*, vol. 74, no. 4, p. 390, Apr. 2017. doi: [10.1001/jamaneurol.2016.5701](https://doi.org/10.1001/jamaneurol.2016.5701). [Online]. Available: <https://pubmed.ncbi.nlm.nih.gov/28241165/>.
- [100] B. H. Kim, Y. H. Choi, J. J. Yang, S. Kim, K. Nho, and J. M. Lee, “Identification of Novel Genes Associated with Cortical Thickness in Alzheimer’s Disease: Systems Biology Approach to Neuroimaging Endophenotype,” *Journal of Alzheimer’s disease : JAD*, vol. 75, no. 2, pp. 531–545, 2020. doi: [10.3233/](https://doi.org/10.3233/)

- JAD-191175. [Online]. Available: <https://pubmed.ncbi.nlm.nih.gov/32310165/>.
- [101] T. Jubault, J. F. Gagnon, S. Karama, A. Ptito, A. L. Lafontaine, A. C. Evans, and O. Monchi, “Patterns of cortical thickness and surface area in early Parkinson’s disease,” *NeuroImage*, vol. 55, no. 2, pp. 462–467, Mar. 2011. doi: [10.1016/J.NEUROIMAGE.2010.12.043](https://doi.org/10.1016/j.neuroimage.2010.12.043).
 - [102] Z. Huang, D. Ruan, B. Huang, T. Zhou, C. Shi, X. Yu, R. C. K. Chan, Y. Wang, and C. Pu, “Negative symptoms correlate with altered brain structural asymmetry in amygdala and superior temporal region in schizophrenia patients,” *Frontiers in psychiatry*, vol. 13, Sep. 2022. doi: [10.3389/FPSYT.2022.1000560](https://doi.org/10.3389/fpsyt.2022.1000560). [Online]. Available: <https://pubmed.ncbi.nlm.nih.gov/36226098/>.
 - [103] V. J. Williams, J. Juranek, P. Cirino, and J. M. Fletcher, “Cortical Thickness and Local Gyrification in Children with Developmental Dyslexia,” *Cerebral Cortex*, vol. 28, no. 3, pp. 963–973, Mar. 2018. doi: [10.1093/cercor/bhx001](https://doi.org/10.1093/cercor/bhx001). [Online]. Available: <https://pubmed.ncbi.nlm.nih.gov/28108497/>.
 - [104] Y. Aleman-Gomez, J. Janssen, H. Schnack, E. Balaban, L. Pina-Camacho, F. Alfaro-Almagro, *et al.*, “The Human Cerebral Cortex Flattens during Adolescence,” *Journal of Neuroscience*, vol. 33, no. 38, pp. 15 004–15 010, Sep. 2013. doi: [10.1523/JNEUROSCI.1459-13.2013](https://doi.org/10.1523/JNEUROSCI.1459-13.2013). [Online]. Available: <https://www.jneurosci.org/content/33/38/15004>.
 - [105] S. Carmona, M. Martínez-García, M. Paternina-Die, E. Barba-Müller, L. M. Wierenga, Y. Alemán-Gómez, *et al.*, “Pregnancy and adolescence entail similar neuroanatomical adaptations: A comparative analysis of cerebral morphometric changes,” *Human Brain Mapping*, vol. 40, no. 7, pp. 2143–2152, May 2019. doi: [10.1002/HBM.24513](https://doi.org/10.1002/HBM.24513).
 - [106] E. Hoekzema, E. Barba-Müller, C. Pozzobon, M. Picado, F. Lucco, D. García-García, *et al.*, “Pregnancy leads to long-lasting changes in human brain structure,” *Nature Neuroscience* 2016 20:2, vol. 20, no. 2, pp. 287–296, Dec. 2016. doi: [10.1038/nn.4458](https://doi.org/10.1038/nn.4458). [Online]. Available: <https://www.nature.com/articles/nn.4458>.
 - [107] B. Fischl and A. M. Dale, “Measuring the thickness of the human cerebral cortex from magnetic resonance images,” *Proceedings of the National Academy of Sciences of the United States of America*, vol. 97, no. 20, pp. 11 050–11 055, Sep. 2000. doi: [10.1073/PNAS.200033797](https://doi.org/10.1073/PNAS.200033797). [Online]. Available: <https://pubmed.ncbi.nlm.nih.gov/10984517/>.
 - [108] S. R. Das, B. B. Avants, M. Grossman, and J. C. Gee, “Registration based cortical thickness measurement,” *NeuroImage*, vol. 45, no. 3, pp. 867–879, Apr. 2009. doi: [10.1016/J.NEUROIMAGE.2008.12.016](https://doi.org/10.1016/j.neuroimage.2008.12.016).

- [109] J. Lee, J. M. Lee, J. H. Kim, I. Y. Kim, A. C. Evans, and S. I. Kim, “A novel quantitative validation of the cortical surface reconstruction algorithm using MRI phantom: Issues on local geometric accuracy and cortical thickness,” *Lecture Notes in Computer Science (including subseries Lecture Notes in Artificial Intelligence and Lecture Notes in Bioinformatics)*, vol. 4190 LNCS - I, pp. 183–190, 2006. doi: [10.1007/11866565_23](https://doi.org/10.1007/11866565_23). [Online]. Available: https://link.springer.com/chapter/10.1007/11866565_23.
- [110] P. Kochunov, J. F. Mangin, T. Coyle, J. Lancaster, P. Thompson, D. Rivière, *et al.*, “Age-related morphology trends of cortical sulci,” *Human Brain Mapping*, vol. 26, no. 3, p. 210, Nov. 2005. doi: [10.1002/HBM.20198](https://doi.org/10.1002/HBM.20198). [Online]. Available: <https://www.ncbi.nlm.nih.gov/pmc/articles/PMC6871665/>.
- [111] A. M. Winkler, D. N. Greve, K. J. Bjuland, T. E. Nichols, M. R. Sabuncu, A. K. Håberg, J. Skranes, and L. M. Rimol, “Joint Analysis of Cortical Area and Thickness as a Replacement for the Analysis of the Volume of the Cerebral Cortex,” *Cerebral Cortex*, vol. 28, no. 2, pp. 738–749, Feb. 2018. doi: [10.1093/CERCOR/BHX308](https://doi.org/10.1093/CERCOR/BHX308). [Online]. Available: <https://academic.oup.com/cercor/article/28/2/738/4668693>.
- [112] G. Lohmann, D. Y. von Cramon, and H. Steinmetz, “Sulcal variability of twins,” *Cerebral Cortex*, vol. 9, no. 7, pp. 754–63, Oct. 1999. doi: [10.1093/cercor/9.7.754](https://doi.org/10.1093/cercor/9.7.754). [Online]. Available: <https://pubmed.ncbi.nlm.nih.gov/10554998/>.
- [113] G. Lohmann, D. Y. Von Cramon, and A. C. Colchester, “Deep Sulcal Landmarks Provide an Organizing Framework for Human Cortical Folding,” *Cerebral Cortex*, vol. 18, no. 6, pp. 1415–1420, Jun. 2008. doi: [10.1093/CERCOR/BHM174](https://doi.org/10.1093/CERCOR/BHM174). [Online]. Available: <https://academic.oup.com/cercor/article/18/6/1415/273888>.
- [114] D. C. Van Essen and H. A. Drury, “Structural and Functional Analyses of Human Cerebral Cortex Using a Surface-Based Atlas,” *Journal of Neuroscience*, vol. 17, no. 18, pp. 7079–7102, Sep. 1997. doi: [10.1523/JNEUROSCI.17-18-07079.1997](https://doi.org/10.1523/JNEUROSCI.17-18-07079.1997). [Online]. Available: <https://www.jneurosci.org/content/17/18/7079.abstract>.
- [115] J. Régis, J. F. Mangin, T. Ochiai, V. Frouin, D. Rivière, A. Cachia, M. Tamura, and Y. Samson, ““Sulcal root” generic model: a hypothesis to overcome the variability of the human cortex folding patterns,” *Neurologia medico-chirurgica*, vol. 45, no. 1, pp. 1–17, Jan. 2005. doi: [10.2176/NMC.45.1](https://doi.org/10.2176/NMC.45.1). [Online]. Available: <https://pubmed.ncbi.nlm.nih.gov/15699615/>.
- [116] Y. Meng, G. Li, W. Lin, J. H. Gilmore, and D. Shen, “Spatial distribution and longitudinal development of deep cortical sulcal landmarks in infants,” *NeuroImage*, vol. 100, pp. 206–218, Oct. 2014. doi: [10.1016/J.NEUROIMAGE.2014.06.004](https://doi.org/10.1016/J.NEUROIMAGE.2014.06.004).

- [117] K. Im and P. E. Grant, “Sulcal pits and patterns in developing human brains,” *NeuroImage*, vol. 185, pp. 881–890, Jan. 2019. doi: [10.1016/J.NEUROIMAGE.2018.03.057](https://doi.org/10.1016/j.neuroimage.2018.03.057). [Online]. Available: <https://pubmed.ncbi.nlm.nih.gov/29601953/>.
- [118] G. Lohmann and D. Y. von Cramon, “Automatic labelling of the human cortical surface using sulcal basins,” *Medical image analysis*, vol. 4, no. 3, pp. 179–88, Sep. 2000. doi: [10.1016/S1361-8415\(00\)00024-4](https://doi.org/10.1016/S1361-8415(00)00024-4). [Online]. Available: <http://www.ncbi.nlm.nih.gov/pubmed/11145307>.
- [119] C.-y. Kao, M. Hofer, G. Sapiro, J. Stern, K. Rehm, and D. A. Rottenberg, “A Geometric Method for Automatic Extraction of Sulcal Fundi,” *IEEE Transactions on Medical Imaging*, vol. 26, no. 4, pp. 530–540, Apr. 2007. doi: [10.1109/TMI.2006.886810](https://doi.org/10.1109/TMI.2006.886810). [Online]. Available: <http://ieeexplore.ieee.org/document/4141194/>.
- [120] K. Im, H. J. Jo, J. F. Mangin, A. C. Evans, S. I. Kim, and J. M. Lee, “Spatial Distribution of Deep Sulcal Landmarks and Hemispherical Asymmetry on the Cortical Surface,” *Cerebral Cortex*, vol. 20, no. 3, pp. 602–611, Mar. 2010. doi: [10.1093/CERCOR/BHP127](https://doi.org/10.1093/CERCOR/BHP127). [Online]. Available: <https://academic.oup.com/cercor/article/20/3/602/419548>.
- [121] J. Giard, P. Rondao Alface, J. Gala, and B. Macq, “Fast Surface-Based Travel Depth Estimation Algorithm for Macromolecule Surface Shape Description,” *IEEE/ACM Transactions on Computational Biology and Bioinformatics*, vol. 8, no. 1, pp. 59–68, Jan. 2011. doi: [10.1109/TCBB.2009.53](https://doi.org/10.1109/TCBB.2009.53). [Online]. Available: <http://ieeexplore.ieee.org/document/4967572/>.
- [122] A. Klein, S. S. Ghosh, F. S. Bao, J. Giard, Y. Häme, E. Stavsky, *et al.*, “Mind-boggling morphometry of human brains,” *PLOS Computational Biology*, vol. 13, no. 2, D. Schneidman, Ed., e1005350, Feb. 2017. doi: [10.1371/journal.pcbi.1005350](https://doi.org/10.1371/journal.pcbi.1005350). [Online]. Available: <https://dx.plos.org/10.1371/journal.pcbi.1005350>.
- [123] K. Zilles, E. Armstrong, A. Schleicher, and H. J. Kretschmann, “The human pattern of gyrification in the cerebral cortex,” *Anatomy and embryology*, vol. 179, no. 2, pp. 173–179, Nov. 1988. doi: [10.1007/BF00304699](https://doi.org/10.1007/BF00304699). [Online]. Available: <https://pubmed.ncbi.nlm.nih.gov/3232854/>.
- [124] J. E. Kline, V. Sita, P. Illapani, L. He, M. Altaye, J. W. Logan, and N. A. Parikh, “Early cortical maturation predicts neurodevelopment in very preterm infants,” *Arch Dis Child Fetal Neonatal Ed*, vol. 105, pp. 460–465, 2020. doi: [10.1136/archdischild-2019-317466](https://doi.org/10.1136/archdischild-2019-317466). [Online]. Available: <http://fn.bmj.com/>.
- [125] J. J. Kulynych, L. F. Luevano, D. W. Jones, and D. R. Weinberger, “Cortical abnormality in schizophrenia: An in vivo application of the gyrification index,” *Biological Psychiatry*, vol. 41, no. 10, pp. 995–999, May 1997. doi: [10.1016/S0006-3223\(96\)00292-2](https://doi.org/10.1016/S0006-3223(96)00292-2).

- [126] M. Schaer, M. Bach Cuadra, L. Tamarit, F. Lazeyras, S. Eliez, and J. P. Thiran, "A Surface-based approach to quantify local cortical gyrification," *IEEE Transactions on Medical Imaging*, vol. 27, no. 2, pp. 161–170, 2008. doi: [10.1109/TMI.2007.903576](https://doi.org/10.1109/TMI.2007.903576).
- [127] A. J. Bastos-Leite, J. H. van Waesberghe, A. L. Oen, W. M. van der Flier, P. Scheltens, and F. Barkhof, "Hippocampal sulcus width and cavities: comparison between patients with Alzheimer disease and nondemented elderly subjects," *AJNR. American Journal of Neuroradiology*, vol. 27, no. 10, pp. 2141–5, Nov. 2006. [Online]. Available: <https://www.ncbi.nlm.nih.gov/pmc/articles/PMC7977199/>.
- [128] P. Reiner, E. Jouvent, E. Duchesnay, R. Cuingnet, J.-F. Mangin, and H. Chabriat, "Sulcal Span in Alzheimer's Disease, Amnesic Mild Cognitive Impairment, and Healthy Controls," *Journal of Alzheimer's Disease*, vol. 29, no. 3, pp. 605–613, Mar. 2012. doi: [10.3233/JAD-2012-111622](https://doi.org/10.3233/JAD-2012-111622). [Online]. Available: <https://www.medra.org/servlet/aliasResolver?alias=iospress&doi=10.3233/JAD-2012-111622>.
- [129] T. Liu, D. M. Lipnicki, W. Zhu, D. Tao, C. Zhang, Y. Cui, J. S. Jin, P. S. Sachdev, and W. Wen, "Cortical Gyrification and Sulcal Spans in Early Stage Alzheimer's Disease," *PLoS ONE*, vol. 7, no. 2, S. D. Ginsberg, Ed., e31083, Feb. 2012. doi: [10.1371/journal.pone.0031083](https://doi.org/10.1371/journal.pone.0031083). [Online]. Available: <https://journals.plos.org/plosone/article?id=10.1371/journal.pone.0031083>.
- [130] L. Hamelin, M. Bertoux, M. Bottlaender, H. Corne, J. Lagarde, V. Hahn, *et al.*, "Sulcal morphology as a new imaging marker for the diagnosis of early onset Alzheimer's disease," *Neurobiology of Aging*, vol. 36, no. 11, pp. 2932–2939, Nov. 2015. doi: [10.1016/j.neurobiolaging.2015.04.019](https://doi.org/10.1016/j.neurobiolaging.2015.04.019). [Online]. Available: <https://linkinghub.elsevier.com/retrieve/pii/S0197458015003759>.
- [131] K. Cai, H. Xu, H. Guan, W. Zhu, J. Jiang, Y. Cui, J. Zhang, T. Liu, and W. Wen, "Identification of Early-Stage Alzheimer's Disease Using Sulcal Morphology and Other Common Neuroimaging Indices," *PloS one*, vol. 12, no. 1, S. D. Ginsberg, Ed., e0170875, Jan. 2017. doi: [10.1371/journal.pone.0170875](https://doi.org/10.1371/journal.pone.0170875). [Online]. Available: <http://www.ncbi.nlm.nih.gov/pubmed/28129351>.
- [132] A. Cachia, A. Amad, J. Brunelin, M.-O. Krebs, M. Plaze, P. Thomas, and R. Jardri, "Deviations in cortex sulcation associated with visual hallucinations in schizophrenia," *Molecular Psychiatry*, vol. 20, no. 9, pp. 1101–1107, Sep. 2015. doi: [10.1038/mp.2014.140](https://doi.org/10.1038/mp.2014.140). [Online]. Available: <https://pubmed.ncbi.nlm.nih.gov/25349166/>.
- [133] J. Janssen, C. M. Díaz-Caneja, C. Alloza, A. Schippers, L. de Hoyos, J. Santonja, *et al.*, "Dissimilarity in Sulcal Width Patterns in the Cortex can be Used to Identify Patients With Schizophrenia With Extreme Deficits in Cognitive Performance," *Schizophrenia Bulletin*, vol. 47, no. 2, pp. 552–561, Mar. 2021. doi:

- [10.1093/SCHBUL/SBAA131](https://academic.oup.com/schizophreniabulletin/article/47/2/552/5910387). [Online]. Available: <https://academic.oup.com/schizophreniabulletin/article/47/2/552/5910387>.
- [134] J. F. Mangin, D. Rivière, A. Cachia, E. Duchesnay, Y. Cointepas, D. Papadopoulos-Orfanos, D. L. Collins, A. C. Evans, and J. Régis, “Object-based morphometry of the cerebral cortex,” *IEEE Transactions on Medical Imaging*, vol. 23, no. 8, pp. 968–982, Aug. 2004. doi: [10.1109/TMI.2004.831204](https://doi.org/10.1109/TMI.2004.831204).
- [135] C. R. Madan, “Robust estimation of sulcal morphology,” *Brain Informatics*, vol. 6, no. 1, p. 5, Dec. 2019. doi: [10.1186/s40708-019-0098-1](https://doi.org/10.1186/s40708-019-0098-1). [Online]. Available: <https://braininformatics.springeropen.com/articles/10.1186/s40708-019-0098-1>.
- [136] E. H. Willbrand, E. Ferrer, S. A. Bunge, and K. S. Weiner, “Development of human lateral prefrontal sulcal morphology and its relation to reasoning performance,” *bioRxiv*, p. 2022.09.14.507822, Sep. 2022. doi: [10.1101/2022.09.14.507822](https://doi.org/10.1101/2022.09.14.507822). [Online]. Available: <https://www.biorxiv.org/content/10.1101/2022.09.14.507822v1.abstract>.
- [137] M. J. Mateos, A. Gastelum-Strozzi, F. A. Barrios, E. Bribiesca, S. Alcauter, and J. A. Marquez-Flores, “A novel voxel-based method to estimate cortical sulci width and its application to compare patients with Alzheimer’s disease to controls,” *NeuroImage*, vol. 207, no. October 2019, p. 116 343, 2020. doi: [10.1016/j.neuroimage.2019.116343](https://doi.org/10.1016/j.neuroimage.2019.116343). [Online]. Available: <https://doi.org/10.1016/j.neuroimage.2019.116343>.
- [138] Y. Mishchenko, “A fast algorithm for computation of discrete Euclidean distance transform in three or more dimensions on vector processing architectures,” *Signal, Image and Video Processing*, vol. 9, no. 1, pp. 19–27, Jan. 2015. doi: [10.1007/S11760-012-0419-9](https://doi.org/10.1007/S11760-012-0419-9). [Online]. Available: <https://link.springer.com/article/10.1007/s11760-012-0419-9>.
- [139] N. Makris, G. P. Gasic, D. N. Kennedy, S. M. Hodge, J. R. Kaiser, M. J. Lee, *et al.*, “Cortical Thickness Abnormalities in Cocaine Addiction—A Reflection of Both Drug Use and a Pre-existing Disposition to Drug Abuse?” *Neuron*, vol. 60, no. 1, pp. 174–188, Oct. 2008. doi: [10.1016/J.NEURON.2008.08.011](https://doi.org/10.1016/J.NEURON.2008.08.011).
- [140] R. Momenan, L. E. Steckler, Z. S. Saad, S. van Rafelghem, M. J. Kerich, and D. W. Hommer, “Effects of alcohol dependence on cortical thickness as determined by magnetic resonance imaging,” *Psychiatry Research: Neuroimaging*, vol. 204, no. 2-3, pp. 101–111, Nov. 2012. doi: [10.1016/J.PSYCHRESNS.2012.05.003](https://doi.org/10.1016/J.PSYCHRESNS.2012.05.003).
- [141] E. R. Sowell, B. S. Peterson, P. M. Thompson, S. E. Welcome, A. L. Henkenius, and A. W. Toga, “Mapping cortical change across the human life span,” *Nature neuroscience*, vol. 6, no. 3, pp. 309–315, Mar. 2003. doi: [10.1038/NN1008](https://doi.org/10.1038/NN1008). [Online]. Available: <https://pubmed.ncbi.nlm.nih.gov/12548289/>.

- [142] T. D. Cannon, Y. Chung, G. He, D. Sun, A. Jacobson, T. G. Van Erp, *et al.*, “Progressive Reduction in Cortical Thickness as Psychosis Develops: A Multisite Longitudinal Neuroimaging Study of Youth at Elevated Clinical Risk,” *Biological Psychiatry*, vol. 77, no. 2, pp. 147–157, Jan. 2015. doi: [10.1016/J.BIOPSYCH.2014.05.023](https://doi.org/10.1016/J.BIOPSYCH.2014.05.023).
- [143] K. Wagstyl, L. Ronan, K. J. Whitaker, I. M. Goodyer, N. Roberts, T. J. Crow, and P. C. Fletcher, “Multiple markers of cortical morphology reveal evidence of supragranular thinning in schizophrenia,” *Translational Psychiatry*, vol. 6, no. 4, e780, 2016. doi: [10.1038/TP.2016.43](https://doi.org/10.1038/TP.2016.43). [Online]. Available: <https://www.ncbi.nlm.nih.gov/pmc/articles/PMC4872401/>.
- [144] A. Klein and J. Tourville, “101 labeled brain images and a consistent human cortical labeling protocol,” *Frontiers in neuroscience*, vol. 6, no. DEC, p. 171, 2012. doi: [10.3389/fnins.2012.00171](https://doi.org/10.3389/fnins.2012.00171). [Online]. Available: <http://www.ncbi.nlm.nih.gov/pubmed/23227001>.
- [145] V. S. Caviness, J. Meyer, N. Makris, and D. N. Kennedy, “MRI-Based Topographic Parcellation of Human Neocortex: An Anatomically Specified Method with Estimate of Reliability,” *Journal of Cognitive Neuroscience*, vol. 8, no. 6, pp. 566–587, Nov. 1996. doi: [10.1162/jocn.1996.8.6.566](https://doi.org/10.1162/jocn.1996.8.6.566). [Online]. Available: <https://direct.mit.edu/jocn/article/8/6/566-587/3232>.
- [146] J. Declerck, G. Subsol, J. P. Thirion, and N. Ayache, “Automatic retrieval of anatomical structures in 3D medical images,” *Lecture Notes in Computer Science (including subseries Lecture Notes in Artificial Intelligence and Lecture Notes in Bioinformatics)*, vol. 905, pp. 153–162, 1995. doi: [10.1007/978-3-540-49197-2_17](https://doi.org/10.1007/978-3-540-49197-2_17). [Online]. Available: https://link.springer.com/chapter/10.1007/978-3-540-49197-2_17.
- [147] C. Renault, M. Desvignes, and M. Revenu, “3D curves tracking and its application to cortical sulci detection,” in *Proceedings 2000 International Conference on Image Processing (Cat. No.00CH37101)*, IEEE, 2000, pp. 491–494. doi: [10.1109/ICIP.2000.899462](https://doi.org/10.1109/ICIP.2000.899462). [Online]. Available: <http://ieeexplore.ieee.org/document/899462/>.
- [148] G. Lohmann, F. Kruggel, and D. Y. Cramon, “Automatic detection of sulcal bottom lines in MR images of the human brain,” in *Lecture Notes in Computer Science (including subseries Lecture Notes in Artificial Intelligence and Lecture Notes in Bioinformatics)*, 1997, pp. 369–374. doi: [10.1007/3-540-63046-5_28](https://doi.org/10.1007/3-540-63046-5_28). [Online]. Available: http://link.springer.com/10.1007/3-540-63046-5_28.
- [149] G. Castellano, R. Lotufo, A. Falcao, and F. Cendes, “Characterization of the human cortex in MR images through the image foresting transform,” in *Proceedings 2003 International Conference on Image Processing (Cat. No.03CH37429)*,

- vol. 1, IEEE, 2003, pp. 357–60. doi: [10.1109/ICIP.2003.1246972](https://doi.org/10.1109/ICIP.2003.1246972). [Online]. Available: <http://ieeexplore.ieee.org/document/1246972/>.
- [150] A. Le Troter, G. Auzias, and O. Coulon, “Automatic sulcal line extraction on cortical surfaces using geodesic path density maps,” *NeuroImage*, vol. 61, no. 4, pp. 941–949, 2012. doi: [10.1016/j.neuroimage.2012.04.021](https://doi.org/10.1016/j.neuroimage.2012.04.021). [Online]. Available: <http://dx.doi.org/10.1016/j.neuroimage.2012.04.021>.
- [151] Yonggang Shi, P. Thompson, I. Dinov, and A. Toga, “Hamilton–Jacobi Skeleton on Cortical Surfaces,” *IEEE Transactions on Medical Imaging*, vol. 27, no. 5, pp. 664–673, May 2008. doi: [10.1109/TMI.2007.913279](https://doi.org/10.1109/TMI.2007.913279). [Online]. Available: <http://ieeexplore.ieee.org/document/4389763/>.
- [152] J. K. Seong, K. Im, S. W. Yoo, S. W. Seo, D. L. Na, and J. M. Lee, “Automatic extraction of sulcal lines on cortical surfaces based on anisotropic geodesic distance,” *NeuroImage*, vol. 49, no. 1, pp. 293–302, Jan. 2010. doi: [10.1016/J.NEUROIMAGE.2009.08.013](https://doi.org/10.1016/J.NEUROIMAGE.2009.08.013). [Online]. Available: <https://pubmed.ncbi.nlm.nih.gov/19683580/>.
- [153] Y. Y. Boykov and M. P. Jolly, “Interactive graph cuts for optimal boundary & region segmentation of objects in N-D images,” *Proceedings of the IEEE International Conference on Computer Vision*, vol. 1, pp. 105–112, 2001. doi: [10.1109/ICCV.2001.937505](https://doi.org/10.1109/ICCV.2001.937505).
- [154] P. Kochunov, D. A. Robin, D. R. Royall, T. Coyle, J. Lancaster, V. Kochunov, A. E. Schlosser, and P. T. Fox, “Can structural MRI indices of cerebral integrity track cognitive trends in executive control function during normal maturation and adulthood?” *Human Brain Mapping*, vol. 30, no. 8, pp. 2581–2594, Aug. 2009. doi: [10.1002/hbm.20689](https://doi.org/10.1002/hbm.20689). [Online]. Available: <http://doi.wiley.com/10.1002/hbm.20689>.
- [155] D. W. Shattuck, A. A. Joshi, D. Pantazis, E. Kan, R. A. Dutton, E. R. Sowell, P. M. Thompson, A. W. Toga, and R. M. Leahy, “Semi-automated method for delineation of landmarks on models of the cerebral cortex,” *Journal of Neuroscience Methods*, vol. 178, no. 2, pp. 385–392, Apr. 2009. doi: [10.1016/j.jneumeth.2008.12.025](https://doi.org/10.1016/j.jneumeth.2008.12.025). [Online]. Available: <https://linkinghub.elsevier.com/retrieve/pii/S0165027008007401>.
- [156] I. Lyu, S. H. Kim, N. D. Woodward, M. A. Styner, and B. A. Landman, “TRACE: A Topological Graph Representation for Automatic Sulcal Curve Extraction,” *IEEE Transactions on Medical Imaging*, vol. 37, no. 7, pp. 1653–1663, 2018. doi: [10.1109/TMI.2017.2787589](https://doi.org/10.1109/TMI.2017.2787589).
- [157] U. Ramer, “An iterative procedure for the polygonal approximation of plane curves,” *Computer Graphics and Image Processing*, vol. 1, no. 3, pp. 244–256, Nov. 1972. doi: [10.1016/S0146-664X\(72\)80017-0](https://doi.org/10.1016/S0146-664X(72)80017-0). [Online]. Available: <https://linkinghub.elsevier.com/retrieve/pii/S0146664X72800170>.

- [158] D. H. Douglas and T. K. Peucker, “Algorithms for the reduction of the number of points required to represent a digitized line or its caricature,” *Cartographica: The International Journal for Geographic Information and Geovisualization*, vol. 10, no. 2, pp. 112–122, Dec. 1973. doi: [10.3138/FM57-6770-U75U-7727](https://doi.org/10.3138/FM57-6770-U75U-7727). [Online]. Available: <http://doi.wiley.com/10.1002/9780470669488.ch2>.
- [159] J. Dubois, M. Benders, C. Borradori-Tolsa, A. Cachia, F. Lazeyras, R. Ha-Vinh Leuchter, S. V. Sizonenko, S. K. Warfield, J. F. Mangin, and P. S. Hüppi, “Primary cortical folding in the human newborn: an early marker of later functional development,” *Brain*, vol. 131, no. 8, pp. 2028–2041, Aug. 2008. doi: [10.1093/BRAIN/AWN137](https://doi.org/10.1093/BRAIN/AWN137). [Online]. Available: <https://academic.oup.com/brain/article/131/8/2028/267469>.
- [160] P. Kochunov, D. C. Glahn, P. T. Fox, J. L. Lancaster, K. Saleem, W. Shelledy, *et al.*, “Genetics of primary cerebral gyrification: Heritability of length, depth and area of primary sulci in an extended pedigree of Papio baboons,” *NeuroImage*, vol. 53, no. 3, pp. 1126–1134, 2010. doi: [10.1016/j.neuroimage.2009.12.045](https://doi.org/10.1016/j.neuroimage.2009.12.045). [Online]. Available: <http://dx.doi.org/10.1016/j.neuroimage.2009.12.045>.
- [161] S. Durrleman, X. Pennec, A. Trouvé, and N. Ayache, “Measuring Brain Variability Via Sulcal Lines Registration: A Diffeomorphic Approach,” in *Medical Image Computing and Computer-Assisted Intervention – MICCAI 2007*, Berlin, Heidelberg: Springer Berlin Heidelberg, pp. 675–682. doi: [10.1007/978-3-540-75757-3_82](https://doi.org/10.1007/978-3-540-75757-3_82). [Online]. Available: http://link.springer.com/10.1007/978-3-540-75757-3_82.
- [162] F. Leroy, Q. Cai, S. L. Bogart, J. Dubois, O. Coulon, K. Monzalvo, *et al.*, “New human-specific brain landmark: The depth asymmetry of superior temporal sulcus,” *Proceedings of the National Academy of Sciences*, vol. 112, no. 4, pp. 1208–1213, Jan. 2015. doi: [10.1073/pnas.1412389112](https://doi.org/10.1073/pnas.1412389112). [Online]. Available: <http://www.pnas.org/lookup/doi/10.1073/pnas.1412389112>.
- [163] A. Pron, C. Deruelle, and O. Coulon, “U-shape short-range extrinsic connectivity organisation around the human central sulcus,” *Brain Structure and Function*, vol. 226, no. 1, pp. 179–193, Jan. 2021. doi: [10.1007/s00429-020-02177-5](https://doi.org/10.1007/s00429-020-02177-5). [Online]. Available: <http://link.springer.com/10.1007/s00429-020-02177-5>.
- [164] J. S. Kippenhan, R. K. Olsen, C. B. Mervis, C. A. Morris, and P. Kohn, “Genetic Contributions to Human Gyrification: Sulcal Morphometry in Williams Syndrome,” *Journal of Neuroscience*, vol. 25, no. 34, pp. 7840–7846, Aug. 2005. doi: [10.1523/JNEUROSCI.1722-05.2005](https://doi.org/10.1523/JNEUROSCI.1722-05.2005). [Online]. Available: <http://www.jneurosci.org/cgi/doi/10.1523/JNEUROSCI.1722-05.2005>.

- [165] F. Pizzagalli, G. Auzias, Q. Yang, S. R. Mathias, J. Faskowitz, J. D. Boyd, *et al.*, “The reliability and heritability of cortical folds and their genetic correlations across hemispheres,” *Communications Biology*, vol. 3, no. 1, p. 510, Dec. 2020. doi: [10.1038/s42003-020-01163-1](https://doi.org/10.1038/s42003-020-01163-1). [Online]. Available: <http://www.nature.com/articles/s42003-020-01163-1>.
- [166] A. F. Alexander-Bloch, A. Raznahan, S. N. Vandekar, J. Seidlitz, Z. Lu, S. R. Mathias, *et al.*, “Imaging local genetic influences on cortical folding,” *Proceedings of the National Academy of Sciences*, vol. 117, no. 13, pp. 7430–7436, Mar. 2020. doi: [10.1073/pnas.1912064117](https://doi.org/10.1073/pnas.1912064117). [Online]. Available: <http://www.pnas.org/lookup/doi/10.1073/pnas.1912064117>.
- [167] K. Im, Y. Y. Choi, J. J. Yang, K. H. Lee, S. I. Kim, P. E. Grant, and J. M. Lee, “The relationship between the presence of sulcal pits and intelligence in human brains,” *NeuroImage*, vol. 55, no. 4, pp. 1490–1496, 2011. doi: [10.1016/j.neuroimage.2010.12.080](https://doi.org/10.1016/j.neuroimage.2010.12.080). [Online]. Available: <http://dx.doi.org/10.1016/j.neuroimage.2010.12.080>.
- [168] F. De Guio, D. Germanaud, J. Lefèvre, C. Fischer, J. F. Mangin, H. Chabriat, and E. Jouvent, “Alteration of the Cortex Shape as a Proxy of White Matter Swelling in Severe Cerebral Small Vessel Disease,” *Frontiers in Neurology*, vol. 10, no. JUL, p. 753, 2019. doi: [10.3389/FNEUR.2019.00753](https://doi.org/10.3389/FNEUR.2019.00753). [Online]. Available: <https://www.ncbi.nlm.nih.gov/pmc/articles/PMC6635831/>.
- [169] W. D. Hopkins, A. Meguerditchian, O. Coulon, S. Bogart, J. F. Mangin, C. C. Sherwood, *et al.*, “Evolution of the Central Sulcus Morphology in Primates,” *Brain, Behavior and Evolution*, vol. 84, no. 1, pp. 19–30, 2014. doi: [10.1159/000362431](https://doi.org/10.1159/000362431). [Online]. Available: <https://www.karger.com/Article/FullText/362431>.
- [170] M. Shokouhi, J. H. G. Williams, G. D. Waiter, and B. Condon, “Changes in the Sulcal Size Associated With Autism Spectrum Disorder Revealed by Sulcal Morphometry,” *Autism Research*, vol. 5, no. 4, pp. 245–252, Aug. 2012. doi: [10.1002/aur.1232](https://doi.org/10.1002/aur.1232). [Online]. Available: <https://onlinelibrary.wiley.com/doi/full/10.1002/aur.1232>
<https://onlinelibrary.wiley.com/doi/abs/10.1002/aur.1232>
<https://onlinelibrary.wiley.com/doi/10.1002/aur.1232>.
- [171] K. Im, J.-M. Lee, U. Yoon, Y.-W. Shin, S. B. Hong, I. Y. Kim, J. S. Kwon, and S. I. Kim, “Fractal dimension in human cortical surface: Multiple regression analysis with cortical thickness, sulcal depth, and folding area,” *Human Brain Mapping*, vol. 27, no. 12, pp. 994–1003, Dec. 2006. doi: [10.1002/hbm.20238](https://doi.org/10.1002/hbm.20238). [Online]. Available: <https://onlinelibrary.wiley.com/doi/10.1002/hbm.20238>.
- [172] M. E. Rettmann, X. Han, C. Xu, and J. L. Prince, “Automated Sulcal Segmentation Using Watersheds on the Cortical Surface,” *NeuroImage*, vol. 15, no. 2,

- pp. 329–344, 2002. doi: [10.1006/nimg.2001.0975](https://doi.org/10.1006/nimg.2001.0975). [Online]. Available: <http://linkinghub.elsevier.com/retrieve/pii/S1053811901909759>.
- [173] J. S. B. Mitchell, D. M. Mount, and C. H. Papadimitriou, “The Discrete Geodesic Problem,” *SIAM Journal on Computing*, vol. 16, no. 4, pp. 647–668, Aug. 1987. doi: [10.1137/0216045](https://doi.org/10.1137/0216045). [Online]. Available: <http://epubs.siam.org/doi/10.1137/0216045>.
- [174] A. Jacobson *et al.*, *gptoolbox: Geometry Processing Toolbox*, 2021. [Online]. Available: <https://github.com/alecjacobson/gptoolbox/>.
- [175] O. K.-C. Au, C.-L. Tai, H.-K. Chu, D. Cohen-Or, and T.-Y. Lee, “Skeleton extraction by mesh contraction,” in *ACM SIGGRAPH 2008 papers on - SIGGRAPH '08*, New York, New York, USA: ACM Press, 2008, p. 1. doi: [10.1145/1399504.1360643](https://doi.org/10.1145/1399504.1360643). [Online]. Available: <http://portal.acm.org/citation.cfm?doid=1399504.1360643>.
- [176] J. B. Kruskal, “On the Shortest Spanning Subtree of a Graph and the Traveling Salesman Problem,” *Proceedings of the American Mathematical Society*, vol. 7, no. 1, p. 48, Feb. 1956. doi: [10.2307/2033241](https://doi.org/10.2307/2033241). [Online]. Available: <https://www.jstor.org/stable/2033241?origin=crossref>.
- [177] E. W. Dijkstra, “A note on two problems in connexion with graphs,” *Numerische Mathematik*, vol. 1, no. 1, pp. 269–271, Dec. 1959. doi: [10.1007/BF01386390](https://doi.org/10.1007/BF01386390). [Online]. Available: <http://link.springer.com/10.1007/BF01386390>.
- [178] D. Van Essen, K. Ugurbil, E. Auerbach, D. Barch, T. Behrens, R. Bucholz, *et al.*, “The Human Connectome Project: A data acquisition perspective,” *NeuroImage*, vol. 62, no. 4, pp. 2222–2231, Oct. 2012. doi: [10.1016/j.neuroimage.2012.02.018](https://doi.org/10.1016/j.neuroimage.2012.02.018). [Online]. Available: <https://linkinghub.elsevier.com/retrieve/pii/S1053811912001954>.
- [179] M. F. Glasser, S. N. Sotiropoulos, J. A. Wilson, T. S. Coalson, B. Fischl, J. L. Andersson, *et al.*, “The minimal preprocessing pipelines for the Human Connectome Project,” *NeuroImage*, vol. 80, pp. 105–124, Oct. 2013. doi: [10.1016/j.neuroimage.2013.04.127](https://doi.org/10.1016/j.neuroimage.2013.04.127). [Online]. Available: <https://linkinghub.elsevier.com/retrieve/pii/S1053811913005053>.
- [180] A. A. Joshi, D. Pantazis, Q. Li, H. Damasio, D. W. Shattuck, A. W. Toga, and R. M. Leahy, “Sulcal set optimization for cortical surface registration,” *NeuroImage*, vol. 50, no. 3, pp. 950–9, Apr. 2010. doi: [10.1016/j.neuroimage.2009.12.064](https://doi.org/10.1016/j.neuroimage.2009.12.064). [Online]. Available: <http://www.ncbi.nlm.nih.gov/pubmed/20056160>.
- [181] D. Pantazis, A. Joshi, J. Jiang, D. W. Shattuck, L. E. Bernstein, H. Damasio, and R. M. Leahy, “Comparison of landmark-based and automatic methods for cortical surface registration,” *NeuroImage*, vol. 49, no. 3, pp. 2479–93, Feb. 2010. doi: [10.1016/j.neuroimage.2009.09.027](https://doi.org/10.1016/j.neuroimage.2009.09.027). [Online]. Available: <http://www.ncbi.nlm.nih.gov/pubmed/19796696>.

- [182] C. Amiez, C. R. E. Wilson, and E. Procyk, "Variations of cingulate sulcal organization and link with cognitive performance," *Scientific Reports*, vol. 8, no. 1, p. 13988, Dec. 2018. doi: [10.1038/s41598-018-32088-9](https://doi.org/10.1038/s41598-018-32088-9). [Online]. Available: <http://www.nature.com/articles/s41598-018-32088-9>.
- [183] D. Yekutieli and Y. Benjamini, "The control of the false discovery rate in multiple testing under dependency," *The Annals of Statistics*, vol. 29, no. 4, pp. 1165–1188, Aug. 2001. doi: [10.1214/aos/1013699998](https://doi.org/10.1214/aos/1013699998). [Online]. Available: <http://projecteuclid.org/euclid.aos/1013699998>.
- [184] P. Besl and N. D. McKay, "A method for registration of 3-D shapes," *IEEE Transactions on Pattern Analysis and Machine Intelligence*, vol. 14, no. 2, pp. 239–256, Feb. 1992. doi: [10.1109/34.121791](https://doi.org/10.1109/34.121791). [Online]. Available: <http://ieeexplore.ieee.org/document/121791/>.
- [185] R. Vallat, "Pingouin: statistics in Python," *Journal of Open Source Software*, vol. 3, no. 31, p. 1026, Nov. 2018. doi: [10.21105/joss.01026](https://doi.org/10.21105/joss.01026). [Online]. Available: <https://joss.theoj.org/papers/10.21105/joss.01026>.
- [186] M. Bertoux, J. Lagarde, F. Corlier, L. Hamelin, J. F. Mangin, O. Colliot, *et al.*, "Sulcal morphology in Alzheimer's disease: an effective marker of diagnosis and cognition," *Neurobiology of Aging*, vol. 84, pp. 41–49, Dec. 2019. doi: [10.1016/J.NEUROBIOLAGING.2019.07.015](https://doi.org/10.1016/J.NEUROBIOLAGING.2019.07.015).
- [187] E. Jouvent, S. Reyes, J. F. Mangin, P. Roca, M. Perrot, B. Thyreau, D. Herve, M. Dichgans, and H. Chabriat, "Apathy is related to cortex morphology in CADASIL: A sulcal-based morphometry study," *Neurology*, vol. 76, no. 17, pp. 1472–1477, Apr. 2011. doi: [10.1212/WNL.0b013e31821810a4](https://doi.org/10.1212/WNL.0b013e31821810a4). [Online]. Available: <https://pubmed.ncbi.nlm.nih.gov/21518996/>.
- [188] K. Jin, T. Zhang, M. Shaw, P. Sachdev, and N. Cherbuin, "Relationship Between Sulcal Characteristics and Brain Aging," *Frontiers in Aging Neuroscience*, vol. 10, p. 339, Nov. 2018. doi: [10.3389/FNAGI.2018.00339/BIBTEX](https://doi.org/10.3389/FNAGI.2018.00339/BIBTEX).
- [189] H. Tang, T. Liu, H. Liu, J. Jiang, J. Cheng, H. Niu, S. Li, H. Brodaty, P. Sachdev, and W. Wen, "A slower rate of sulcal widening in the brains of the nondemented oldest old," *NeuroImage*, vol. 229, p. 117740, Apr. 2021. doi: [10.1016/J.NEUROIMAGE.2021.117740](https://doi.org/10.1016/J.NEUROIMAGE.2021.117740).
- [190] J.-F. Mangin, E. Jouvent, and A. Cachia, "In-vivo measurement of cortical morphology: means and meanings," *Current Opinion in Neurology*, vol. 23, no. 4, pp. 359–367, Aug. 2010. doi: [10.1097/WCO.0b013e32833a0afc](https://doi.org/10.1097/WCO.0b013e32833a0afc). [Online]. Available: <https://journals.lww.com/00019052-201008000-00004>.
- [191] P. Kochunov, W. Rogers, J.-F. Mangin, and J. Lancaster, "A Library of Cortical Morphology Analysis Tools to Study Development, Aging and Genetics of Cerebral Cortex," *Neuroinformatics*, vol. 10, no. 1, pp. 81–96, Jan. 2012. doi: [10.1007/s12021-011-9127-9](https://doi.org/10.1007/s12021-011-9127-9). [Online]. Available: <http://link.springer.com/10.1007/s12021-011-9127-9>.

- [192] B. Fischl, “FreeSurfer,” *NeuroImage*, vol. 62, no. 2, pp. 774–781, Aug. 2012. doi: [10.1016/J.NEUROIMAGE.2012.01.021](https://doi.org/10.1016/J.NEUROIMAGE.2012.01.021).
- [193] P. E. Danielsson, “Euclidean distance mapping,” *Computer Graphics and Image Processing*, vol. 14, no. 3, pp. 227–248, Nov. 1980. doi: [10.1016/0146-664X\(80\)90054-4](https://doi.org/10.1016/0146-664X(80)90054-4).
- [194] D. R. McKay, P. Kochunov, M. D. Cykowski, J. W. Kent, A. R. Laird, J. L. Lancaster, J. Blangero, D. C. Glahn, and P. T. Fox, “Sulcal Depth-Position Profile Is a Genetically Mediated Neuroscientific Trait: Description and Characterization in the Central Sulcus,” *The Journal of Neuroscience*, vol. 33, no. 39, pp. 15 618–15 625, Sep. 2013. doi: [10.1523/JNEUROSCI.1616-13.2013](https://doi.org/10.1523/JNEUROSCI.1616-13.2013). [Online]. Available: <https://www.jneurosci.org/content/33/39/15618>.
- [195] T. Liu, P. S. Sachdev, D. M. Lipnicki, J. Jiang, G. Geng, W. Zhu, *et al.*, “Limited relationships between two-year changes in sulcal morphology and other common neuroimaging indices in the elderly,” *NeuroImage*, vol. 83, pp. 12–17, Dec. 2013. doi: [10.1016/j.neuroimage.2013.06.058](https://doi.org/10.1016/j.neuroimage.2013.06.058). [Online]. Available: <https://linkinghub.elsevier.com/retrieve/pii/S1053811913006952>.
- [196] P. J. LaMontagne, T. L. Benzinger, J. C. Morris, S. Keefe, R. Hornbeck, C. Xiong, *et al.*, “OASIS-3: Longitudinal Neuroimaging, Clinical, and Cognitive Dataset for Normal Aging and Alzheimer Disease,” *medRxiv*, p. 2019.12.13.19014902, Dec. 2019. doi: [10.1101/2019.12.13.19014902](https://doi.org/10.1101/2019.12.13.19014902). [Online]. Available: <https://www.medrxiv.org/content/10.1101/2019.12.13.19014902v1>.
- [197] A. M. Dale, B. Fischl, and M. I. Sereno, “Cortical Surface-Based Analysis: I. Segmentation and Surface Reconstruction,” *NeuroImage*, vol. 9, no. 2, pp. 179–194, Feb. 1999. doi: [10.1006/nimg.1998.0395](https://doi.org/10.1006/nimg.1998.0395). [Online]. Available: <https://linkinghub.elsevier.com/retrieve/pii/S1053811998903950>.
- [198] B. Fischl, D. H. Salat, E. Busa, M. Albert, M. Dieterich, C. Haselgrove, *et al.*, “Whole Brain Segmentation: Automated Labeling of Neuroanatomical Structures in the Human Brain,” *Neuron*, vol. 33, no. 3, pp. 341–355, Jan. 2002. doi: [10.1016/S0896-6273\(02\)00569-X](https://doi.org/10.1016/S0896-6273(02)00569-X).
- [199] T. Möller and B. Trumbore, “Fast, Minimum Storage Ray-Triangle Intersection,” *Journal of Graphics Tools*, vol. 2, no. 1, pp. 21–28, Jan. 1997. doi: [10.1080/10867651.1997.10487468](https://doi.org/10.1080/10867651.1997.10487468). [Online]. Available: <https://www.tandfonline.com/doi/abs/10.1080/10867651.1997.10487468>.
- [200] M. Perrot, D. Rivière, and J. F. Mangin, “Cortical sulci recognition and spatial normalization,” *Medical Image Analysis*, vol. 15, no. 4, pp. 529–550, Aug. 2011. doi: [10.1016/J.MEDIA.2011.02.008](https://doi.org/10.1016/J.MEDIA.2011.02.008).

- [201] P. Virtanen, R. Gommers, T. E. Oliphant, M. Haberland, T. Reddy, D. Cournapeau, *et al.*, “SciPy 1.0: fundamental algorithms for scientific computing in Python,” *Nature Methods*, vol. 17, no. 3, pp. 261–272, Mar. 2020. doi: [10.1038/s41592-019-0686-2](https://doi.org/10.1038/s41592-019-0686-2). [Online]. Available: <http://www.nature.com/articles/s41592-019-0686-2>.
- [202] D. J. Hagler, A. P. Saygin, and M. I. Sereno, “Smoothing and cluster thresholding for cortical surface-based group analysis of fMRI data,” *NeuroImage*, vol. 33, no. 4, pp. 1093–1103, Dec. 2006. doi: [10.1016/j.neuroimage.2006.07.036](https://doi.org/10.1016/j.neuroimage.2006.07.036). [Online]. Available: <https://pubmed.ncbi.nlm.nih.gov/17011792/>.
- [203] M. J. Lindstrom and D. M. Bates, “Newton-Raphson and EM Algorithms for Linear Mixed-Effects Models for Repeated-Measures Data,” *Journal of the American Statistical Association*, vol. 83, no. 404, p. 1014, Dec. 1988. doi: [10.2307/2290128](https://doi.org/10.2307/2290128).
- [204] H. Y. Lin, C. C. Huang, K. H. Chou, A. C. Yang, C. Y. Z. Lo, S. J. Tsai, and C. P. Lin, “Differential Patterns of Gyrus and Sulcal Morphological Changes During Normal Aging Process,” *Frontiers in Aging Neuroscience*, vol. 13, p. 15, Feb. 2021. doi: [10.3389/FNAGI.2021.625931/BIBTEX](https://doi.org/10.3389/FNAGI.2021.625931/BIBTEX).
- [205] L. Buée, P. R. Hof, and A. Delacourte, “Brain Microvascular Changes in Alzheimer’s Disease and Other Dementias,” *Annals of the New York Academy of Sciences*, vol. 826, no. 1, pp. 7–24, Sep. 1997. doi: [10.1111/J.1749-6632.1997.TB48457.X](https://doi.org/10.1111/J.1749-6632.1997.TB48457.X). [Online]. Available: <https://onlinelibrary.wiley.com/doi/full/10.1111/j.1749-6632.1997.tb48457.x>.
- [206] A. F. Marquand, S. M. Kia, M. Zabihi, T. Wolfers, J. K. Buitelaar, and C. F. Beckmann, “Conceptualizing mental disorders as deviations from normative functioning,” *Molecular Psychiatry* 2019 24:10, vol. 24, no. 10, pp. 1415–1424, Jun. 2019. doi: [10.1038/s41380-019-0441-1](https://doi.org/10.1038/s41380-019-0441-1). [Online]. Available: <https://www.nature.com/articles/s41380-019-0441-1>.
- [207] M. Ono, S. Kubik, and C. D. Abernathy, *Atlas of the cerebral sulci*. Thieme Medical Publishers, 1990, p. 218.
- [208] A. M. Winkler, M. A. Webster, J. C. Brooks, I. Tracey, S. M. Smith, and T. E. Nichols, “Non-parametric combination and related permutation tests for neuroimaging,” *Human brain mapping*, vol. 37, no. 4, pp. 1486–1511, Apr. 2016. doi: [10.1002/HBM.23115](https://doi.org/10.1002/HBM.23115). [Online]. Available: <https://pubmed.ncbi.nlm.nih.gov/26848101/>.
- [209] T. Zhang, X. Li, X. Jiang, F. Ge, S. Zhang, L. Zhao, *et al.*, “Cortical 3-hinges could serve as hubs in cortico-cortical connective network,” *Brain imaging and behavior*, vol. 14, no. 6, pp. 2512–2529, Dec. 2020. doi: [10.1007/S11682-019-00204-6](https://doi.org/10.1007/S11682-019-00204-6). [Online]. Available: <https://pubmed.ncbi.nlm.nih.gov/31950404/>.

- [210] L. Borne, D. Rivière, M. Mancip, and J. F. Mangin, “Automatic labeling of cortical sulci using patch- or CNN-based segmentation techniques combined with bottom-up geometric constraints,” *Medical Image Analysis*, vol. 62, p. 101 651, May 2020. doi: [10.1016/J.MEDIA.2020.101651](https://doi.org/10.1016/J.MEDIA.2020.101651).
- [211] I. Lyu, S. Bao, L. Hao, J. Yao, J. A. Miller, W. Voorhies, W. D. Taylor, S. A. Bunge, K. S. Weiner, and B. A. Landman, “Labeling lateral prefrontal sulci using spherical data augmentation and context-aware training,” *NeuroImage*, vol. 229, p. 117 758, Apr. 2021. doi: [10.1016/J.NEUROIMAGE.2021.117758](https://doi.org/10.1016/J.NEUROIMAGE.2021.117758).

APPENDIX A: SUPPLEMENTARY MATERIAL FOR CHAPTER 3

A.1. Curvature and Depth Statistics

Mean Curvature (mm^{-1})

<i>Sulcus Name</i>	ABLE		GPDM		TRACE		Mindboggle		ABLE - GPDM		ABLE - TRACE		ABLE - Mindboggle	
	<i>Mean(sd)</i>		<i>Mean(sd)</i>		<i>Mean(sd)</i>		<i>Mean(sd)</i>		<i>t^a(p-FDR^b)</i>	<i>Cohen's D(CI)^c</i>	<i>t(p-FDR)</i>	<i>Cohen's D(CI)</i>	<i>t(p-FDR)</i>	<i>Cohen's D(CI)</i>
<i>Left Hemisphere</i>														
Calcarine	0.348 (0.058)		0.364 (0.101)		0.259 (0.042)		0.168 (0.101)		-2.19 (0.255)	-0.30 (-0.60, -0.01)	18.88 (<0.001)	1.93 (1.44, 2.43)	13.60 (<0.001)	2.44 (1.86, 3.03)
Central Sulcus	0.436 (0.048)		0.429 (0.059)		0.309 (0.032)		0.326 (0.046)		1.38 (1.000)	0.15 (-0.14, 0.45)	24.40 (<0.001)	3.63 (2.82, 4.43)	21.79 (<0.001)	2.73 (2.10, 3.37)
Cingulate	0.327 (0.047)		0.294 (0.090)		0.256 (0.034)		0.293 (0.040)		2.92 (0.051)	0.58 (0.26, 0.90)	17.15 (<0.001)	2.21 (1.67, 2.75)	6.85 (<0.001)	0.97 (0.62, 1.33)
Parieto-Occipital Fissure	0.303 (0.075)		0.346 (0.130)		0.261 (0.031)		0.263 (0.059)		-2.58 (0.110)	-0.51 (-0.82, -0.20)	4.84 (<0.001)	0.94 (0.59, 1.29)	4.43 (0.001)	0.76 (0.43, 1.09)
Superior Temporal	0.307 (0.056)		0.298 (0.077)		0.221 (0.035)		0.237 (0.051)		1.53 (0.912)	0.16 (-0.14, 0.45)	19.18 (<0.001)	2.13 (1.60, 2.66)	11.38 (<0.001)	1.49 (1.06, 1.91)
<i>Right Hemisphere</i>														
Calcarine	0.354 (0.065)		0.395 (0.096)		0.272 (0.031)		0.192 (0.067)		-4.06 (0.002)	-0.61 (-0.92, -0.29)	11.91 (<0.001)	1.98 (1.48, 2.49)	14.22 (<0.001)	2.91 (2.24, 3.58)
Central Sulcus	0.401 (0.045)		0.400 (0.050)		0.278 (0.023)		0.304 (0.037)		0.26 (1.000)	0.03 (-0.26, 0.32)	25.63 (<0.001)	4.25 (3.33, 5.18)	18.10 (<0.001)	2.73 (2.09, 3.36)
Cingulate	0.336 (0.044)		0.272 (0.079)		0.258 (0.028)		0.290 (0.037)		6.57 (<0.001)	1.08 (0.71, 1.45)	18.93 (<0.001)	2.40 (1.83, 2.98)	12.42 (<0.001)	1.22 (0.83, 1.60)
Parieto-Occipital Fissure	0.295 (0.055)		0.341 (0.125)		0.259 (0.036)		0.259 (0.052)		-3.12 (0.031)	-0.66 (-0.98, -0.34)	5.67 (<0.001)	0.92 (0.57, 1.27)	5.32 (<0.001)	0.80 (0.47, 1.14)
Superior Temporal	0.305 (0.048)		0.293 (0.078)		0.226 (0.108)		0.238 (0.047)		1.59 (0.829)	0.23 (-0.06, 0.53)	6.83 (<0.001)	1.33 (0.93, 1.73)	10.14 (<0.001)	1.83 (1.36, 2.31)

Mean Depth (mm)

<i>Sulcus Name</i>	ABLE		GPDM		TRACE		Mindboggle		ABLE - GPDM		ABLE - TRACE		ABLE - Mindboggle	
	<i>Mean(sd)</i>		<i>Mean(sd)</i>		<i>Mean(sd)</i>		<i>Mean(sd)</i>		<i>t^a(p-FDR^b)</i>	<i>Cohen's D(CI)^c</i>	<i>t(p-FDR)</i>	<i>Cohen's D(CI)</i>	<i>t(p-FDR)</i>	<i>Cohen's D(CI)</i>
<i>Left Hemisphere</i>														
Calcarine	12.48 (1.55)		15.19 (3.06)		11.80 (1.49)		11.73 (2.77)		-7.77 (<0.001)	-1.28 (-1.67, -0.88)	5.50 (<0.001)	0.45 (0.14, 0.75)	1.85 (0.513)	0.36 (0.06, 0.66)
Central Sulcus	14.27 (1.18)		17.27 (1.48)		12.27 (0.90)		13.05 (0.95)		-26.19 (<0.001)	-2.31 (-2.87, -1.75)	21.34 (<0.001)	1.98 (1.48, 2.48)	12.34 (<0.001)	1.20 (0.82, 1.59)
Cingulate	9.16 (1.13)		8.27 (1.45)		8.99 (0.81)		9.73 (0.84)		4.25 (0.001)	0.73 (0.40, 1.06)	1.86 (0.512)	0.19 (-0.11, 0.48)	-4.70 (<0.001)	-0.62 (-0.94, -0.30)
Parieto-Occipital Fissure	13.59 (1.78)		16.69 (3.12)		13.46 (1.54)		14.25 (1.95)		-8.33 (<0.001)	-1.40 (-1.81, -0.99)	0.59 (1.000)	0.07 (-0.22, 0.36)	-2.78 (0.068)	-0.40 (-0.71, -0.10)
Superior Temporal	14.02 (1.80)		15.81 (2.43)		12.66 (1.51)		12.58 (1.49)		-10.46 (<0.001)	-0.86 (-1.20, -0.52)	12.61 (<0.001)	0.83 (0.49, 1.17)	8.54 (<0.001)	0.90 (0.55, 1.25)
<i>Right Hemisphere</i>														
Calcarine	13.03 (1.62)		16.24 (2.71)		12.37 (1.74)		12.72 (2.56)		-11.50 (<0.001)	-1.64 (-2.08, -1.19)	3.96 (0.003)	0.41 (0.10, 0.71)	1.24 (1.000)	0.20 (-0.10, 0.49)
Central Sulcus	14.47 (1.07)		17.69 (1.24)		12.75 (0.93)		13.32 (0.85)		-27.55 (<0.001)	-2.86 (-3.52, -2.20)	14.36 (<0.001)	1.77 (1.30, 2.24)	9.46 (<0.001)	1.26 (0.87, 1.65)
Cingulate	9.58 (1.18)		9.00 (1.82)		9.21 (0.98)		9.60 (0.84)		3.24 (0.023)	0.43 (0.12, 0.73)	3.45 (0.013)	0.30 (0.00, 0.60)	-0.34 (1.000)	-0.03 (-0.32, 0.26)
Parieto-Occipital Fissure	14.59 (1.53)		18.43 (3.19)		14.59 (1.54)		15.50 (2.03)		-9.45 (<0.001)	-1.68 (-2.13, -1.23)	-0.06 (1.000)	-0.01 (-0.30, 0.28)	-4.42 (<0.001)	-0.54 (-0.86, -0.23)
Superior Temporal	15.85 (1.79)		19.22 (2.63)		14.10 (1.23)		14.20 (1.63)		-14.34 (<0.001)	-1.52 (-1.95, -1.09)	14.26 (<0.001)	1.19 (0.81, 1.57)	9.58 (<0.001)	1.00 (0.64, 1.36)

^aComparisons between groups were conducted using the pairwise *t*-test.

^b*p*-values in bold remain significant after entering all uncorrected *p*-values ($N = 120$) into a False Discovery Rate (FDR) correction for multiple comparisons with $q = 0.05$.

^cCI= 95% confidence interval.

Table A.1: Comparison of the values of mean sulcal fundi curvatures and depths: *p*-values FDR corrected.

A.2. Bland-Altman Plots per Sulcus

A.2.1. Bland-Altman Plots for Calcarine Sulcus

Bland-Altman Plot: Left Calcarine Sulcus

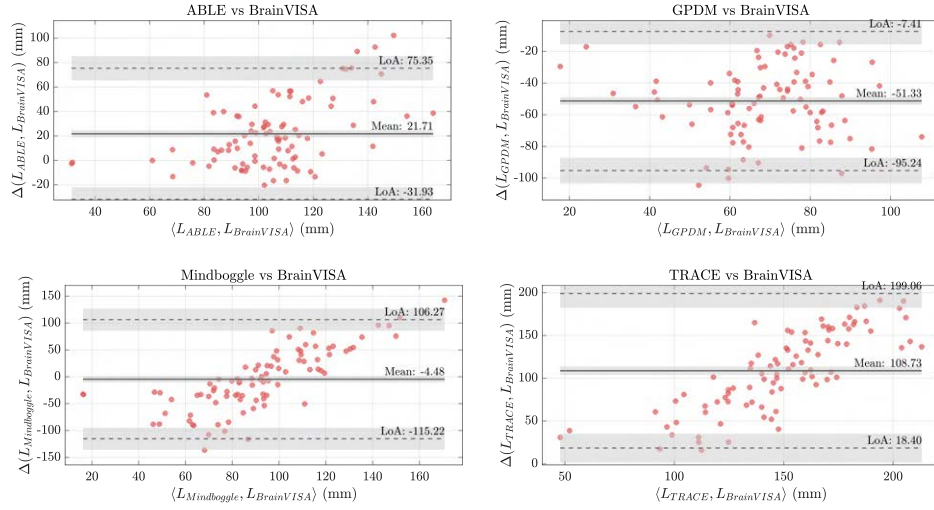


Figure A.1: Bland-Altman plot comparing the four methods (ABLE, GPDM, Mindboggle, and TRACE) against BrainVISA's reference values for the left calcarine sulcus.

Bland-Altman Plot: Right Calcarine Sulcus

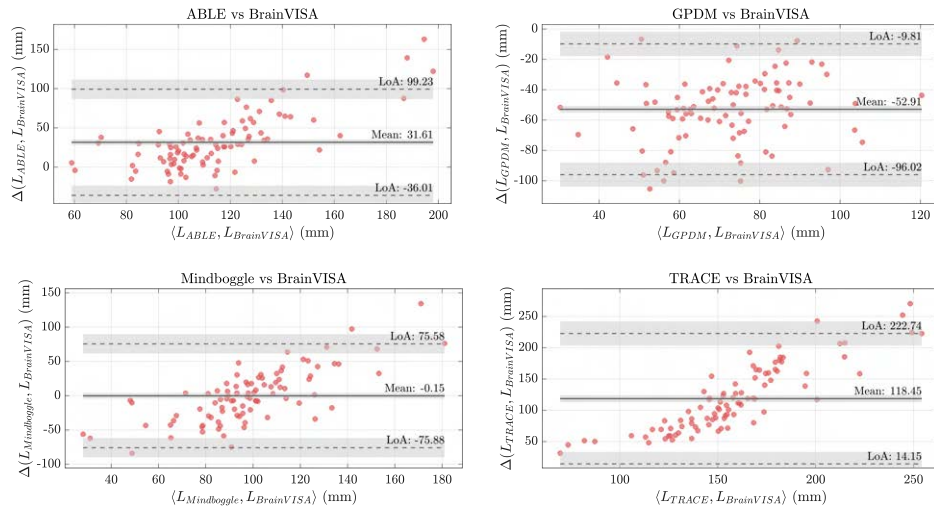


Figure A.2: Bland-Altman plot comparing the four methods (ABLE, GPDM, Mindboggle, and TRACE) against BrainVISA's reference values for the right calcarine sulcus.

A.2.2. Bland-Altman Plots for Central Sulcus

Bland-Altman Plot: Left Central Sulcus

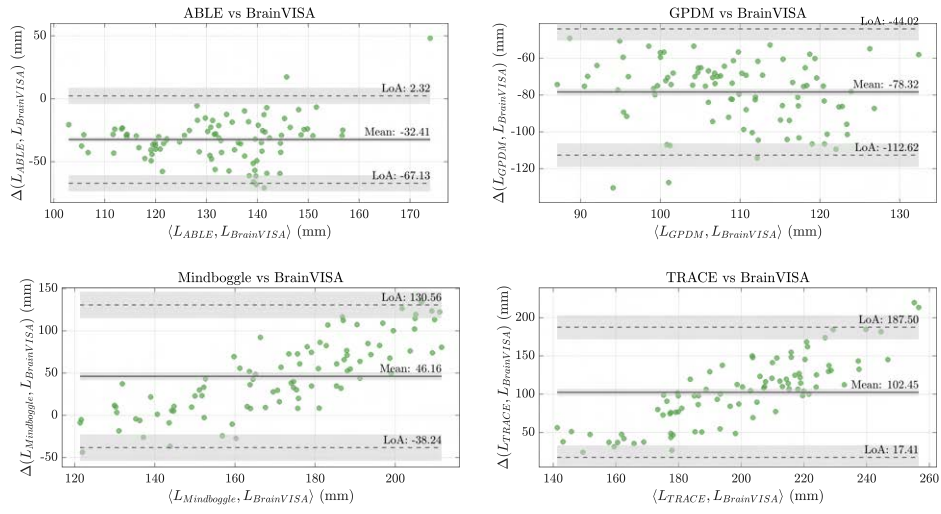


Figure A.3: Bland-Altman plot comparing the four methods (ABLE, GPDM, Mindboggle, and TRACE) against BrainVISA's reference values for the left central sulcus.

Bland-Altman Plot: Right Central Sulcus

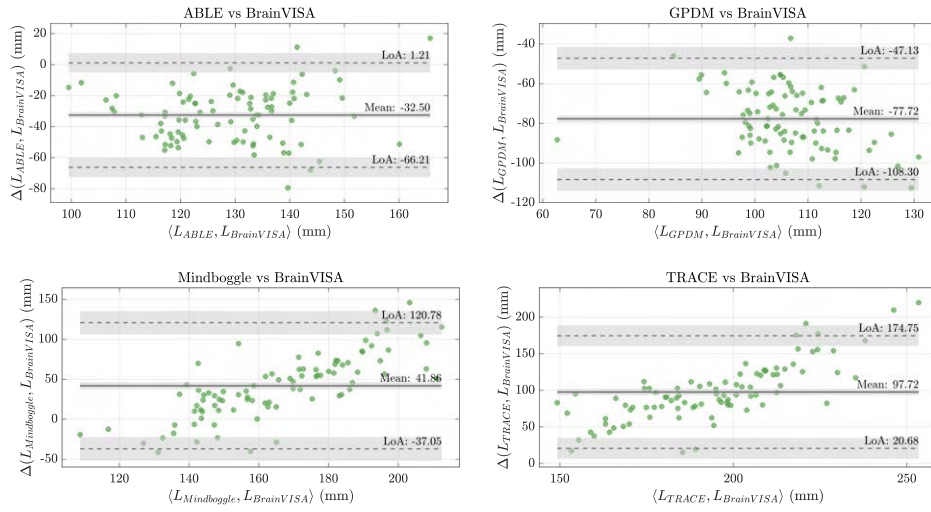


Figure A.4: Bland-Altman plot comparing the four methods (ABLE, GPDM, Mindboggle, and TRACE) against BrainVISA's reference values for the right central sulcus.

A.2.3. Bland-Altman Plots for Cingulate Sulcus

Bland-Altman Plot: Left Cingulate Sulcus

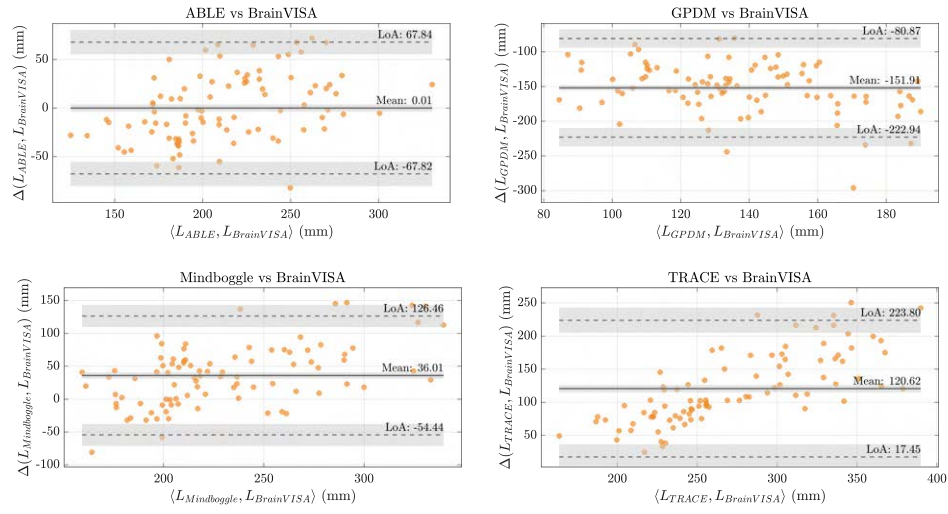


Figure A.5: Bland-Altman plot comparing the four methods (ABLE, GPDM, Mindboggle, and TRACE) against BrainVISA's reference values for the left cingulate sulcus.

Bland-Altman Plot: Right Cingulate Sulcus

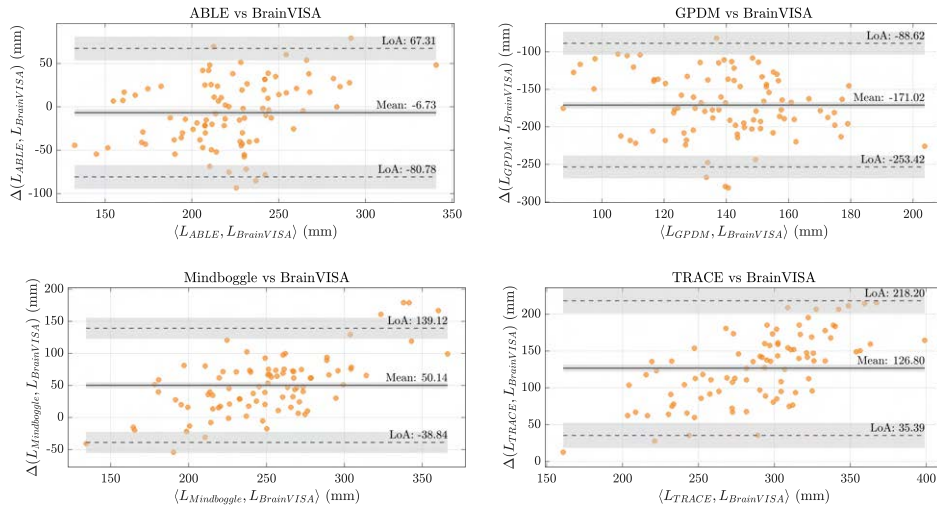


Figure A.6: Bland-Altman plot comparing the four methods (ABLE, GPDM, Mindboggle, and TRACE) against BrainVISA's reference values for the right cingulate sulcus.

A.2.4. Bland-Altman Plots for Parieto-Occipital Fissure

Bland-Altman Plot: Left Parieto-Occipital Fissure

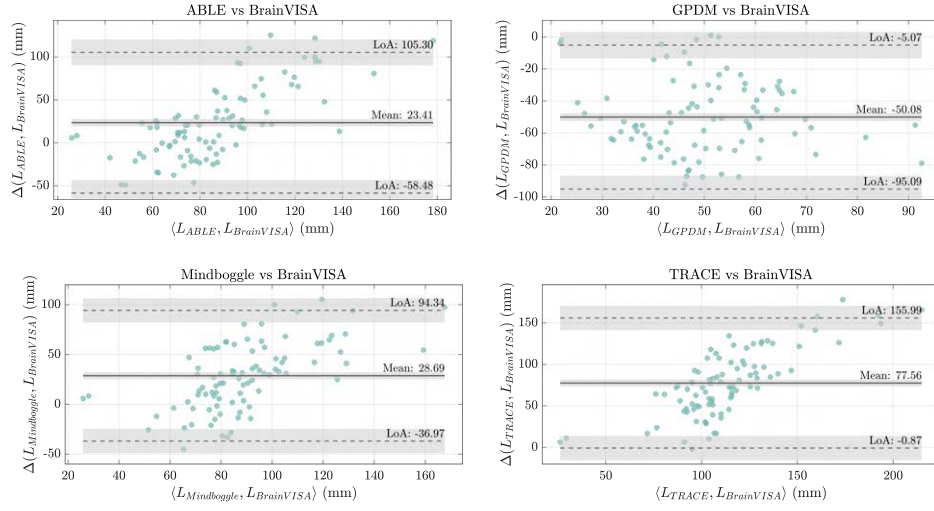


Figure A.7: Bland-Altman plot comparing the four methods (ABLE, GPDM, Mindboggle, and TRACE) against BrainVISA's reference values for the left parieto-occipital fissure.

Bland-Altman Plot: Right Parieto-Occipital Fissure

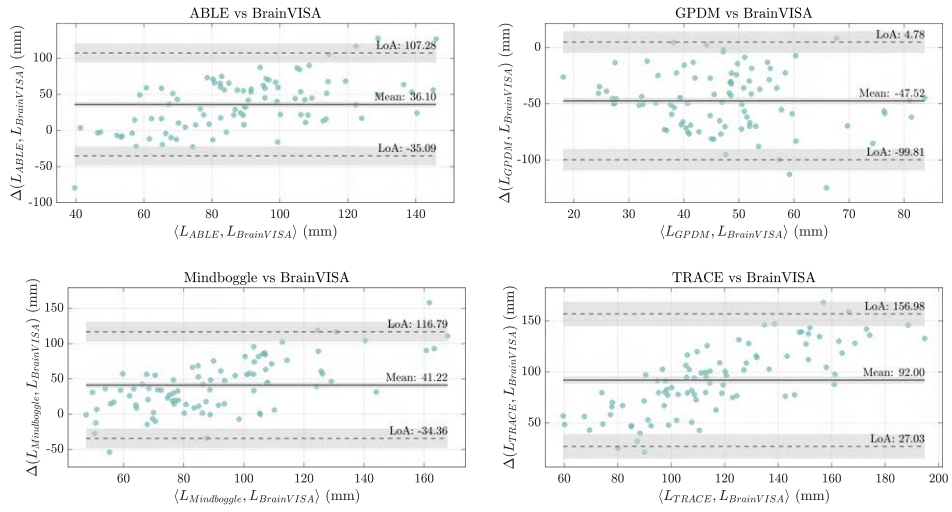


Figure A.8: Bland-Altman plot comparing the four methods (ABLE, GPDM, Mindboggle, and TRACE) against BrainVISA's reference values for the right parieto-occipital fissure.

A.2.5. Bland-Altman Plots for Superior Temporal Sulcus

Bland-Altman Plot: Left Superior Temporal Sulcus

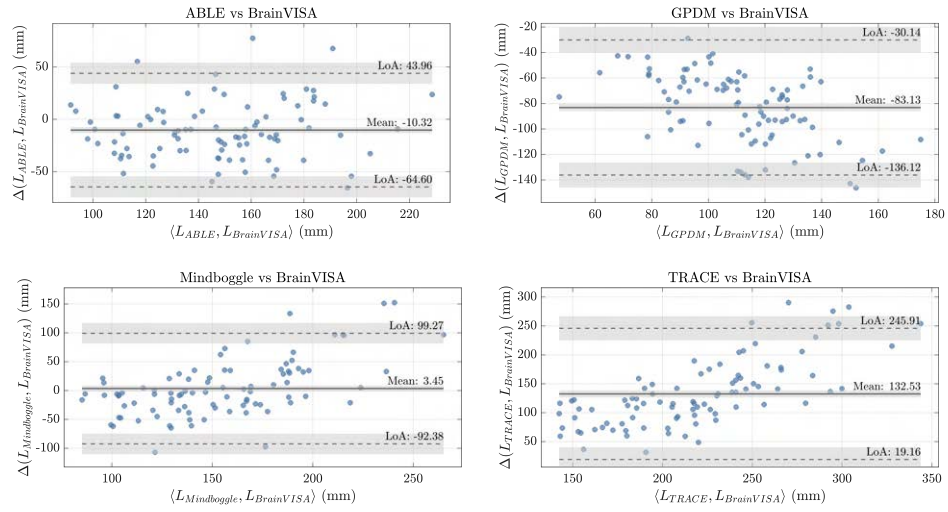


Figure A.9: Bland-Altman plot comparing the four methods (ABLE, GPDM, Mindboggle, and TRACE) against BrainVISA's reference values for the left superior temporal sulcus.

Bland-Altman Plot: Right Superior Temporal Sulcus

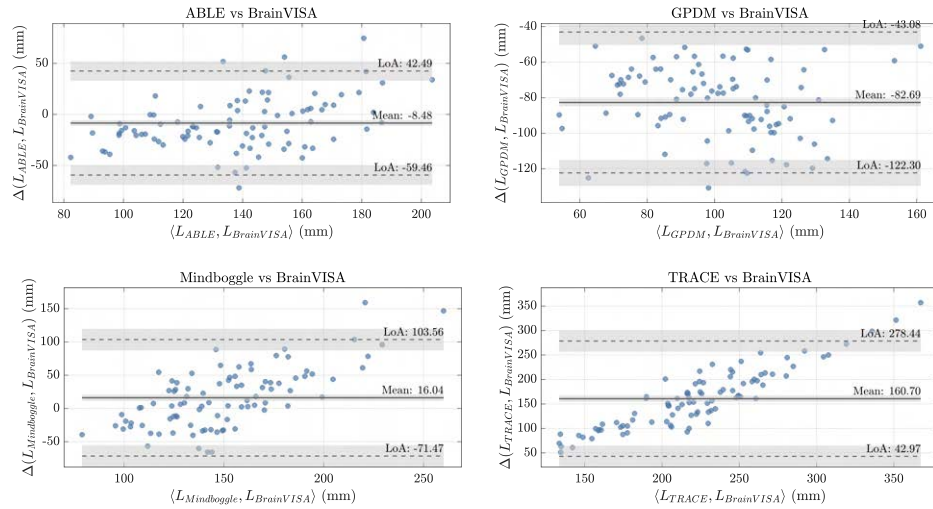


Figure A.10: Bland-Altman plot comparing the four methods (ABLE, GPDM, Mindboggle, and TRACE) against BrainVISA's reference values for the right superior temporal sulcus.

A.3. Summary of Longitude Differences Between Methods and Reference Values

<i>Sulcus Name</i>	Differences between methods and BrainVISA (mm)			
	ABLE <i>Mean (CI[2.5%], CI[97.5%])</i>	GPDM <i>Mean (CI[2.5%], CI[97.5%])</i>	TRACE <i>Mean (CI[2.5%], CI[97.5%])</i>	Mindboggle <i>Mean (CI[2.5%], CI[97.5%])</i>
<i>Left Hemisphere</i>				
<i>Calcarine</i>	21.71 (-31.94, 75.35)	-51.33 (-95.24, -7.41)	108.73 (18.40, 199.06)	-4.48 (-115.22, 106.27)
<i>Central Sulcus</i>	-32.41 (-67.13, 2.32)	-78.32 (-112.62, -44.02)	102.45 (17.41, 187.50)	46.16 (-38.24, 130.56)
<i>Cingulate</i>	0.01 (-67.82, 67.84)	-151.91 (-222.94, -80.87)	120.62 (17.45, 223.80)	36.01 (-54.44, 126.46)
<i>Parieto-Occipital Fissure</i>	23.41 (-58.48, 105.31)	-50.08 (-95.09, -5.07)	77.56 (-0.87, 155.99)	28.69 (-36.97, 94.34)
<i>Superior Temporal</i>	-10.32 (-64.60, 43.96)	-83.13 (-136.12, -30.14)	132.53 (19.16, 245.91)	3.45 (-92.38, 99.27)
<i>Right Hemisphere</i>				
<i>Calcarine</i>	31.61 (-36.01, 99.23)	-52.91 (-96.02, -9.81)	118.45 (14.15, 222.75)	-0.15 (-75.88, 75.58)
<i>Central Sulcus</i>	-32.50 (-66.21, 1.21)	-77.72 (-108.30, -47.13)	97.72 (20.68, 174.75)	41.86 (-37.05, 120.78)
<i>Cingulate</i>	-6.73 (-80.78, 67.31)	-171.02 (-253.42, -88.62)	126.80 (35.39, 218.21)	50.14 (-38.85, 139.12)
<i>Parieto-Occipital Fissure</i>	36.10 (-35.09, 107.28)	-47.52 (-99.81, 4.78)	92.00 (27.03, 156.98)	41.22 (-34.36, 116.79)
<i>Superior Temporal</i>	-8.48 (-59.46, 42.49)	-82.69 (-122.30, -43.08)	160.70 (42.97, 278.44)	16.04 (-71.47, 103.56)

Table A.2: Summary of mean differences between methods and confidence intervals extracted from the Bland-Altman plots.

A.4. Intercept of Sulcal Longitude Regressions

<i>Sulcus Name</i>	ABLE <i>Intercept CI([2.5%],[97.5%])</i>	GPDM <i>Intercept CI([2.5%],[97.5%])</i>	TRACE <i>Intercept CI([2.5%],[97.5%])</i>	Mindboggle <i>Intercept CI([2.5%],[97.5%])</i>
<i>Left Hemisphere</i>				
<i>Calcarine</i>	38.68 (9.67, 67.68)	11.87 (-7.79, 31.52)	71.24 (22.68, 119.80)	99.59 (43.58, 155.60)
<i>Central Sulcus</i>	42.96 (7.33, 78.60)	55.57 (29.52, 81.61)	94.39 (-1.31, 190.09)	105.62 (11.48, 199.76)
<i>Cingulate</i>	5.34 (-37.44, 48.12)	0.64 (-29.90, 31.18)	12.27 (-48.51, 73.06)	34.66 (-22.40, 91.73)
<i>Parieto-Occipital Fissure</i>	44.76 (8.10, 81.43)	13.16 (-1.75, 28.07)	61.23 (26.01, 96.45)	52.52 (23.35, 81.69)
<i>Superior Temporal</i>	38.17 (11.64, 64.71)	18.90 (1.91, 35.89)	91.67 (32.73, 150.62)	15.58 (-34.73, 65.89)
<i>Right Hemisphere</i>				
<i>Calcarine</i>	11.97 (-29.59, 53.54)	0.03 (-24.04, 24.10)	48.42 (-14.23, 111.07)	-0.92 (-47.71, 45.86)
<i>Central Sulcus</i>	57.95 (26.47, 89.43)	41.89 (20.15, 63.63)	154.23 (70.76, 237.70)	102.18 (16.75, 187.61)
<i>Cingulate</i>	43.76 (-9.38, 96.91)	44.87 (6.09, 83.66)	75.36 (9.32, 141.39)	0.06 (-64.22, 64.35)
<i>Parieto-Occipital Fissure</i>	61.29 (33.91, 88.67)	23.77 (10.56, 36.99)	53.19 (29.17, 77.22)	41.74 (12.08, 71.39)
<i>Superior Temporal</i>	3.69 (-28.44, 35.82)	-20.54 (-41.73, 0.65)	-36.53 (-97.74, 24.67)	8.66 (-46.66, 63.98)

Table A.3: Intercept (and its confidence interval) of the linear regressions of the sulcal longitudes obtained by each of the methods and reference values.

A.5. Parameter Variation for GPDM and TRACE

A subset of 10 subjects from the test-retest database has been analyzed to characterize the sulcal length variation when different parameters of GPDM and TRACE are modified.

For GPDM, the parameters modified are the number of extremities and the probability threshold as seen in Figure A.11

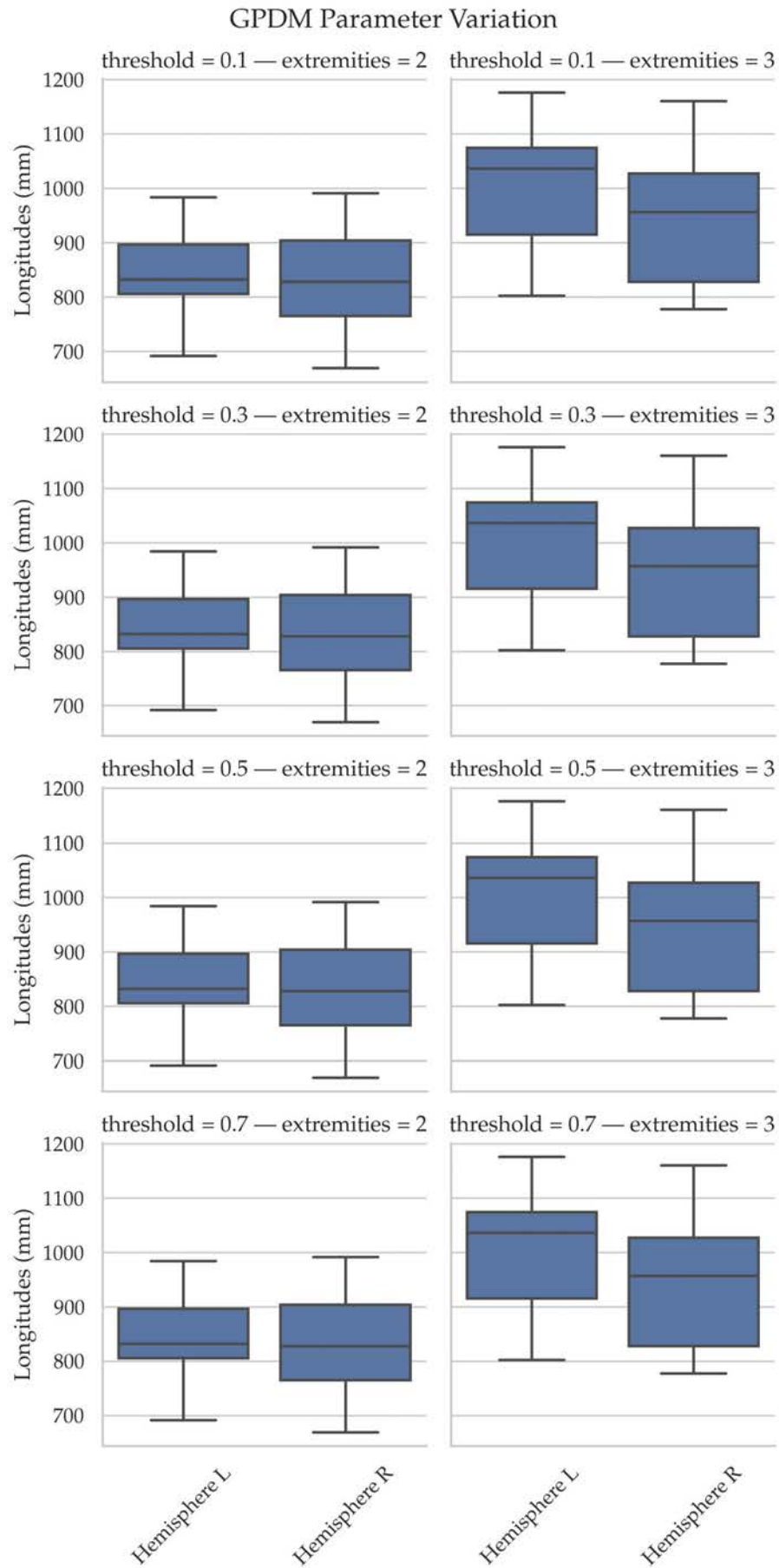


Figure A.11: Sulcal longitudes in millimeters for the parameter variation of the number of extremities and probability threshold for the GPDM tool in both left and right hemispheres.

The parameters analyzed for TRACE include the pruning threshold and the distance for the endpoint detection (see Figure A.12).

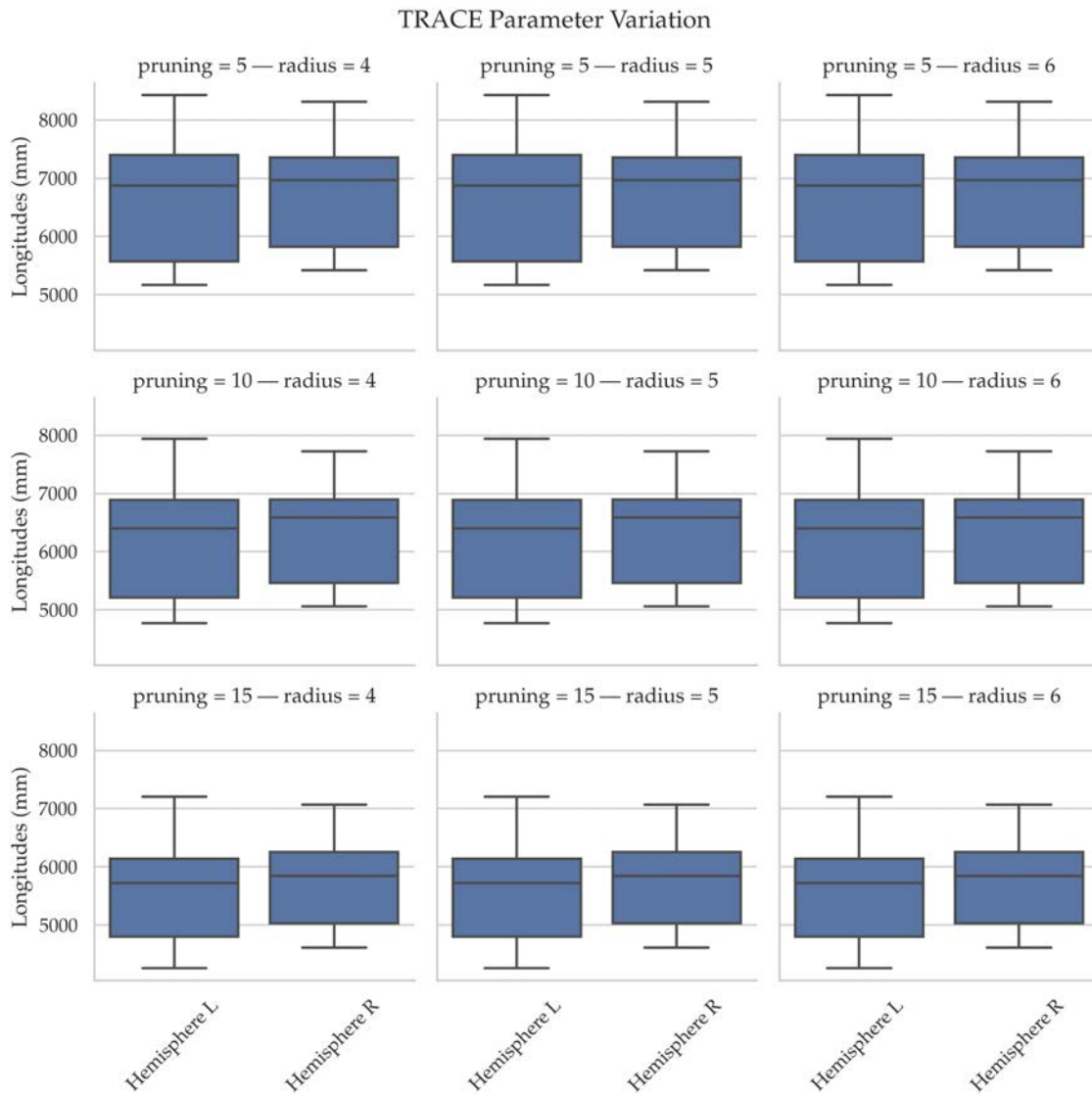


Figure A.12: Sulcal longitudes in millimeters obtained by TRACE when varying the pruning threshold and the endpoint detection distance in both left and right hemispheres.

As a reference, Figure A.13 contains the sulcal longitudes obtained by ABLE and BrainVISA for the same subset.

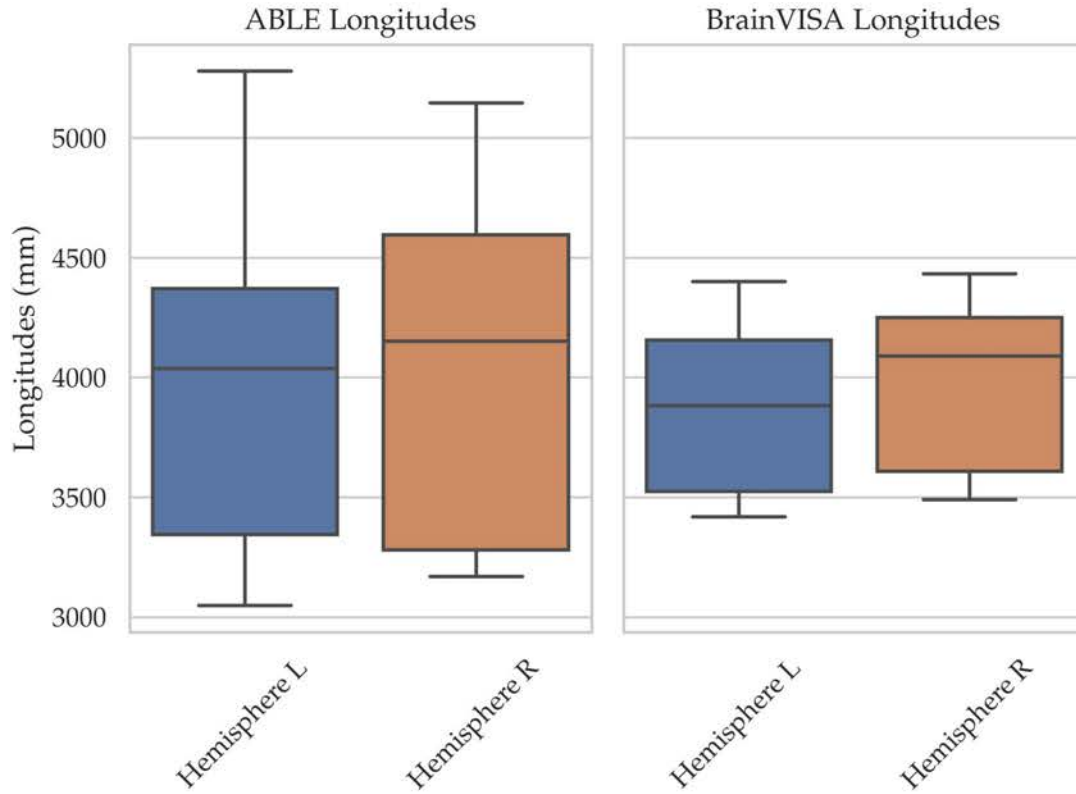


Figure A.13: Left: Longitudes obtained for ABL for the left and right hemispheres. Right: Longitudes obtained for BrainVISA for the left and right hemispheres. These values are included as a reference for comparison. Longitude values are reported in millimeters.

A.6. Point Density and Reproducibility in TRACE

We have performed an analysis of the relation between the number of points per millimeter of the labeled lines and the mean Hausdorff distances. For this analysis, we have processed the “.*scurve*” and “.*scurve.bary*” files provided by TRACE. The first one contains a list of the vertices of the surface where the line lies, while the second one is a more precise geodesic trajectory including vertices and intermediate points in edges. The boxplot in A.14 shows that the vertex-only file achieves a point density lower than 1 mm/point, associated with higher mean Hausdorff distances. The geodesic trajectory shows a density close to 3 mm/point, with mean Hausdorff distances below 1 mm.

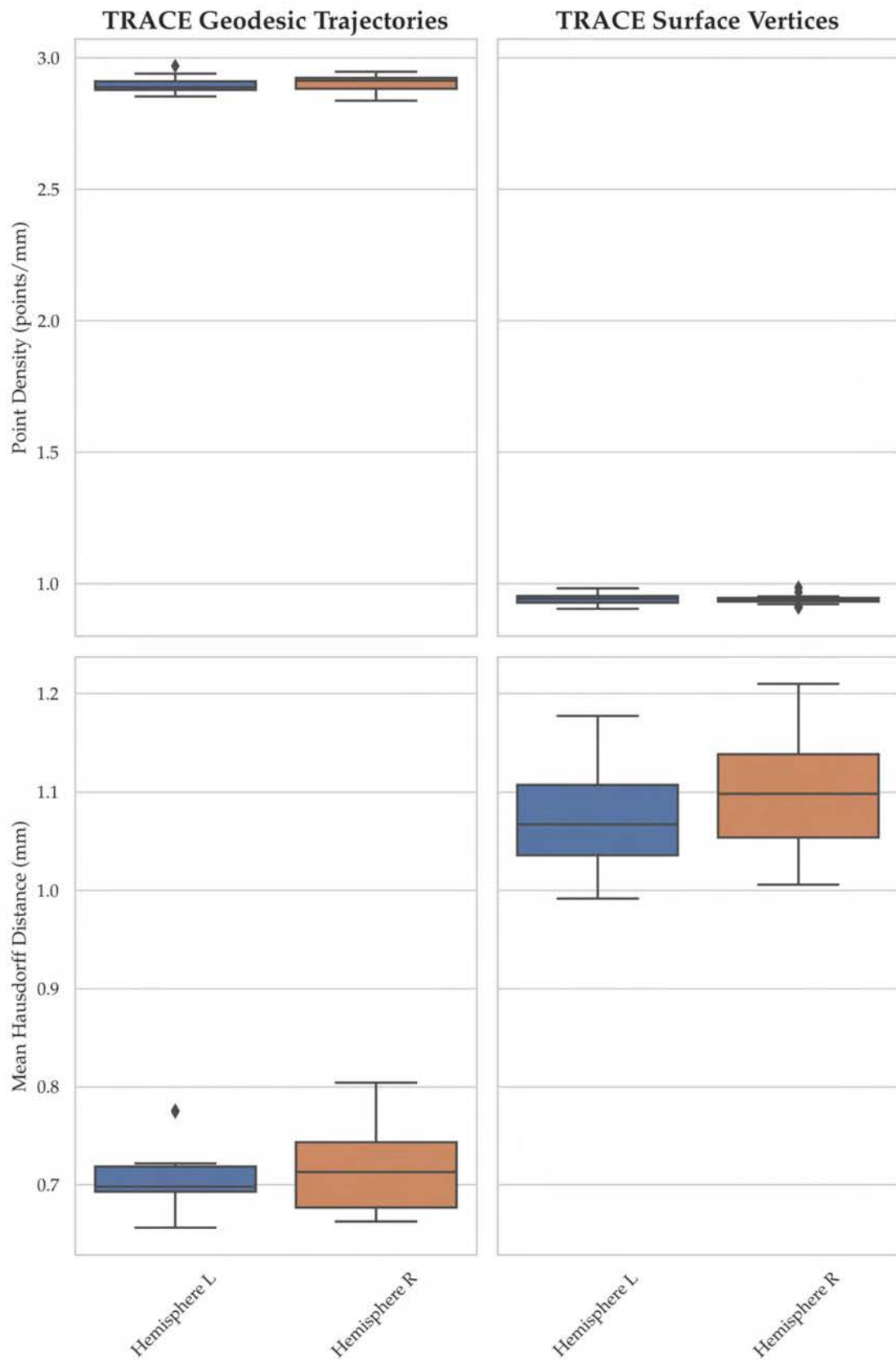


Figure A.14: The upper figures shows the point density values for TRACE using vertex-only trajectories and geodesic trajectories for both left and right hemisphere. Figures at the bottom show the associated mean Hausdorff distances for the trajectories and hemispheres.

APPENDIX B: SUPPLEMENTARY MATERIAL FOR CHAPTER 4

A.7. Depth Step Size Selection

A correct value for the parameter of depth step in the generation of isolines is essential, as it allows a proper sampling of the surface without unnecessary increments in the processing time. In this case, the simulated sulcus is used for the estimation of an optimal depth step value. This surface has a mean edge length of 0.5 mm, so we estimate width maps with depth step values ranging from the edge length (0.5 mm) to 1/50 the edge length (0.01 mm). The differences between estimated values and simulated ones are computed. Figure A.15 shows the variation of mean error and standard deviation for the different step sizes evaluated.

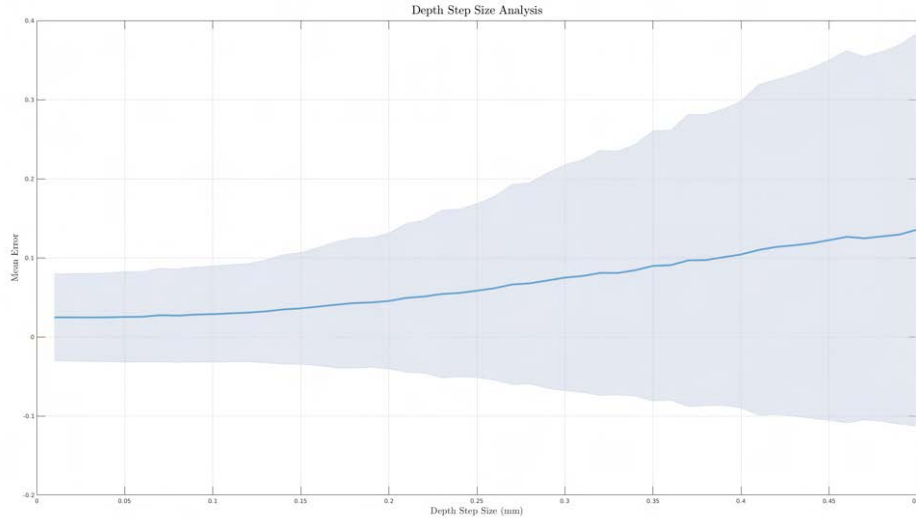


Figure A.15: Plot of the mean error and its standard deviation for the different step sizes analyzed.

The results show a slope change or elbow approximately at 0.125 mm, which is 1/4 of the edge length. In this case, we have edge lengths of 1 mm for the real data, meaning that the optimal step size would be 0.25 mm. Adding a small security margin, the default value selected for this method is 0.20 mm.